

Luminosity and Redshift Dependence of the Covering Factor of AGNs viewed with WISE and SDSS

Y.Toba^{1,2,3}, S.Oyabu⁴, H.Matsuhara^{1,2}, M.Malkan⁵, P.Gandhi⁶, T.Nakagawa², N.Isobe², M.Shirahata^{2,7}, N.Oi², Y.Ohyama⁸, S.Takita², C.Yamauchi⁹,

and

K.Yano^{2,10},

toba@ir.isas.jaxa.jp

ABSTRACT

In this work, we investigate the dependence of the covering factor (CF) of active galactic nuclei (AGNs) (i) on the mid-infrared (MIR) luminosity and (ii) on the redshift. We constructed 12- and 22- μm luminosity functions (LFs) at $0.006 \leq z \leq 0.3$ using the *Wide-field Infrared Survey Explorer* (*WISE*) data. Combining the *WISE* catalog with the Sloan Digital Sky Survey (SDSS) spectroscopic data, we selected 223,982 galaxies at 12 μm and 25,721 galaxies at 22 μm for spectroscopic classification. We then identified 16,355 AGNs at 12 μm and 4,683

¹Department of Space and Astronautical Science, the Graduate University for Advanced Studies (Sokendai), 3-1-1 Yoshinodai, Chuo-ku, Sagamihara, Kanagawa 252-5210, Japan

²Institute of Space and Astronautical Science, Japan Aerospace Exploration Agency, 3-1-1 Yoshinodai, Chuo-ku, Sagamihara, Kanagawa 252-5210, Japan

³Research Center for Space and Cosmic Evolution, Ehime University, Bunkyo-cho, Matsuyama 790-8577, Japan

⁴Graduate School of Science, Nagoya University, Furo-cho, Chikusa-ku, Nagoya, Aichi 464-8602, Japan

⁵Department of Physics and Astronomy, University of California, Los Angeles, CA 90095-1547, USA

⁶Department of Physics, Durham University, Durham DH1-3LE, UK

⁷National Astronomical Observatory of Japan, 2-21-1 Osawa, Mitaka, Tokyo 181-8588

⁸Institute of Astronomy and Astrophysics, Academia Sinica, P.O. Box 23-141, Taipei 10617, Taiwan, R.O.C

⁹Misato Observatory, 180 Matsugamine, Misato-cho, Kaiso-gun, Wakayama 640-1366, Japan

¹⁰Department of Physics, School of Science, The University of Tokyo, 7-3-1, Hongo, Bunkyo-ku, Tokyo 113-0033, Japan

AGNs at $22\ \mu\text{m}$ by their optical emission lines and cataloged classifications in the SDSS. Following that, we estimated the CF as the fraction of type 2 AGN in all AGNs whose MIR emissions are dominated by the active nucleus (not their host galaxies) based on their MIR colors. We found that (i) the CF decreased with increasing MIR luminosity, regardless of the choice of type 2 AGN classification criteria, and (ii) the CF did not change significantly with the redshift for $z \leq 0.2$. Furthermore, we carried out various tests to determine the influence of selection bias and confirmed similar dependences exist even when taking these uncertainties into account. The luminosity dependence of the CF can be explained by the receding torus model, but the “modified” receding torus model gives a slightly better fit, as suggested by Simpson.

Subject headings: galaxies: active — galaxies: luminosity function, mass function — galaxies: nuclei — infrared: galaxies — methods: statistical — catalogs

1. INTRODUCTION

The popular unification scheme for active galactic nuclei (AGNs) requires that the observed differences between type 1 and type 2 AGNs arise from the orientation (e.g., Antonucci 1993; Urry & Padovani 1995), and the basic premise is that all AGNs are fundamentally the same. This scheme proposes a geometrically thick dusty torus surrounding the AGN central engine (accretion disk and supermassive black hole), with the torus providing anisotropic obscuration of the central region so that sources viewed face-on are recognized as type 1 AGNs, while those observed edge-on are type 2 AGNs. However, even if this torus exists in all AGNs, its key parameters such as its geometry and physical properties are still unclear.

We focus here on the geometrical covering fraction of the dust torus, a fundamental parameter in the unification scheme. The covering factor (CF) is defined as the fraction of the sky, as seen from the AGN center, that is blocked by heavily obscuring material. This corresponds to the fraction of type 2 AGNs in the entire AGN population. Recently, some authors have claimed that the CF depends on the luminosity and redshift. For example, Simpson (2005) examined data for 4,304 galaxies (including AGNs) from the Sloan Digital Sky Survey (SDSS) Data Release 2 (DR2) and found that the CF decreases with increasing [OIII] emission line luminosity, which is believed to be isotropic. Hasinger (2008) also reported a negative correlation between the fraction of absorbed (\sim type 2) AGNs and the X-ray (2–10 keV) luminosity based on 1,290 AGNs selected in the 2–10 keV band from different flux-limited surveys with very high optical identification completeness. Furthermore, Hasinger (2008) found that the absorbed fraction increases significantly with increasing redshift, saturating

at a redshift of $z \sim 2$. Recently, Toba et al. (2013) also confirmed the luminosity dependence of the CF by using the *AKARI* mid-infrared all-sky survey catalog (Ishihara et al. 2010). Some authors, however, have questioned these dependencies by claiming that the data are affected by various uncertainties. In particular, the observed correlations can be explained as a selection effect, in which case they may not necessarily have any astrophysical significance. For instance, Dwelly & Page (2006) found from *XMM-Newton* observations of the Chandra Deep Field-South that there is no evidence that the absorption distribution is dependent on either the intrinsic X-ray luminosity or the redshift. Akylas et al. (2006) suggested that the apparent increase in the absorbed AGN fraction with increasing redshift is due to a systematic overestimation of the column densities measured in high redshift sources where the absorption cut-off is shifted towards low energies. Lawrence & Elvis (2010) attempted to carefully distinguish strict type 2 AGNs from more lightly reddened type 1 AGNs, as well as from low-excitation narrow-line AGNs, which were assembled from the literature. They also showed that radio, infrared (IR), and volume-limited samples all agree in showing that the type 2 fraction does not change with luminosity. Therefore, it is still unclear whether the CF intrinsically depends on the luminosity and particularly on redshift.

To resolve this problem, it is important to conduct a statistical analysis based on IR observations; reprocessed radiation from the dust in the torus is re-emitted in the IR wavelength range. Mid-IR (MIR) emission, in particular, is expected to be direct radiation from the dust torus and uninfluenced by dust extinction. In this paper, we estimate the CF of the dust torus using the MIR luminosity functions (LFs) and examine the luminosity and redshift dependence based on a statistically complete AGN sample. The LF of galaxies is a fundamental statistical tool for describing galaxy properties, since it should be almost entirely independent of the viewing angle. We construct the MIR LFs using the data from the *Wide-field Infrared Survey Explorer* (*WISE*; Wright et al. 2010), which was launched in 2009. *WISE* performed an all-sky survey with a high sensitivity in four bands (particularly relevant to the study here are the 12- and 22- μm bands). While the spatial resolution of *WISE* is relatively poor owing to the 40-cm diameter of the telescope, it is several orders of magnitude better than those of the *Infrared Astronomical Satellite* (*IRAS*; Neugebauer et al. 1984; Beichman et al. 1988) and *AKARI* (Murakami et al. 2007), both of which performed previous all-sky IR surveys.

This paper is organized as follows. Section 2 describes the sample selection and derivation of the LFs, and the 12- and 22- μm LFs computed using the $1/V_{\text{max}}$ technique are presented in Section 3. Our results are then compared with previous studies. In Section 4, we consider the origin of the MIR emission. According to an empirical method based on a *WISE* color-color diagram, we extract sources that are dominated in the MIR by the active nucleus. We then estimate the CF for those AGN-dominated MIR objects and discuss the

luminosity and redshift dependence of the CF by analyzing the relationship between the CF and luminosity in separate redshift bins. This paper provides us with statistically robust results about the luminosity and redshift dependence of the CF and yields a reliable dust torus model that explains the results. Throughout this paper, we assume a flat universe with $\Omega_k = 0$, and we adopt $(\Omega_M, \Omega_\Lambda) = (0.3, 0.7)$ and $H_0 = 75 \text{ km s}^{-1} \text{ Mpc}^{-1}$.

2. DATA AND ANALYSIS

We selected 12- and 22- μm flux-limited galaxies based on the *WISE* and SDSS catalogs, and these galaxies were then classified into five types according to their optical spectroscopic information in the SDSS catalog. For spectroscopically classified galaxies, we constructed the LFs using the $1/V_{\text{max}}$ method, considering both the detection limit of the *WISE* and SDSS catalogs.

2.1. Sample Selection

The *WISE* All-Sky Release Source Catalog provides positions and four-band (3.4-, 4.6-, 12-, and 22- μm) photometry for 563,921,584 objects. In particular, there are 26,673,624 and 3,846,254 sources in the all-sky catalog with $\geq 10\sigma$ detections in the 12- and 22- μm bands, respectively. The sample used for this study was selected from *WISE* MIR sources with spectroscopy from the SDSS DR8 (Aihara et al. 2011). In the end, we selected a 12- μm flux-limited sample of 223,982 galaxies and a 22- μm flux-limited sample of 25,721 galaxies.

2.1.1. *WISE* sample

WISE performed an all-sky survey at 3.4, 4.6, 12, and 22 μm with angular resolutions of 6.1, 6.4, 6.5, and 12.0 arcsec and a 5σ photometric sensitivity better than 0.08, 0.11, 1, and 6 mJy (corresponding to 16.5, 15.5, 11.2, and 7.9 Vega magnitudes), respectively, in these four bands (Wright et al. 2010). A flow chart of our sample selection process is shown in Figure 1.

We first narrowed our sample to *WISE* sources within the SDSS DR8 Legacy region (7966 deg²). The SDSS spectroscopic survey is performed using two multi-object fiber spectrographs on the same telescope. Each spectroscopic fiber plug plate, referred to as a “tile”, has a circular field-of-view with a radius of 1.49 degrees (Blanton et al. 2003), and 1794 tiles are employed in the Legacy survey. Because the tiles are circular, there is a fraction of the

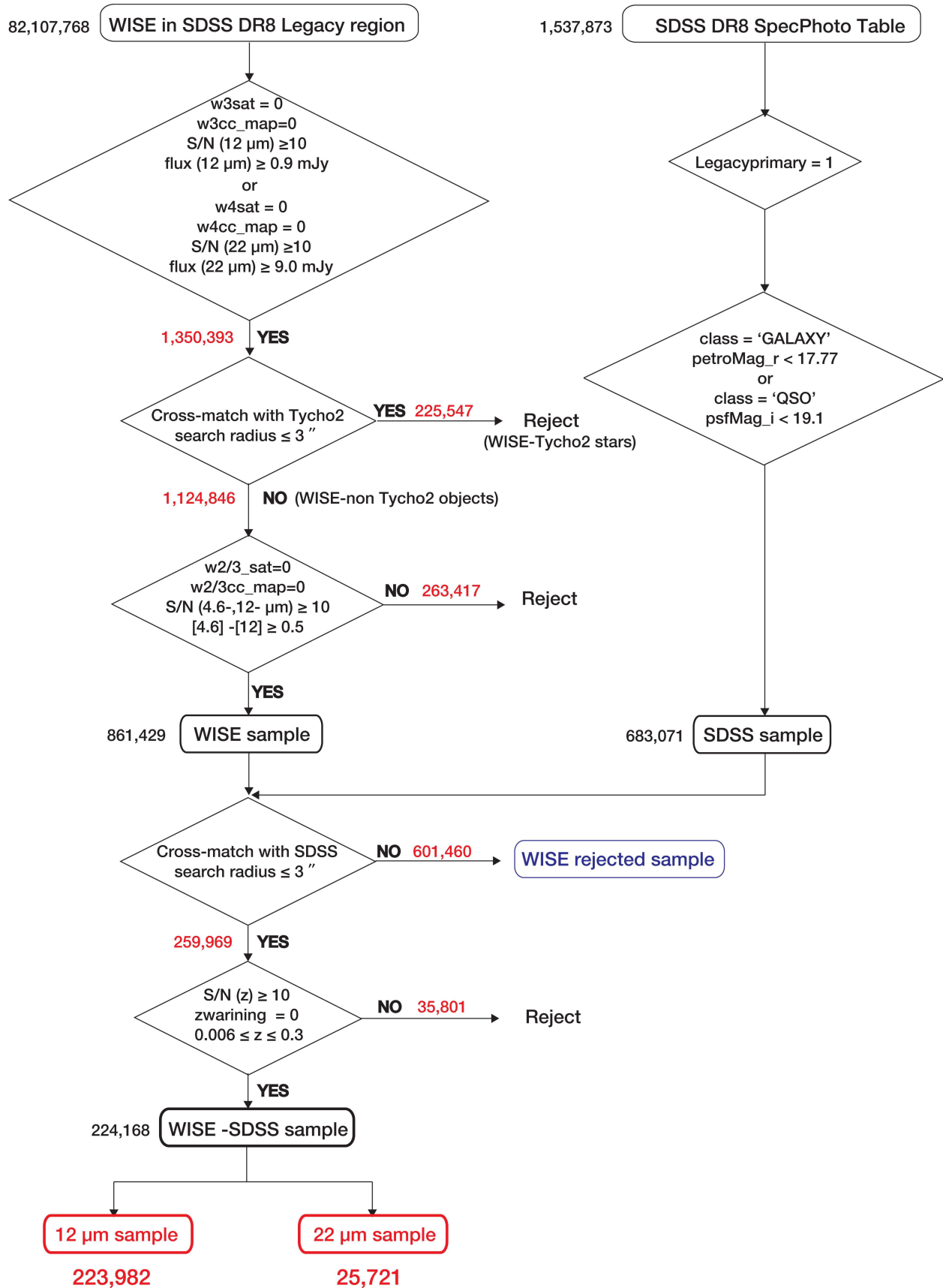


Fig. 1.— Flow chart of the sample selection process.

sky that is covered by the overlap of tiles. The equatorial coordinates of the tile centers are contained in the `sdsstilesAll` table. For the coordinates of each tile center, we searched for nearby *WISE* sources within a search radius of 1.49 degrees, which yielded a total of 82,107,768 *WISE* sources.

We then extracted 10σ -detected objects at $12\ \mu\text{m}$ above 0.9 mJy (~ 11.4 mag) or at $22\ \mu\text{m}$ above 9.0 mJy (~ 7.4 mag). These fluxes correspond to almost 100% completeness flux limits, according to the Explanatory Supplement to the *WISE* All-Sky Data Release Products¹. When the sources were extracted, we also checked whether the sources were saturated. The observed saturation levels of *WISE* are 1.0 (~ 3.8 mag) and 12.0 Jy (~ 0.4 mag) for $12\ \mu\text{m}$ and $22\ \mu\text{m}$, respectively. The saturated pixel fractions listed in the catalog are flagged as *w1-4sat* in each band. We eliminated sources that had fluxes exceeding the saturation level and a high fraction of saturated pixels (i.e., *WISE* sources with *w3sat* $\neq 0$ for $12\ \mu\text{m}$ or *w4sat* $\neq 0$ for $22\ \mu\text{m}$ were eliminated). In addition, we checked sources that were contaminated or biased due to proximity to an image artifact (e.g., diffraction spikes, scattered-light halos, or optical ghosts) according to *w1-4cc_map*. A source that was unaffected by known artifacts was flagged as *w1-4cc_map* = 0. We thus eliminated sources with *w3cc_map* $\neq 0$ for $12\ \mu\text{m}$ or *w4cc_map* $\neq 0$ for $22\ \mu\text{m}$. This reduced the number of *WISE* samples to 1,350,393. Note that the *WISE* catalog contains the Vega magnitude of each source, and we converted these to fluxes. The zero magnitude flux densities for $12\ \mu\text{m}$ and $22\ \mu\text{m}$ are 31.674 and 8.363 Jy, respectively. Here, the profile-fitting magnitude (*w1-4mpro*) was used as the magnitude for the majority of the *WISE* sources. However, because the *w1-4mpro* photometry is optimized for point sources and may underestimate the true brightness of extended sources, we used the elliptical aperture magnitude (*w1-4gmag*) for the extended sources. The aperture is based on the elliptical shape reported in the Two Micron All Sky Survey (2MASS) Extended Source Catalog (XSC). We defined extended sources using *ext_flg* in the *WISE* catalog.

These 1,350,393 sources were then cross-identified with the *Tycho-2* Catalog (Høg et al. 2000) to remove galactic bright stars. The *Tycho-2* catalog contains the positions, proper motions, and two-color photometry of the 2.5 million bright stars in the sky down to the magnitude limit of the plates ($V_T \sim 11.5$). To avoid omitting high proper-motion stars, we referred to the *mean position* rigorously propagated to the epoch J2000.0 by the proper motions in this catalog. As a result, a total of 225,547 stars (hereinafter *WISE-Tycho 2* stars) were identified. As shown in Figure 2, we adopted a 3-arcsec search radius because the star density in the SDSS spectroscopic region is at most $\sim 50\ \text{deg}^{-2}$ (Høg et al. 2000).

¹<http://wise2.ipac.caltech.edu/docs/release/allsky/expsup/>

Thus, the probability of chance coincidence is less than 0.01% (i.e., $1,350,393 \times 0.0001 \sim 135$ sources may be misidentified), which is acceptable.

Of the 1,124,846 remaining sources (hereinafter *WISE-non Tycho 2* objects), we removed certain stars based on their colors. Figure 3 shows a histogram of the $[4.6] - [12]$ color of the *WISE-non Tycho 2* objects. Here, $[4.6]$ and $[12]$ represent the Vega magnitudes in the *WISE* 4.6- and 12- μm bands, respectively. The zero magnitude flux density for 4.6 μm is 171.787 Jy. To examine the color distribution of the stars, the *WISE-Tycho 2* stars are also plotted for comparison. As shown in Figure 3, the *WISE-Tycho 2* stars are located at $[4.6] - [12] \sim 0$ because the radiation from galactic stars is dominated by the Rayleigh–Jeans tail of the blackbody spectrum, thus yielding a Vega-system color near zero. To ensure the reliability of the color value, we examined the color of objects with a signal-to-noise ratio (S/N) greater than 10, $w2/3sat = 0$, and $w2/3cc_map = 0$. We found 263,417 objects that met the following criterion as stars:

$$[4.6] - [12] \leq 0.5 . \quad (1)$$

We note, however, that there are some stars in the $0.5 < [4.6] - [12] < 1$ region, but this region also may be populated with nearby elliptical galaxies with no dust. Therefore, we adopted a robust criterion to avoid the omission of galaxies. This left 861,429 objects in our *WISE* sample.

2.1.2. SDSS sample

The SDSS DR8 spectroscopic catalog includes the main galaxy (Strauss et al. 2002), luminous red galaxy (LRG) (Eisenstein et al. 2001), and QSO (Richards et al. 2002) samples. The DR8 legacy spectroscopic survey catalog contains about 1.5 million sources and covers 7,966 deg^2 . SDSS sources with `legacyPrimary = 1` were selected from the `SpecPhoto` table, created by joining spectroscopic and photometric information. The “`legacyPrimary`” parameter is designed to choose the best available unique set of spectra of the legacy sources, and so the above criterion ensures clean spectroscopic data. We focused on the main galaxy and QSO samples in this study; these samples are magnitude-limited objects with Petrosian (1976) magnitudes brighter than $r = 17.77$ for the main galaxy sample and with point-spread function (PSF) magnitudes brighter than $i = 19.1$ for the QSO samples at $z < 3$. The principal spectroscopic type (galaxy or QSO) is listed under the column headed “`CLASS`” in the `SpecPhoto` table. We thus extracted objects with (i) `petroMag_r` below 17.77 mag and `CLASS = “GALAXY”` and (ii) `psfMag_i` below 19.1 mag and `CLASS = “QSO”`. This process selected 683,071 SDSS objects.

2.1.3. Cross-identification of WISE and SDSS

We then cross-matched the *WISE* samples with the SDSS samples. Using a matching radius of 3 arcsec, 259,969 *WISE*-SDSS objects were selected as shown in Figure 2. Adopting this search radius gives a probability of chance coincidence of 0.05%; Donoso et al. (2012) cross-matched data from the *WISE* and SDSS DR7 spectroscopic catalogs and estimated the expected false detection fraction at 3 arcsec by using random catalogs generated over the effective area. This means that $861,429 \times 0.0005 \sim 431$ sources may be misidentified, which we regard as acceptable. Note that 111 *WISE* sources have two SDSS counterparts because the spatial resolution of the SDSS is better than that of *WISE*. These sources are mostly close interacting systems of two members, and of these, we chose the closest object as the optical counterpart.

From these *WISE*-SDSS objects, we selected objects with $zWarning = 0$ and a redshift S/N greater than 10. The $zWarning$ information is contained in the `SpecPhoto` table and has flags set in suspicious cases; $zWarning = 0$ indicates that no problems were identified. Among the objects with a precise estimation of the redshift, we extracted objects with $0.006 \leq z \leq 0.3$. The redshift limit is applied because errors in the distance measurement are dominated by the peculiar motions of galaxies with $z \leq 0.006$, and thus, the luminosity also has a large error. However, for the sources at $z > 0.3$, the [NII] $\lambda 6583$ and $H\alpha$ lines that were used for classifying the sample into several galaxy types (see Section 2.2) were shifted to around 9,000 Å. This wavelength almost corresponds exactly to the upper limit of the spectroscopy coverage and results in a relatively poor sensitivity. Therefore, we set the upper limit of the redshift to 0.3 to ensure a high S/N of these optical lines. A final sample consisted of 224,168 galaxies, whose details are given in Table 1. The mean value of their redshifts is ~ 0.1 , and the redshift distribution is shown in Figure 4. Ultimately, 223,982 galaxies at 12 μm and 25,721 galaxies at 22 μm were selected through these steps.

For the selection process, we employed the “2MASS Catalog Server Kit” to easily construct a high-performance database server for the 2MASS Point Source Catalog (which includes 470,992,970 objects) and several all-sky catalogs (Yamauchi 2011). We also used the STIL Tool Set, (STILTS²) which is a set of command-line tools based on the Starlink Tables Infrastructure Library (Taylor et al. 2006). The SDSS data were obtained from the Catalog Archive Server (CAS³), a database containing catalogs of SDSS objects (both photometric and astrometric) that allows queries of their measured attributes.

²<http://www.star.bristol.ac.uk/~mbt/stilts/>

³<http://skyserver.sdss3.org/dr8/>

Table 1. List of the 224,168 selected galaxies.

objname	RA (J2000.0)	DEC (J2000.0)	f ₁₂ (mJy)	f ₂₂ (mJy)	redshift	type	w3sat	w4sat	S/N (12 μ m)	S/N (22 μ m)	w3cc_map	w4cc_map
SDSS J000000.74-091320.2	00:00:00.73	-09:13:20.0	2.19	2.84	0.134	SF	0.0	0.0	14.90	1.10	0.0	0.0
KUG 2357+156	00:00:01.98	+15:52:53.9	8.67	11.44	0.020	SF	0.0	0.0	27.00	6.40	0.0	0.0
LCSB S0001P	00:00:03.30	-10:43:15.8	3.37	5.61	0.083	Composite	0.0	0.0	33.93	5.68	0.0	0.0
2MASX J00000347+1411539	00:00:03.46	+14:11:53.5	2.09	3.92	0.115	Composite	0.0	0.0	13.30	1.90	0.0	0.0
SDSS J000004.59-105834.7	00:00:04.60	-10:58:35.0	1.74	2.79	0.150	SF	0.0	0.0	12.30	2.60	0.0	0.0
2MASX J00000472+0046546	00:00:04.74	+00:46:54.2	1.75	1.73	0.080	type 2 AGN	0.0	0.0	15.29	1.99	0.0	0.0
ARK 591	00:00:07.83	-00:02:25.8	5.27	5.92	0.024	SF	0.0	0.0	41.76	6.39	0.0	0.0
2MASX J00000811+1432450	00:00:08.08	+14:32:45.9	4.45	9.06	0.105	SF	0.0	0.0	27.30	9.10	0.0	0.0
2MASX J00001235-1032114	00:00:12.34	-10:32:10.7	3.99	6.38	0.077	SF	0.0	0.0	24.60	6.80	0.0	0.0
CGCG 382-016	00:00:12.78	+01:07:13.1	15.31	19.62	0.025	SF	0.0	0.0	67.86	13.92	0.0	0.0
SDSS J000013.84+003912.1	00:00:13.86	+00:39:12.0	1.95	2.31	0.103	SF	0.0	0.0	12.30	2.20	0.0	0.0
2MASX J00001447+1412420	00:00:14.44	+14:12:42.0	1.79	4.37	0.091	LINER	0.0	0.0	11.40	2.00	0.0	0.0
2MASX J00001575-0853283	00:00:15.78	-08:53:27.3	4.81	7.13	0.056	Composite	0.0	0.0	18.20	3.70	0.0	0.0
KUG 2357+144	00:00:16.31	+14:43:59.8	4.50	5.73	0.091	SF	0.0	0.0	27.00	6.40	0.0	0.0
2MASX J00001671+1541400	00:00:16.75	+15:41:40.4	4.42	5.34	0.112	SF	0.0	0.0	27.60	5.50	0.0	0.0
SDSS J000018.63+154327.7	00:00:18.62	+15:43:27.9	1.44	3.92	0.176	SF	0.0	0.0	10.50	1.90	0.0	0.0
SDSS J000019.03-105258.9	00:00:19.03	-10:52:58.7	2.71	4.92	0.083	SF	0.0	0.0	16.90	4.30	0.0	0.0
SDSS J000019.89+142219.5	00:00:19.87	+14:22:19.8	1.81	2.91	0.094	SF	0.0	0.0	12.10	1.00	0.0	0.0
SDSS J000020.06+135001.6	00:00:20.04	+13:50:01.9	1.90	3.09	0.079	SF	0.0	0.0	13.00	1.10	0.0	0.0
SDSS J000020.93+001254.2	00:00:20.92	+00:12:54.4	2.13	3.98	0.085	SF	0.0	0.0	14.40	4.20	0.0	0.0
2MASX J00002629+0035503	00:00:26.31	+00:35:51.1	1.62	4.90	0.104	type 2 AGN	0.0	0.0	10.50	4.30	0.0	0.0
SDSS J000027.65+145624.6	00:00:27.65	+14:56:25.0	4.12	11.94	0.159	LINER	0.0	0.0	25.00	11.10	0.0	0.0
2MASX J00002809+1422530	00:00:28.07	+14:22:52.6	1.76	3.37	0.093	Composite	0.0	0.0	11.70	1.00	0.0	0.0
SDSS J000028.19+142509.8	00:00:28.19	+14:25:10.0	1.67	2.62	0.143	SF	0.0	0.0	11.30	0.70	0.0	0.0
SDSS J000030.00-103825.0	00:00:29.94	-10:38:24.7	2.50	2.89	0.151	SF	0.0	0.0	16.50	2.70	0.0	0.0
2MASX J00003086-0112473	00:00:30.89	-01:12:46.8	1.02	2.30	0.075	SF	0.0	0.0	10.54	2.74	0.0	0.0
2MASX J00003718-1102077	00:00:37.18	-11:02:07.8	3.94	9.04	0.151	type 2 AGN	0.0	0.0	23.40	8.70	0.0	0.0
SDSS J000038.68+143548.1	00:00:38.68	+14:35:48.0	1.62	2.28	0.146	SF	0.0	0.0	12.30	2.60	0.0	0.0
2MASX J00003878+1524270	00:00:38.72	+15:24:27.3	1.63	1.88	0.152	Composite	0.0	0.0	11.80	0.00	0.0	0.0

Note. — Table 1 is published in its entirety in the electronic edition of the *Astrophysical Journal*. A portion of the table is shown here for guidance regarding its form and content. There are 223,982 galaxies at 12 μ m defined by a flux of (12 μ m) \geq 9.0 mJy, $w3sat = 0.0$, $w3cc_map = 0.0$, and an S/N of (12 μ m) \geq 10. There are 25,721 galaxies at 22 μ m with a flux of (22 μ m) \geq 0.9 mJy, $w4sat = 0.0$, $w4cc_map = 0.0$, and an S/N of (22 μ m) \geq 10.

2.2. Classification of Spectroscopic Galaxy Type

We spectroscopically classified the 224,168 galaxies (hereinafter *WISE*-SDSS sample) into five types: type 1 AGNs including quasars and Seyfert 1 galaxies, type 2 AGNs, low-ionization narrow-emission-line region galaxies (LINER), galaxies that are likely to contain both star formation and AGN activity (composite types of galaxies, hereinafter “Composite”), and star-forming galaxies (SF). The classification was based on the spectroscopic information in the *SpecPhoto* table, as shown in Figure 5. Note that we consider Seyfert 2 galaxies (Sy2) as type 2 AGNs unless otherwise noted.

The type 1 AGNs were identified according to the CLASS entry (CLASS = QSO) in the *SpecPhoto* table. Objects for which CLASS = GALAXY were classified as type 2 AGNs, LINER, Composite, or SF by using the optical flux line ratios of [NII] λ 6583/H α versus [OIII] λ 5007/H β (BPT diagram suggested by Baldwin et al. 1981), as shown in Figure 6. However, the BPT diagram is not able to classify a galaxies if H α , H β , [OIII], or [NII] were not detected in the emission line. These galaxies are classified as weak-emission-line galaxies (hereinafter, “Unknown”).

The galaxy classifications, summarized in Table 2, indicate that the 22- μ m band is especially powerful for finding AGNs. The detection rate of AGNs (type 1 + type 2) in the 22- μ m band (\sim 18%) is higher than that in the 12- μ m band (\sim 7%), since the 12- μ m bandpass includes a strong contribution from polycyclic aromatic hydrocarbon (PAH) emission, which is unrelated to the presence of an active nucleus. Some authors have reported that LINERs typically have weak MIR emission (e.g., Ogle et al. 2006). Thus it might be surprising that we find such a high fraction of LINERs (\sim 6%). However, our LINER classification is based on the [NII] lines rather, than the [OI] λ 6300 or [SII] λ 6716 and λ 6731 lines others have found useful for discriminating pure LINERS (e.g., Kewley et al. 2006). If we were to adopt the [OI]/H α versus [OIII]/H β diagram, it would in fact reduce our fraction of LINERs (\sim 3.5%

Table 2. Classifications of the 223,982 galaxies for the 12- μ m LF and 25,721 galaxies for the 22- μ m LF.

type	12 μ m (percentage)	22 μ m (percentage)
type 1 AGNs	8,151 (3.6 %)	2,846 (11.0 %)
type 2 AGNs	8,204 (3.7 %)	1,837 (7.1 %)
LINER	14,491 (6.5 %)	1,477 (5.8 %)
Composite	48,834 (21.8 %)	6,583 (25.6 %)
SF	141,242 (63.0 %)	12,799 (49.8 %)
Unknown	3,060 (1.4 %)	179 (0.7 %)
All	223,982 (100 %)	25,721 (100 %)

at 22 μm). However, as our focus in this study is on type 1 and 2 AGNs and one motivation is to check whether our findings in Toba et al. (2013) based on *AKARI* are confirmed by *WISE*, we employed $[\text{NII}]/\text{H}\alpha$ versus $[\text{OIII}]/\text{H}\beta$ in the same manner as Toba et al. (2013). Figure 7 presents the flux distributions at 12 and 22 μm , and the distributions of 12- and 22- μm luminosities as a function of redshift are illustrated in Figures 8 and 9, respectively. The flux distribution does not reveal any clear differences between each galaxy type, and we see in the redshift distributions that type 1 and type 2 AGNs have relatively higher redshifts.

2.3. Derivation of Luminosity Function with $1/V_{\text{max}}$ method

Here, we derive the LFs following the $1/V_{\text{max}}$ method described by Schmidt (1968). The advantage of the $1/V_{\text{max}}$ method is that it allows us to compute the LF directly from the data; no parameter dependence or model assumptions are needed. The volume density $\phi(L)$ and its uncertainty $\sigma_{\phi(L)}$ are derived using the expressions:

$$\phi(L) = \sum_i^N \frac{1}{V_{\text{max},i}}, \quad (2)$$

$$\sigma_{\phi(L)} = \sqrt{\sum_i^N \frac{1}{V_{\text{max},i}^2}}, \quad (3)$$

where V_{max} is the maximum co-moving volume that would be enclosed at the maximum redshift at which the i th object could be detected. In the context of the cosmology we adopt, V_{max} is

$$V_{\text{max}}(z) = \frac{c}{H_0} \int_{\Omega} \int_{z_{\text{min}}}^{z_{\text{max}}} \frac{(1+z')^2 D_A^2}{\sqrt{\Omega_M(1+z')^3 + \Omega_\Lambda}} dz' d\Omega, \quad (4)$$

where D_A is the angular distance for a given redshift in our adopted cosmology, Ω is the solid angle of the SDSS DR8 spectroscopic region (7966 $\text{deg}^2 \sim 2.43$ str), z_{min} is the lower limit of the redshift bin considered, and z_{max} is the maximum redshift at which the object could be seen given the flux limit of the sample. Note that when z_{max} is smaller than the maximum of the redshift bin considered, $V_{\text{max}} = V(z_{\text{max}}) - V(z_{\text{min}})$. Otherwise, V_{max} is equal to the volume corresponding to the bin considered, $V_{\text{max}} = V_{\text{bin}}$. However, as z_{max} cannot be determined analytically, we calculated z_{max} numerically, using the following procedure.

The absolute magnitude (hereafter, we use the magnitude for descriptive purposes) of the object M observed to have an apparent magnitude m at a redshift z is

$$M = m - K(z) - 5 \log d_L(z) - 25, \quad (5)$$

where d_L is the luminosity distance (measured in Mpc) for a given redshift in our adopted cosmology, and $K(z)$ is the K-correction term, which is the redshift dependence of the magnitude of any object in a given wavelength band. When a source is artificially moved to the detection limit $m(z_{\max}) = m_{\min}$, Equation (5) becomes

$$M = m_{\min} - K(z_{\max}) - 5 \log d_{L_{\max}} - 25 , \quad (6)$$

where $d_{L_{\max}}$ is the maximum luminosity distance $d_L(z_{\max})$. Therefore, we numerically estimate z_{\max} by substituting z into Equations (5) and (6) step-wise in steps of Δz ($= 10^{-5}$ here) and iterating the above approach until the difference between the M values obtained from Equations (5) and (6) is minimized.

Note that when we calculate z_{\max} , the difference in the detection limits of the *WISE* and SDSS surveys should be considered because our *WISE*–SDSS sample is flux- (or magnitude-) limited. For the *WISE* samples, the detection limit is 0.9 mJy at 12 μm and 9.0 mJy at 22 μm . For the SDSS samples, the detection limit is 17.77 Petrosian r-band magnitude for galaxies and 19.10 PSF i-band magnitude for type 1 AGNs. Therefore, we calculated two values of z_{\max} for each survey considering these detection limits, and we adopted the smaller of two possible values in each case. To compute the maximum redshift for the *WISE* objects, $K(z)$ in Equation (5) was derived from the assumption that the spectral energy distribution (SED) of the objects in the IR region obeys a simple power law of $f(\nu) \propto \nu^{-\alpha}$, i.e.,

$$K_{\text{WISE}}(z) = 2.5(\alpha - 1) \log(1 + z) , \quad (7)$$

where the spectral index α is calculated using the 12- and 22- μm fluxes (f_{12} and f_{22} , respectively) as

$$\alpha = -\frac{\log\left(\frac{f_{22}}{f_{12}}\right)}{\log\left(\frac{\nu_{22}}{\nu_{12}}\right)} . \quad (8)$$

The frequencies at 12 and 22 μm , are ν_{12} and ν_{22} , respectively. In the case of SDSS galaxies, $K(z)$ in Equation (5) was computed using the K-correct (ver. 4.2) software of Blanton & Roweis (2007). We also assumed a power law for SDSS type 1 AGNs, with α calculated as

$$\alpha = -\frac{\log\left(\frac{f_r}{f_i}\right)}{\log\left(\frac{\nu_r}{\nu_i}\right)} , \quad (9)$$

where f_r and f_i are the PSF fluxes in r and i bands, respectively, as cataloged in the *SpecPhoto* table. The corresponding frequencies are ν_r and ν_i . Finally, for whichever maximum redshift is smaller, we adopted a maximum co-moving volume for each object i of

$$V_{\max,i} = \min[V_{\max,i}(\text{WISE}), V_{\max,i}(\text{SDSS})] , \quad (10)$$

where $V_{\max}(\text{WISE})$ and $V_{\max}(\text{SDSS})$ are obtained using $z_{\max}(\text{WISE})$ and $z_{\max}(\text{SDSS})$, respectively.

3. RESULTS

We present the MIR LFs from the *WISE*–SDSS sample, classified as discussed in Section 2.2, and show that the shapes of each LF are in agreement with previous studies. We then show each LF in different redshift bins, which indicate that AGNs (particularly type 1 AGNs) show a certain evolution compared to normal galaxies.

3.1. The 12- and 22- μm Luminosity Functions

The rest-frame 12- and 22- μm LFs (i.e., the volume density of the galaxies per unit absolute magnitude range) of our *WISE*–SDSS galaxies at $0.006 \leq z \leq 0.07$, computed with the $1/V_{\max}$ method, are shown in Figure 10. We confirm here the consistency between the LFs of *WISE* and *AKARI* (e.g., Toba et al. 2013). Toba et al. (2013) selected 243 galaxies at 9 μm and 255 galaxies at 18 μm from the *AKARI* MIR all-sky survey catalog, and by combining the *AKARI* data with the SDSS DR7 spectroscopic data, they constructed 9- and 18- μm LFs for the first time. To compare those LFs with ours in a similar redshift range, Figure 10 plots only local objects ($0.006 \leq z \leq 0.07$). Within this redshift range, the average value of the redshift (~ 0.04) is equal to that of Toba et al. (2013). Figure 10 also shows the *IRAS* 12- μm LFs (Rush et al. 1993; Fang et al. 1998) for comparison. These were derived from samples of 893 (Rush et al. 1993) and 668 (Fang et al. 1998) galaxies selected from the *IRAS* Faint Source Survey. Fang et al. (1998), in particular, corrected for the peculiar motion of the local supercluster. Note that for the 9- and 18- μm LFs we first converted the data by cross-identifying our *WISE*–SDSS sample with the *AKARI* MIR all-sky survey catalog, selecting the 200 *WISE*–SDSS-*AKARI* sources within the 3-arcsec search radius, and calculating conversion factors by plotting $\nu L_{\nu}(9 \mu\text{m})$ versus $\nu L_{\nu}(12 \mu\text{m})$ and $\nu L_{\nu}(18 \mu\text{m})$ versus $\nu L_{\nu}(22 \mu\text{m})$, as shown in Figure 11. We obtained the following conversion formulae:

$$\log[\nu L_{\nu}(12 \mu\text{m})] = (0.93 \pm 0.03) \times \log[\nu L_{\nu}(9 \mu\text{m})] + (0.43 \pm 0.26) , \quad (11)$$

$$\log[\nu L_{\nu}(22 \mu\text{m})] = (0.96 \pm 0.02) \times \log[\nu L_{\nu}(18 \mu\text{m})] + (0.37 \pm 0.18) . \quad (12)$$

The conversion uncertainty is represented in Figure 10 as the horizontal error bars. The shapes of the LFs obtained from previous studies (Rush et al. 1993; Fang et al. 1998; Toba et al. 2013) are in good agreement with our derived LFs.

Figure 12 presents the resultant LFs at 12 and 22 μm for each galaxy type for $0.006 \leq z \leq 0.3$. SFs make up the majority of the objects at low luminosities, while AGNs dominate the volume density at luminosities above $\sim 10^{11} L_{\odot}$. This tendency was also reported by Rush, Malkan, & Spinoglio (1993), who used 12- μm flux-limited samples from the *IRAS* Faint Source Catalogue (FSC). Figure 12 also shows that the relative number of AGNs changes with increasing MIR luminosity; at low luminosities, type 2 AGNs dominate the AGN population, whereas type 1 AGNs dominate at high luminosities. Toba et al. (2013) also recently reported a similar trend using *AKARI*. The fraction of type 2 AGNs thus changes with MIR luminosity, which can be interpreted as a luminosity dependence of the CF.

Figures 13 and 14 show the resultant LFs at 12 and 22 μm for each galaxy type in each of the six redshift bins ($0.006 \leq z < 0.05$, $0.05 \leq z < 0.1$, $0.1 \leq z < 0.15$, $0.15 \leq z < 0.2$, $0.2 \leq z < 0.25$, and $0.25 \leq z \leq 0.3$). The overall trends seen in Figure 12 are reproduced in these figures except for $z > 0.2$. For $z > 0.2$, type 1 and type 2 AGNs dominate the volume density over a wide range of luminosities, while for $z \leq 0.2$, their magnitude relationship changes remarkably with increasing MIR luminosity, as seen in Figure 12. At the same time, the overall magnitude relationship between AGNs also changes with increasing redshift; type 2 AGNs make up the majority of the AGNs at low redshift, while type 1 AGNs are the majority at high redshift. This change in the fraction of type 2 AGNs with redshift can be interpreted as a redshift dependence of the CF.

3.2. Evolution of Luminosity Functions

We examined the luminosity (density) evolution of the AGN population based on the 22- μm sample. Here, we fit the LFs for all galaxies and AGNs using the double-power law (Marshall et al. 1987):

$$\phi(L)dL = \phi^* \left\{ \left(\frac{L}{L^*} \right)^{-\alpha} + \left(\frac{L}{L^*} \right)^{-\beta} \right\}^{-1} \frac{dL}{L^*}, \quad (13)$$

where the free parameters are the characteristic luminosity L^* , the normalization factor ϕ^* , the faint-end slope α , and the bright-end slope β , respectively.

Figure 15 shows the best fit for each redshift bin. Four redshift bins ($0.006 \leq z < 0.05$, $0.05 \leq z < 0.1$, $0.1 \leq z < 0.2$, and $0.2 \leq z \leq 0.3$) are considered to keep a certain data point (if there are less than four degrees of freedom, then we cannot use the double-power law as a fit). The fit of the data in the nearest redshift bin ($0.006 \leq z < 0.05$) is shown in all panels for comparison, and to examine the evolution, fits with β fixed to the value of

that in the nearest redshift bin ($0.006 \leq z < 0.05$) are also shown. Comparing the LF of all galaxies with that of AGNs as a function of redshift, we see that the LF of all galaxies does not evolve considerably with redshift, whereas the LF of AGNs shows significant evolution. A comparison of the evolution of LFs for different AGN types (Figure 16) reveals that type 1 AGNs seem to exhibit more significant evolution than type 2 AGNs. However, this difference can arise from an incompleteness of type 2 AGNs, particularly at high redshifts ($z > 0.2$), due to the SDSS selection criterion (see also Section 4.3.2).

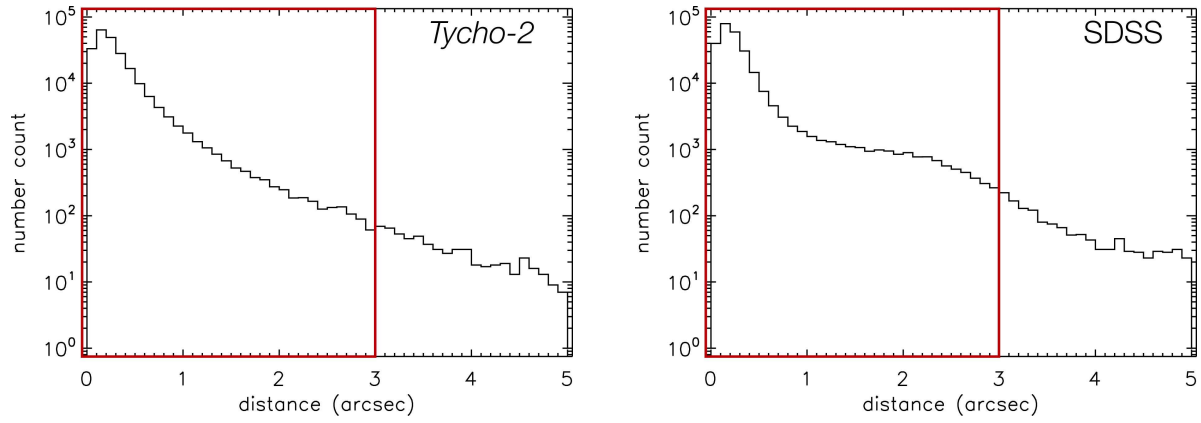


Fig. 2.— Histogram of the angular separation of *WISE* sources from the *Tycho-2* (left) and SDSS (right) coordinates. A search radius of 3 arcsec, as shown in red, was adopted for both sets. Cross-matching with the *Tycho-2* coordinates selected 225,547 objects within the search radius, while that with the SDSS coordinates selected 259,969 objects.

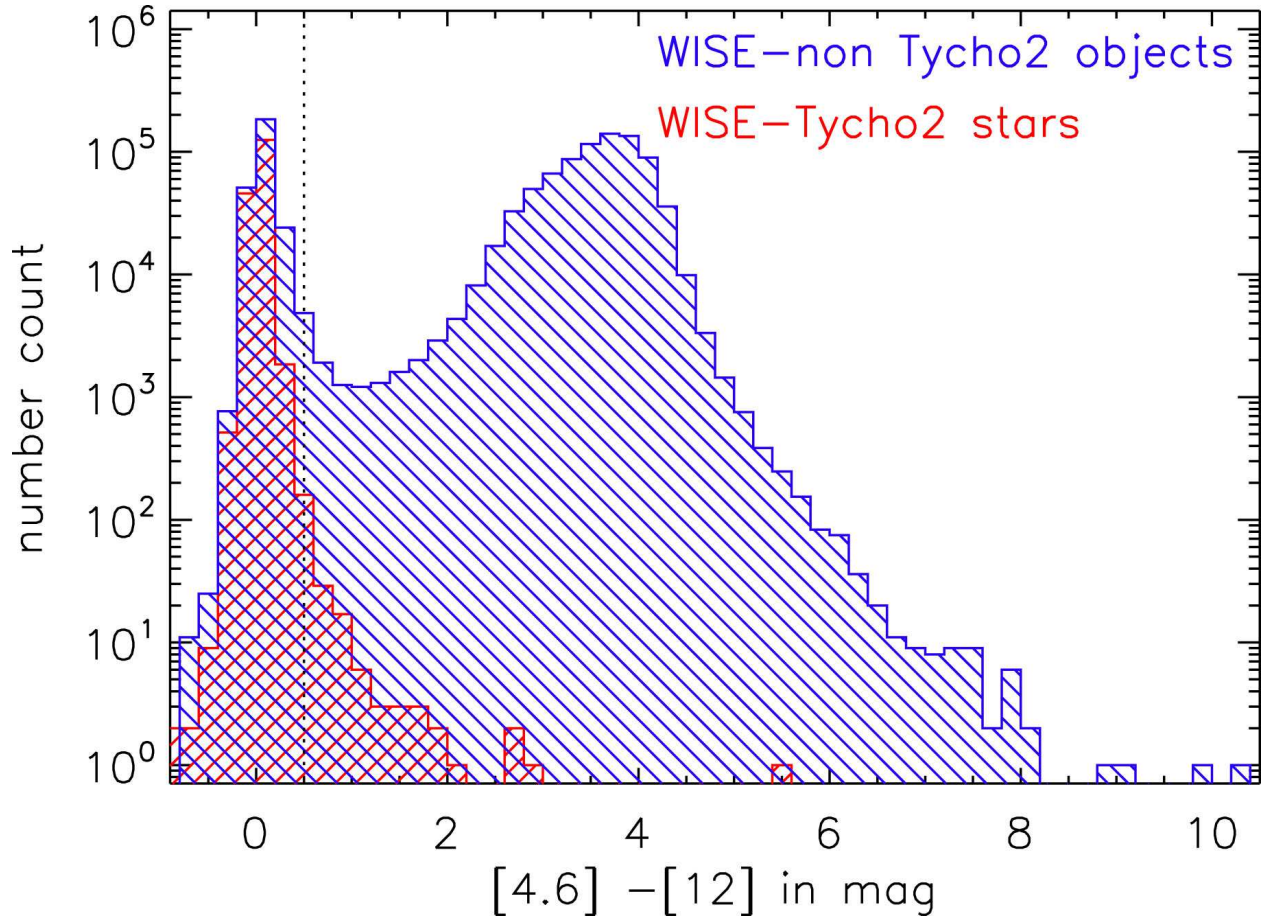


Fig. 3.— Color ($[4.6] - [12]$) distribution of the *WISE* sources. The blue region represents *WISE-non Tycho 2* objects, and the red region represents *WISE-Tycho 2* stars. The dotted line indicates the threshold of star–galaxy separation. Objects with $[4.6] - [12] \leq 0.5$ are removed as stars.

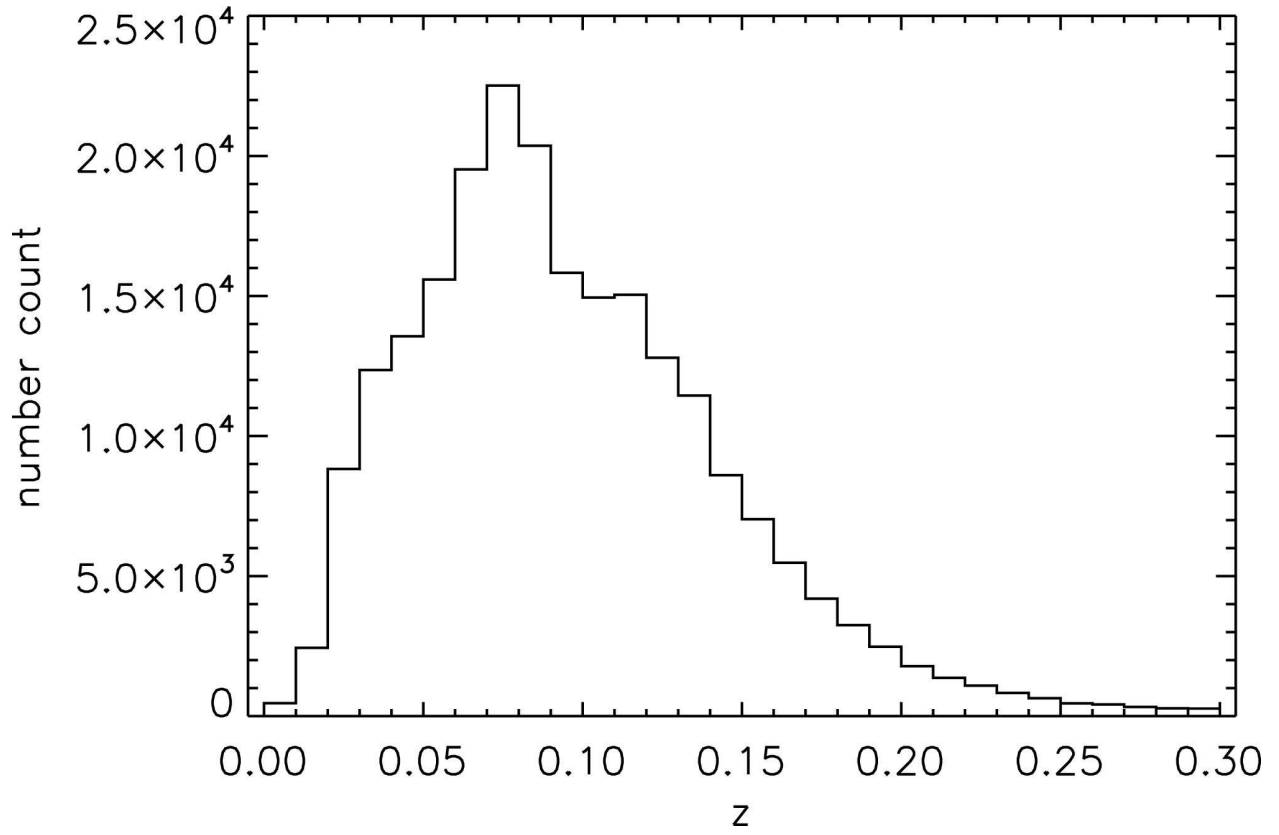


Fig. 4.— Redshift distribution of the 224,168 selected galaxies.

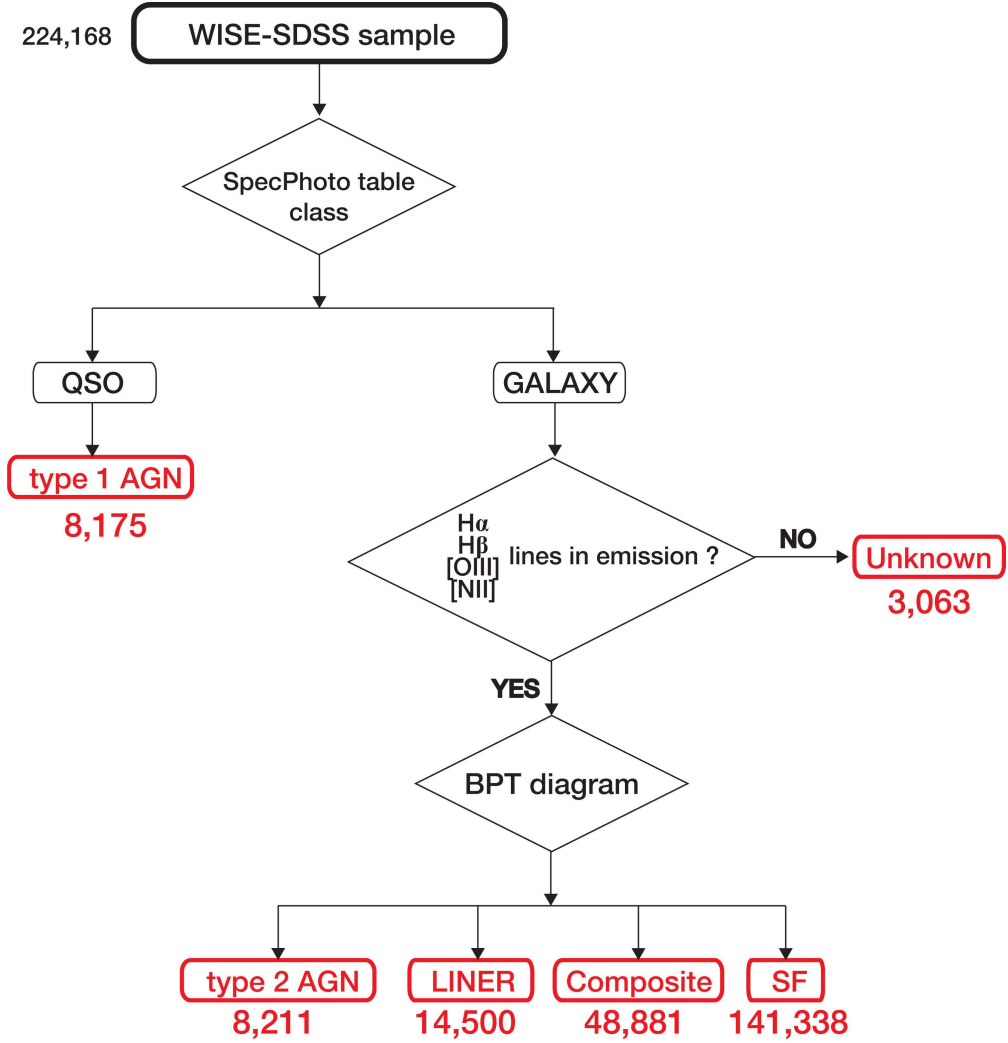


Fig. 5.— Outline of the type classification process.

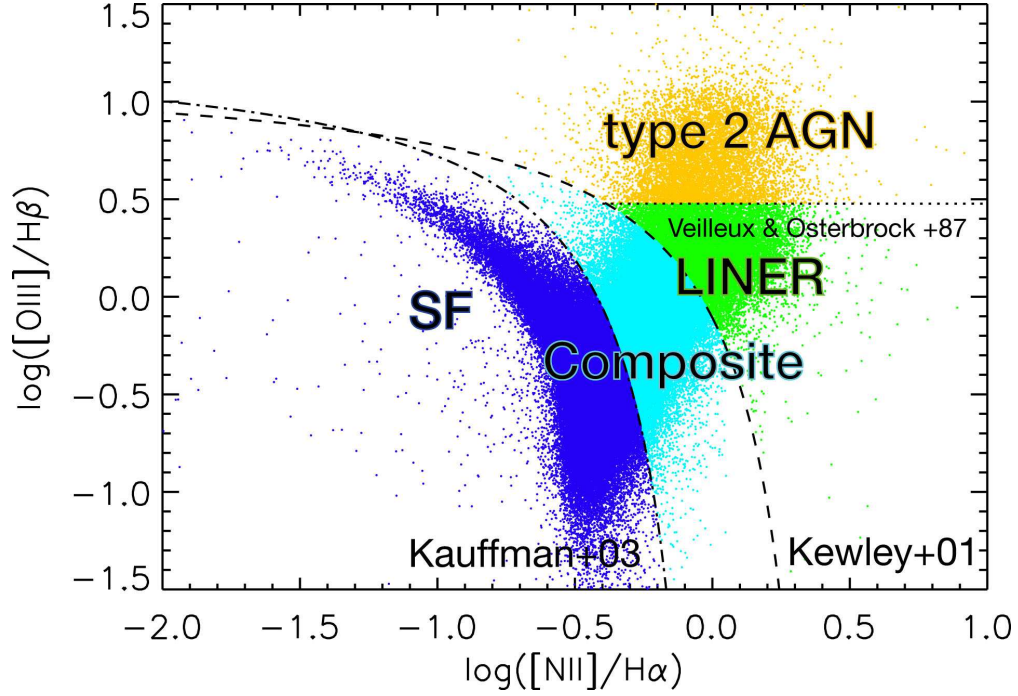


Fig. 6.— BPT diagram of the emission-line flux ratio $[\text{NII}]/\text{H}\alpha$ versus $[\text{OIII}]/\text{H}\beta$ for all the narrow-line galaxies for which line flux information is available. The dashed-dotted line is the criterion given by Kauffmann et al. (2003), the dashed line is the criterion given by Kewley et al. (2001), and the dotted line is the traditional scheme (see for example, Veilleux & Osterbrock 1987).

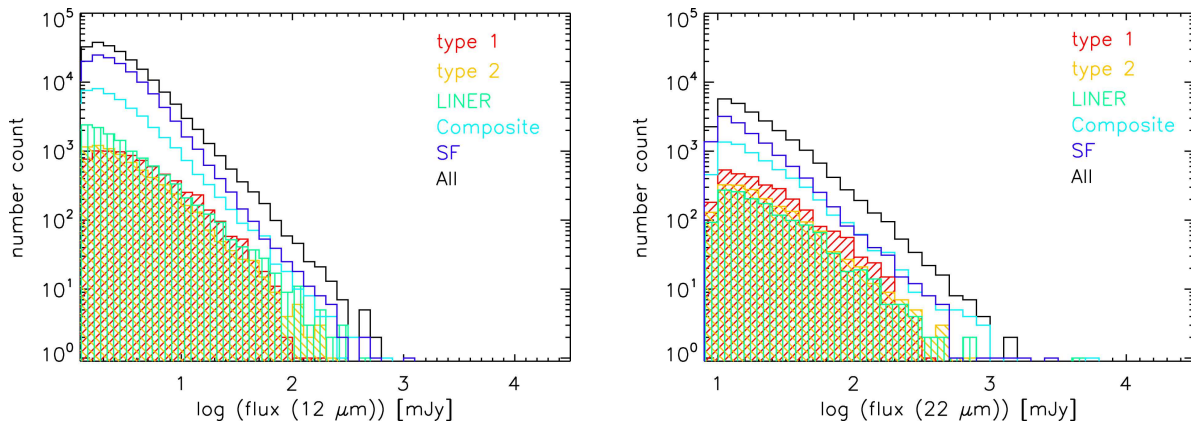


Fig. 7.— Flux distribution for each galaxy type at $12\ \mu\text{m}$ (left) and $22\ \mu\text{m}$ (right).

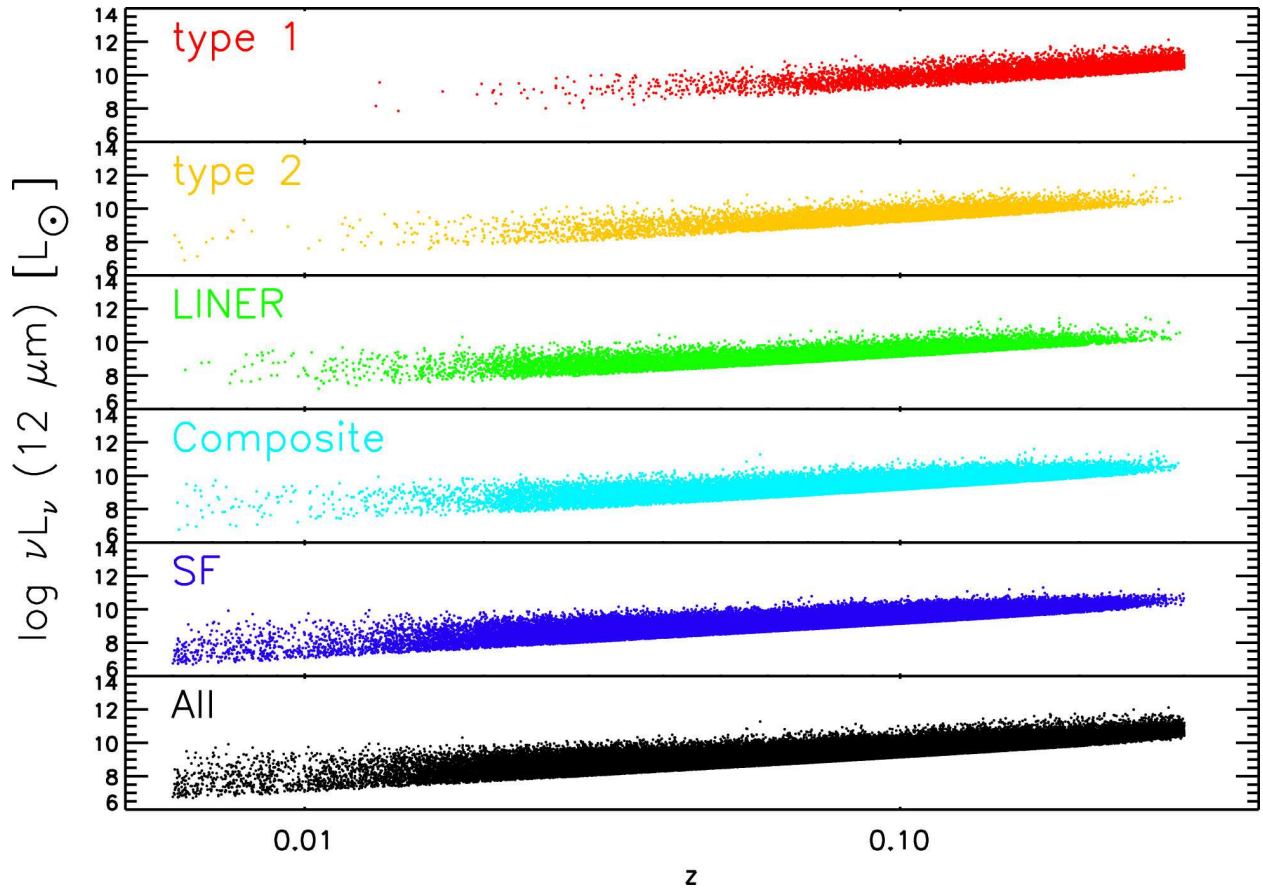


Fig. 8.— The 12- μm luminosities as a function of redshift for each galaxy type.

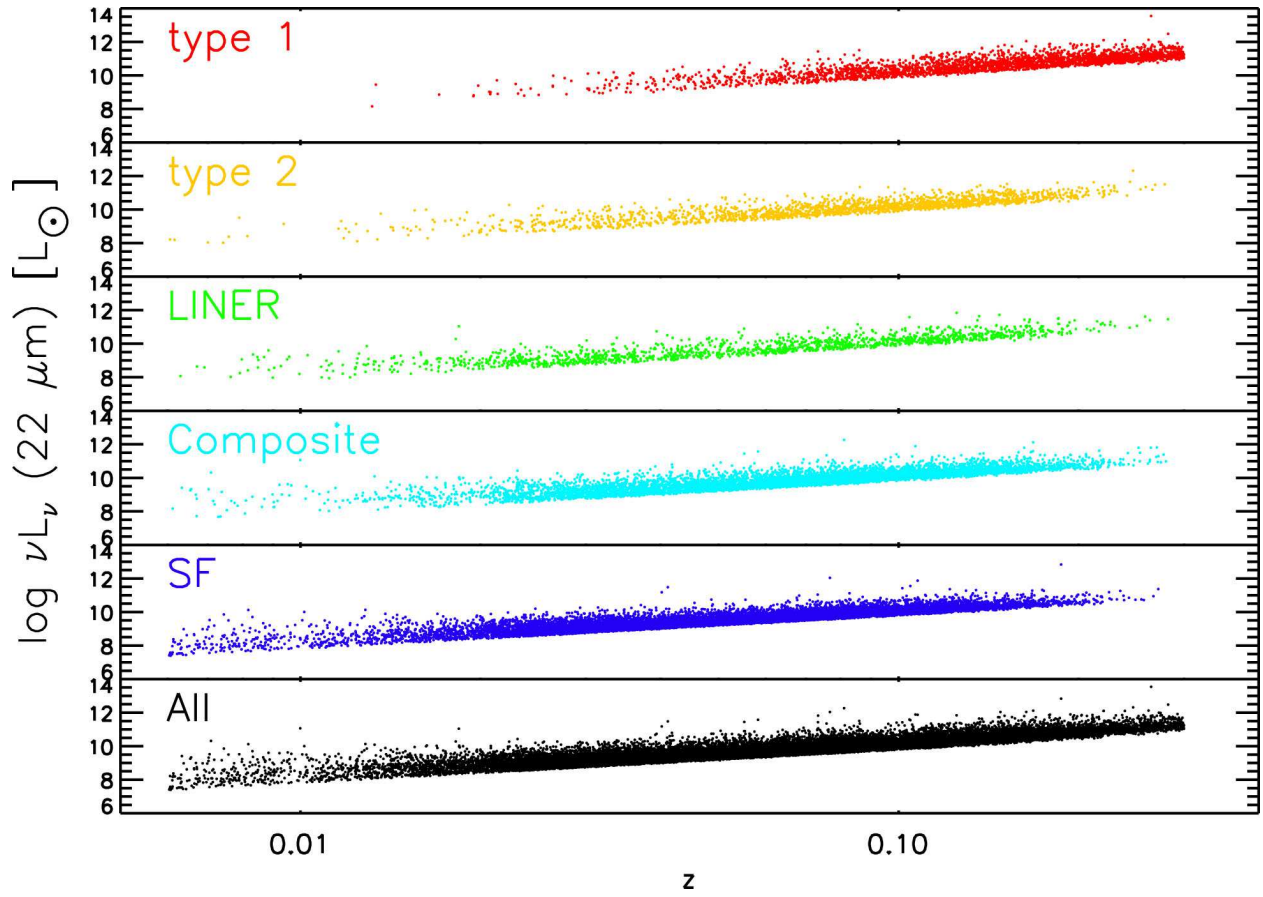


Fig. 9.— The 22- μm luminosities as a function of redshift for each galaxy type.

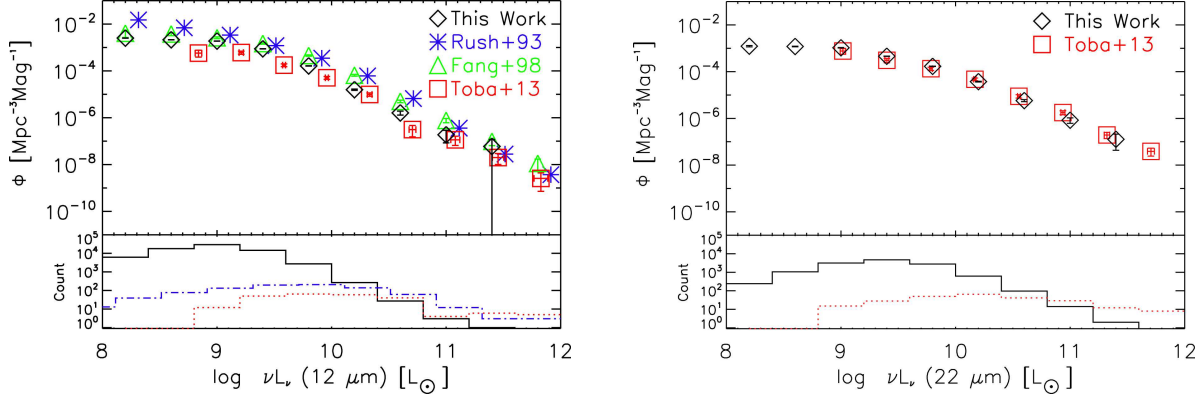


Fig. 10.— The 12- (left) and 22- (right) μm LFs for all galaxies for $0.006 \leq z \leq 0.07$. The 12- μm LFs from Rush et al. (1993) and Fang et al. (1998) and the 9- and 18- μm LFs from Toba et al. (2013) are also plotted for comparison. For the 9- and 18- μm LFs, we converted $\nu L_\nu(9, 18 \mu\text{m})$ to $\nu L_\nu(12, 22 \mu\text{m})$. The vertical error bars are calculated from the Poisson statistical uncertainty, and the horizontal error bars represent the uncertainty of the conversion to $\nu L_\nu(12, 22 \mu\text{m})$.

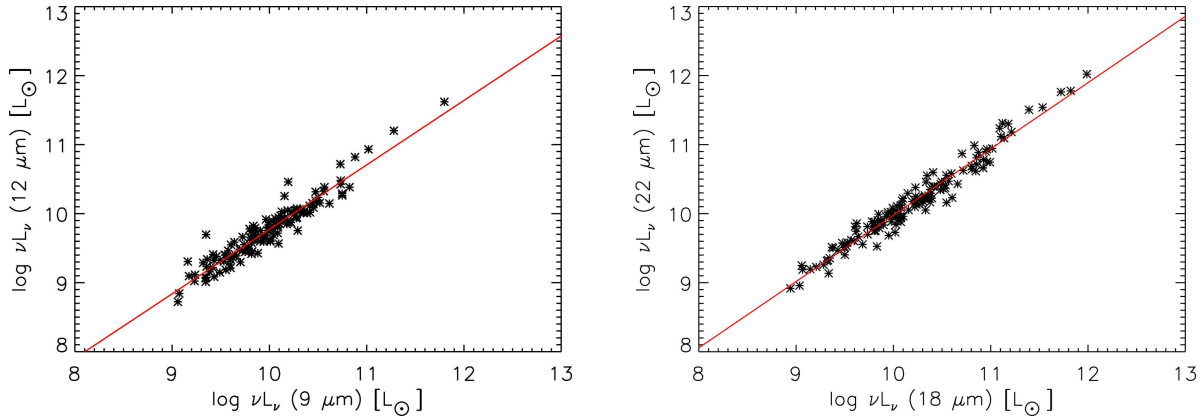


Fig. 11.— *WISE* 12- μm versus *AKARI* 9- μm luminosities (left) and *WISE* 22- μm versus *AKARI* 18- μm luminosities (right). The red dotted line shows the best-fit linear function.

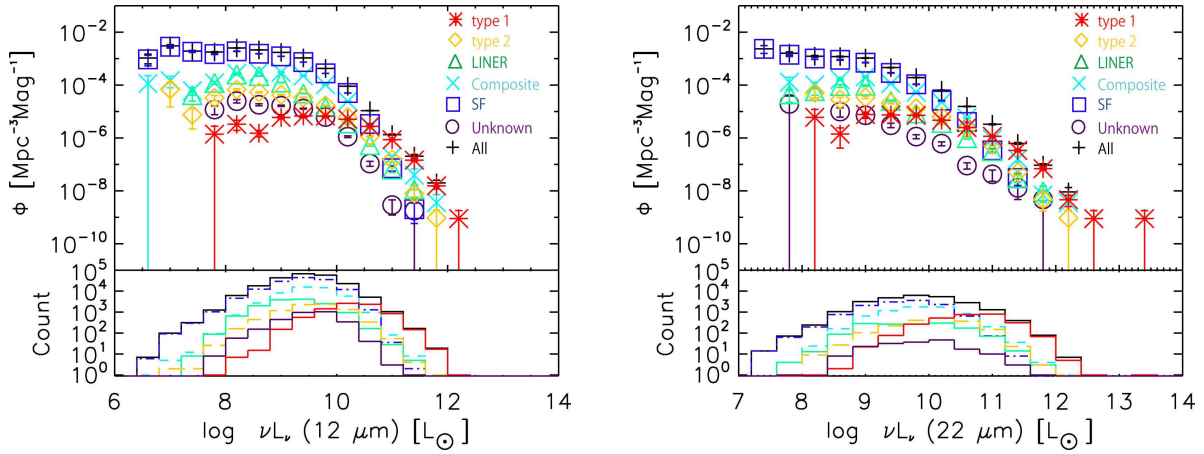


Fig. 12.— The 12- (left) and 22- (right) μm LFs for each galaxy type for $0.006 \leq z \leq 0.3$ plotted in terms of the space density as a function of luminosity. The error bars are calculated from the Poisson statistical uncertainty. The data used in these figures can be found in Tables 7, 8, and 9 (see Appendix B).

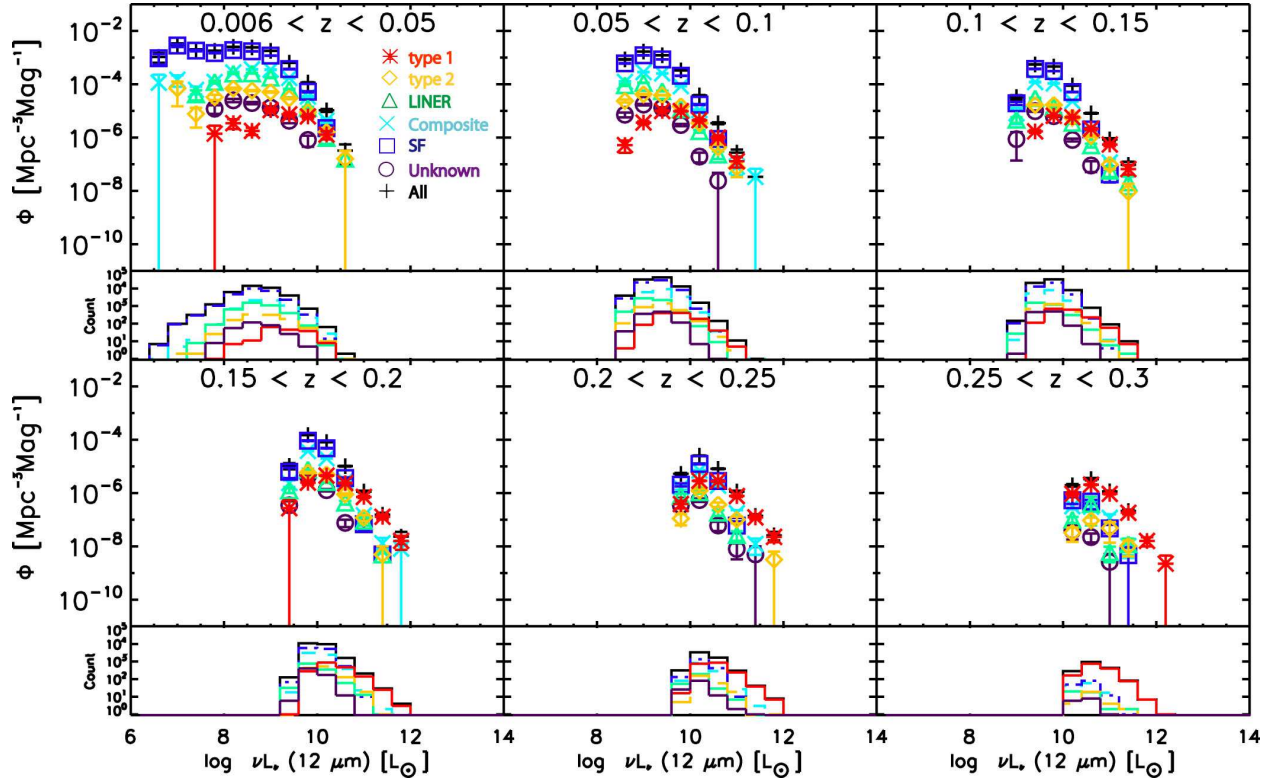


Fig. 13.— The 12- μ m LFs for each galaxy type in each redshift bin ($0.006 \leq z < 0.05$, $0.05 \leq z < 0.1$, $0.1 \leq z < 0.15$, $0.15 \leq z < 0.2$, $0.2 \leq z < 0.25$, and $0.25 \leq z \leq 0.3$). The data used in this figure can be found in Tables 7 and 8 (see Appendix B).

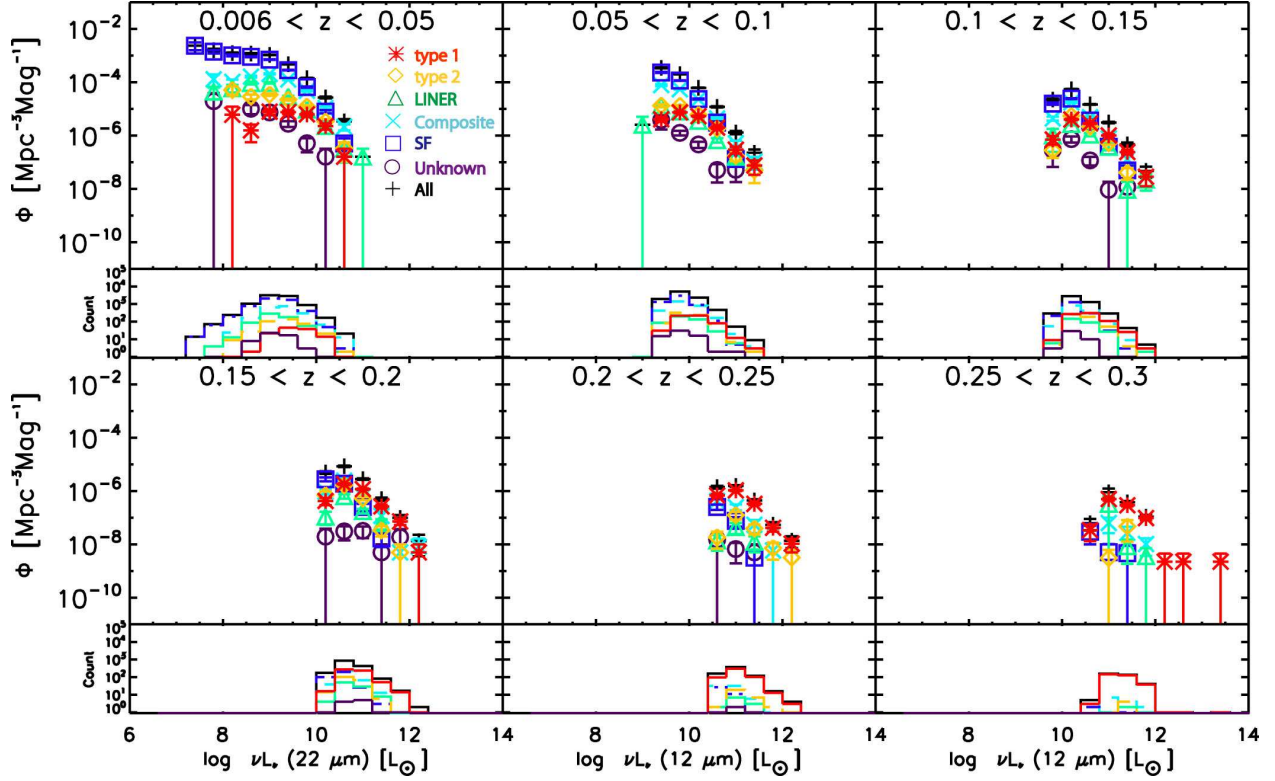


Fig. 14.— The 22- μm LFs for each galaxy type in each redshift bin ($0.006 \leq z < 0.05$, $0.05 \leq z < 0.1$, $0.1 \leq z < 0.15$, $0.15 \leq z < 0.2$, $0.2 \leq z < 0.25$, and $0.25 \leq z \leq 0.3$). The data used in this figure can be found in Tables 7 and 9 (see Appendix B).

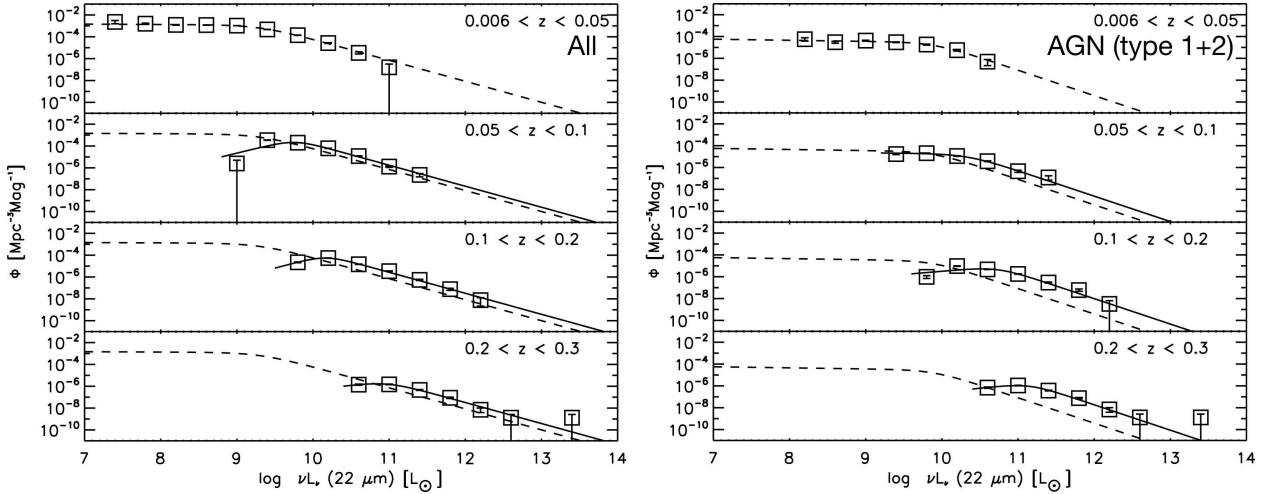


Fig. 15.— The 22- μm LFs for all galaxies (left) and AGNs (right) as a function of redshift. The dashed line represents the best fit function for $0.006 \leq z < 0.05$. The solid line represents the best fit function for a fixed bright-end slope β .

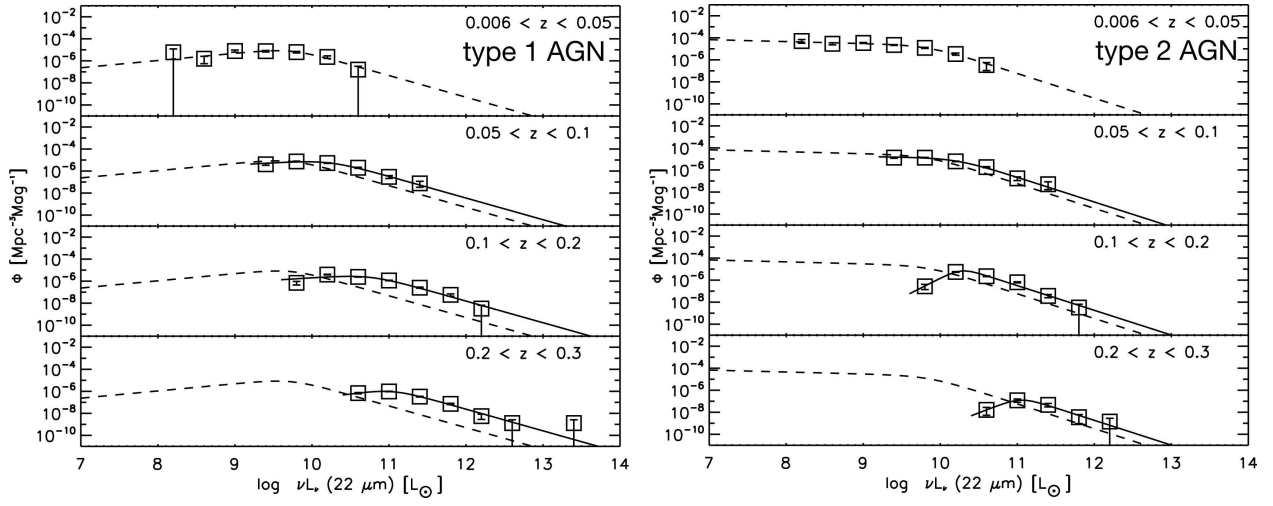


Fig. 16.— The 22- μm LFs for type 1 AGNs (left) and type 2 AGNs (right) as a function of redshift. The dashed line represents the best fit function for $0.006 \leq z < 0.05$. The solid line represents the best fit function for a fixed β .

4. DISCUSSION

In this section, we first consider the origin of the MIR emission by using an empirical method based on a *WISE* color–color diagram to extract sources that are dominated in the MIR by the active nucleus rather than their host galaxy. The luminosity and redshift dependence of the CF are then discussed in separate redshift bins to disentangle the luminosity and redshift correlations. We then consider the uncertainties in the luminosity dependence of the CF, such as the effect of (i) the Unknown galaxies, (ii) rejected objects in the sample selection, and (iii) optically elusive buried AGNs. Following that, we interpret the luminosity dependence in terms of two dust torus models (the receding torus model and the modified receding torus model). Finally, we compare our measurements of the CF with those of optical and hard X-ray results.

4.1. Origin of Mid-Infrared Emission in the *WISE*–SDSS Sample

Before estimating the CF, we consider the origin of the MIR emission in our AGN sample. In this study, we have assumed that the MIR luminosity of the AGNs is dominated by emission from the active nucleus. However, the origin of the MIR emission may not always be an active nucleus: the emission is sometimes likely to have a contribution from the underlying host galaxy, especially in the low-luminosity regime. We thus attempted to select the AGN-dominated MIR sources from the *WISE*–SDSS sample by examining their MIR colors. Recently, Mateos et al. (2012) suggested a highly complete and reliable MIR color selection method for AGN candidates using the 3.4-, 4.6-, and 12- μ m bands of *WISE*. They defined an “AGN wedge” based on the *WISE* and wide-angle Bright Ultrahard *XMM-Newton* survey (BUXS):

$$[3.4] - [4.6] = 0.315 \times ([4.6] - [12]), \quad (14)$$

and

$$[3.4] - [4.6] = -3.172 \times ([4.6] - [12]) + 7.624, \quad (15)$$

where the top and bottom boundaries of the wedge are obtained by adding y-axis ($[3.4] - [4.6]$) intercepts of +0.796 and -0.222 , respectively. They reported that for $L_{2-10\text{keV}} > 10^{44}$ erg s^{-1} ($\sim 10^{11} L_{\odot}$), where the AGN is expected to dominate the MIR emission, $97.1^{+2.2}_{-4.8}$ and $76.5^{+13.3}_{-18.4}$ percent of the BUXS type 1 and type 2 AGNs, respectively, meet the selection criteria, i.e., a large amount of BUXS AGNs lie in the wedge area. They also showed that compared to other methods in the literature (Jarrett et al. 2011; Stern et al. 2012), this technique offers the highest reliability and efficiency for detecting X-ray selected luminous AGN populations with *WISE*. Therefore, we used the AGN wedge to extract AGN-dominated

WISE sources. Hereinafter, we use the 22- μm luminosity as the MIR luminosity because the 12- μm flux is affected by PAH emission, which is unrelated to the presence of an active nucleus as mentioned in Section 2.2 and may introduce large uncertainties.

Figure 17 shows the MIR colors of the *WISE*–SDSS AGNs as a function of the MIR luminosity. SFs are also plotted in the same figure for comparison. The fraction of sources (AGNs) that are expected to be dominated by an active nucleus (i.e., those sources in the AGN wedge) increases with increasing MIR luminosity. At low luminosities, the MIR emission from an AGN is largely dominated by the large contribution from the underlying host galaxy. At high luminosities, however, the MIR emission originates mainly from the active nucleus. This is consistent with the result of Mateos et al. (2012).

Of the AGNs, type 2 AGNs are more affected by the star-forming activity in their host galaxies, especially in the low-luminosity regime, which was also reported by Mateos et al. (2012). This result indicates that there is a difference in the origin of the MIR emission of type 1 and 2 AGNs particularly in low-luminous AGNs, which could be interpreted as resulting from the fact that some low-luminous (type 2) AGNs are obscured by not only a dust torus but also their host SF. Figure 18 shows the distribution of the ratio of the [OIII] (5007 Å) to $\text{H}\beta$ luminosity (believed to be a good tracer for the strength of AGN activity) for the *WISE*–SDSS type 2 AGNs in and outside the AGN wedge. As shown in Figure 18, the peak of the distribution for type 2 AGNs in the AGN wedge is relatively larger than that of the type 2 AGNs outside the AGN wedge. To ensure the reliability of the ratio value, we examined the ratio for objects with a S/N greater than 10 in the [OIII] and $\text{H}\beta$ luminosities. In addition, Mateos et al. (2013), who adopted this technique for [OIII]-selected type 2 quasars (QSO2s) from the SDSS, reported that the fraction of QSO2s in the AGN wedge increases with increasing [OIII] luminosity. Therefore, we conclude that for less powerful AGNs, the host galaxy can contribute substantially to the MIR emission. Throughout the following discussion, we consider the AGN-dominated objects (i.e., those in the AGN wedge) and estimate the CF based on these objects. We note that the [OIII] luminosity includes a contribution from HII regions, particularly in metal-poor galaxies, which means that $L_{[\text{OIII}]} / L_{\text{H}\beta}$ may not always be a good tracer for AGN luminosity. Juneau et al. (2011) proposed the Mass-Excitation (MEx) diagnostic to identify AGNs on the basis of their [OIII]/ $\text{H}\beta$ and stellar masses. The MEx diagnostic is a possible way to investigate the differences in the properties of samples in and outside the AGN wedge. However, such calculations and an extended discussion of the properties based on the MEx diagram are beyond the scope of this paper.

Also, the luminosity and redshift dependences of the CF should be discussed using the complete sample for type 1 and 2 AGNs subject to certain criteria. Choosing objects in

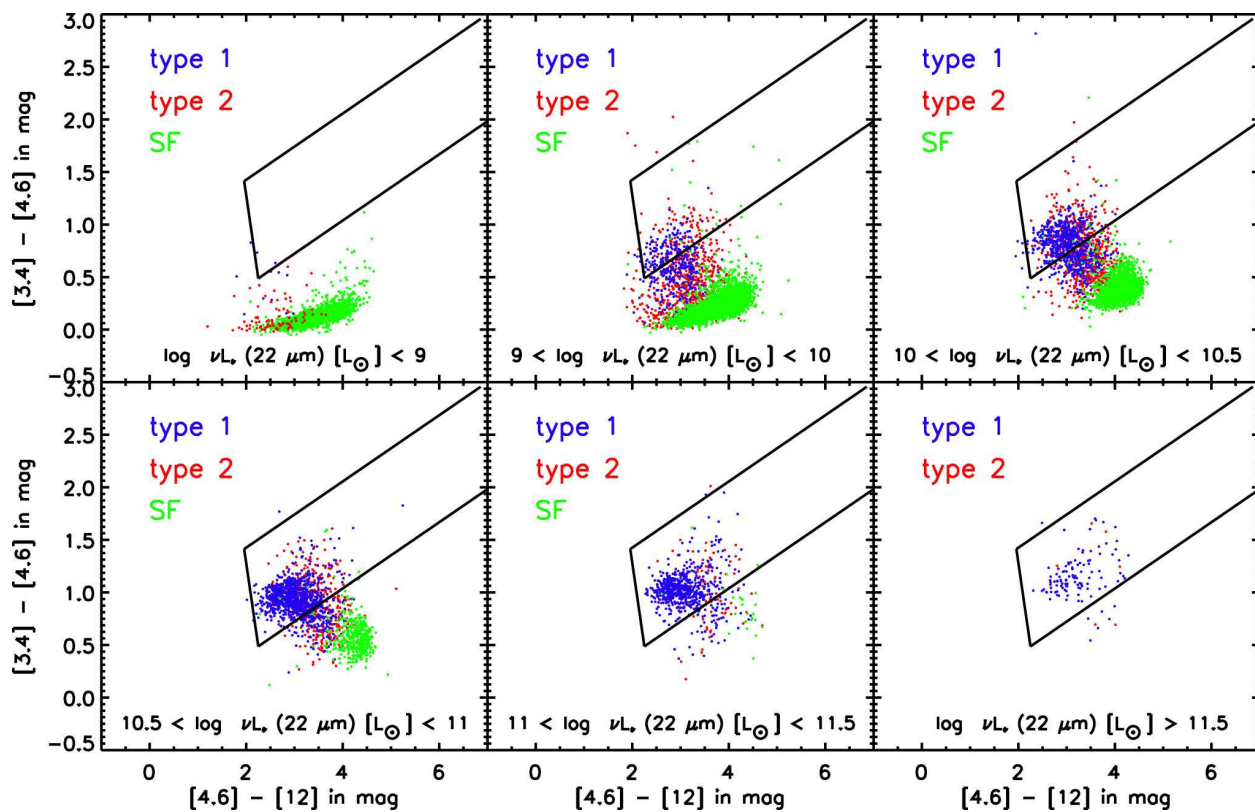


Fig. 17.— MIR color-color diagram for the *WISE*-SDSS sample at $22\ \mu\text{m}$: type 1 AGNs (blue), type 2 AGNs (red), and SFs (green) as a function of the $22\text{-}\mu\text{m}$ luminosity. The solid lines illustrate the AGN selection wedge as defined by Mateos et al. (2012).

the WISE–SDSS sample (i.e., extracting the objects in the AGN wedge) is equivalent to excluding AGNs that are affected by their host galaxies. Implementing the AGN wedge selection technique implies that the intrinsic ratio of type 1 and type 2 AGNs is the same in and outside the AGN wedge. This assumption is reliable because (i) the influence of the host galaxies for each type of AGN is comparable in the unified model, and (ii) the MIR luminosity of the nucleus for each AGN is also comparable as reported by Gandhi et al. (2009), who used high-resolution ($\sim 0.3\text{--}0.4$ arcsec) N-band filters for $12\text{-}\mu\text{m}$ imaging data obtained with the VISIR instrument on the 8-m Very Large Telescope.

4.2. Luminosity and Redshift Dependence of the Covering Factor

In an effort to constrain the structure of the hypothesized dust torus invoked by unification, we examine here the MIR luminosity dependence of the CF. We assume that the MIR luminosity of the AGNs is dominated by emission from the active nucleus (see Section 4.1), and we also assume that the MIR emission is independent of the optical classification, i.e., type 1 and type 2 AGNs should have similar continuum MIR fluxes at any given intrinsic AGN luminosity (see e.g., Horst et al. 2008; Gandhi et al. 2009). By integrating the LFs of the type 1 and type 2 AGNs separately, we obtain the number density Φ for each AGN:

$$\Phi = \int_L \phi(L) dL \sim \sum_i \phi_i(L) \Delta L. \quad (16)$$

Using these number densities, the CF and its uncertainty σ_{CF} can be estimated as

$$CF = \frac{\Phi_2}{\Phi_1 + \Phi_2}, \quad (17)$$

and

$$\sigma_{CF} = CF \times \sqrt{\left(\frac{\sigma_{\Phi_{1+2}}}{\Phi_{1+2}}\right)^2 + \left(\frac{\sigma_{\Phi_2}}{\Phi_2}\right)^2}, \quad (18)$$

where Φ_1 and Φ_2 are the type 1 and type 2 AGN number densities, respectively, and σ_{Φ_1} and σ_{Φ_2} are the associated errors. Note that $\Phi_{1+2} \equiv \Phi_1 + \Phi_2$ and $\sigma_{\Phi_{1+2}} \equiv \sqrt{\sigma_{\Phi_1}^2 + \sigma_{\Phi_2}^2}$.

A point of caution here is that our flux-limited sample produces a strong artificial correlation between the redshift and luminosity (see Figures 8 and 9). Thus, it is difficult to decide whether it is the redshift or the luminosity that is the more fundamental physical variable that correlates with the CF if a sample for all luminosity and all redshift ranges is used for the estimation. To test the intrinsic dependence of the CF on the luminosity and redshift, we have to remove the influence of the z – L correlation. A simple way to do

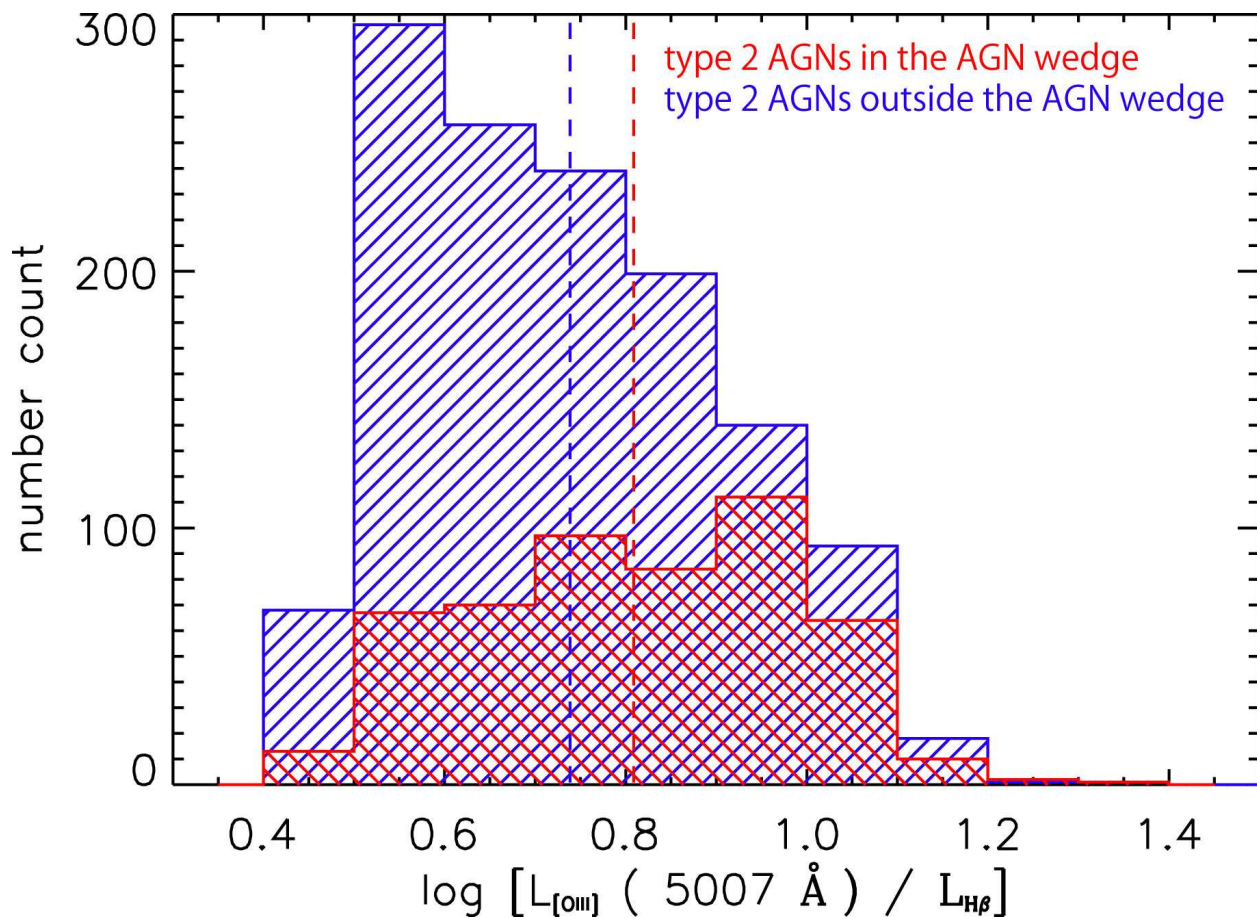


Fig. 18.— Distribution of the ratio of the [OIII] to $H\beta$ luminosity for type 2 AGNs in (red) and outside (blue) the AGN wedge as defined by Mateos et al. (2012). The dashed lines represent the mean value of $\log[L_{[\text{OIII}]} (5007 \text{ \AA}) / L_{\text{H}\beta}]$ for each subsample.

this is to analyze the CF in separate redshift bins. Hasinger (2008), who also used this diagnostic method, reported that the same trend toward a decreasing absorption fraction (which corresponds to the CF) as a function of X-ray luminosity, as observed in the total sample, was seen in each of the redshift bins. We note here that the redshift interval is optimized to keep the data points more or less equal for each redshift bin but only for $z \leq 0.2$ because the number of objects is limited and the SDSS survey may be incomplete, especially for type 2 AGNs for $z > 0.2$. It should also be noted that we assume the CF does not change within each interval, and it is under this assumption that we test the luminosity dependence of the CF.

In addition to considering Sy2 galaxies as type 2 (obscured) AGNs, we note that some LINERs and Composites can also show type 2 AGN-like properties. To take this into account, we also estimated four alternative CFs that included these galaxies as type 2 AGNs:

1. Sy2s
2. Sy2s + LINERs
3. Sy2s + Composites
4. Sy2s + LINERs + Composites

We reiterate here that all the sources used in calculating the CF are expected to be AGN dominant (i.e., in the AGN wedge). Figure 19 shows these CFs as a function of the MIR luminosity in different redshift bins; the CF values are also listed in Table 3. In the $0.006 \leq z < 0.1$ redshift range (see the left and middle panel in Figure 19), the CF does not change with MIR luminosity significantly within error, although the slope of the linear function that we fitted shows a negative correlation. In the $0.1 \leq z \leq 0.2$ redshift bin, however, we can see that the CF does decrease with an increase in the MIR luminosity, regardless of the choice of type 2 AGN classification criteria.

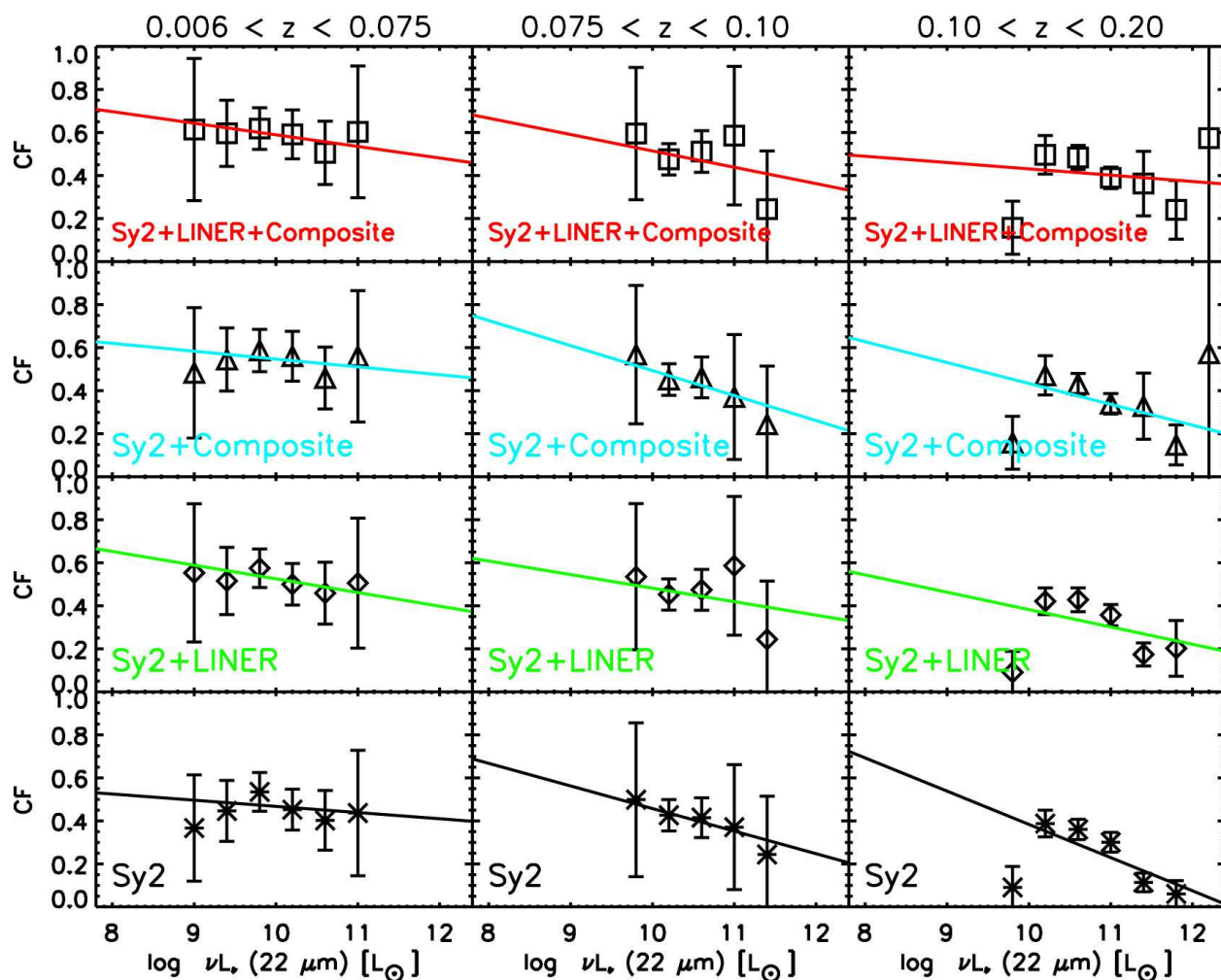


Fig. 19.— Variation in the CF with the 22- μm luminosity in different redshift bins for AGN-dominated MIR sources. The solid line shows the best-fit linear function determined in each redshift bin.

Table 3. CFs as a function of the 22- μm luminosity for each type 2 AGN definition.

log L	Sy2s		Sy2s + LINERs		Sy2s + Composites		Sy2s + LINERs + Composites	
	CF	σ_{CF}	CF	σ_{CF}	CF	σ_{CF}	CF	σ_{CF}
$0.006 \leq z < 0.075$								
9.00	0.37	0.25	0.55	0.32	0.48	0.30	0.61	0.33
9.40	0.45	0.14	0.52	0.16	0.54	0.15	0.60	0.15
9.80	0.53	0.09	0.57	0.09	0.59	0.10	0.62	0.10
10.2	0.45	0.09	0.50	0.10	0.56	0.12	0.59	0.11
10.6	0.40	0.14	0.46	0.14	0.46	0.14	0.51	0.15
11.0	0.44	0.29	0.51	0.30	0.56	0.31	0.60	0.31
$0.075 \leq z < 0.1$								
9.80	0.50	0.36	0.53	0.34	0.57	0.32	0.60	0.31
10.2	0.43	0.07	0.45	0.07	0.45	0.07	0.48	0.07
10.6	0.42	0.09	0.47	0.10	0.46	0.09	0.51	0.10
11.0	0.37	0.29	0.59	0.32	0.37	0.29	0.59	0.32
11.4	0.24	0.27	0.24	0.27	0.24	0.27	0.24	0.27
$0.1 \leq z \leq 0.2$								
9.80	0.09	0.10	0.09	0.10	0.16	0.12	0.16	0.12
10.2	0.39	0.06	0.42	0.06	0.47	0.09	0.50	0.09
10.6	0.36	0.05	0.43	0.06	0.43	0.05	0.48	0.06
11.0	0.30	0.05	0.36	0.05	0.34	0.05	0.39	0.05
11.4	0.11	0.04	0.17	0.05	0.33	0.15	0.36	0.15
11.8	0.06	0.06	0.20	0.13	0.15	0.09	0.24	0.14
12.2	0.57	0.70	0.57	0.70
$0.006 \leq z \leq 0.15$								
9.00	0.36	0.25	0.55	0.33	0.48	0.31	0.62	0.34
9.40	0.44	0.14	0.52	0.16	0.55	0.15	0.60	0.15
9.80	0.52	0.08	0.56	0.08	0.59	0.09	0.62	0.09
10.2	0.47	0.05	0.51	0.05	0.55	0.07	0.58	0.07
10.6	0.37	0.04	0.42	0.04	0.43	0.04	0.48	0.05
11.0	0.28	0.05	0.37	0.07	0.34	0.06	0.42	0.07
11.4	0.14	0.07	0.16	0.07	0.29	0.11	0.31	0.11
11.8	0.54	0.40	0.54	0.40
$0.006 \leq z \leq 0.2$								
9.00	0.36	0.26	0.55	0.33	0.48	0.31	0.62	0.34
9.40	0.44	0.14	0.52	0.16	0.55	0.15	0.60	0.15
9.80	0.52	0.08	0.56	0.08	0.59	0.09	0.62	0.09

This result has been reported several times, for example, by Maiolino et al. (2007), who found that the MIR spectra of 25 AGNs taken by the infrared spectrograph (IRS) on board the *Spitzer Space Telescope* showed a negative correlation between $\nu L_{6.7}/\nu L_{5100}$ (which corresponds to the CF) and the [OIII] λ 5007 line luminosity ($L_{6.7}$ and L_{5100} are the continuum luminosities at rest-frame wavelengths of 6.7 μ m and 5100 \AA , respectively). Burlon et al. (2011), who constructed AGN samples in the local universe ($z < 0.1$) using data from the *Swift*-BAT telescope and calculated the X-ray (15–55 keV) LFs of absorbed and unabsorbed AGNs that were classified according to their absorbing column density (N_H), also found a negative correlation between the fraction of absorbed AGNs and the hard X-ray luminosity. Recently, some studies based on *WISE* data have supported the luminosity dependence of the CF. Assef et al. (2013) presented the distribution of reddening in their AGN sample selected using the *WISE* color in a 9-deg² NOAO Deep Wide-Field Survey Boötes field. They found that the type 1 AGN ($E(B - V) < 0.15$) fraction is a strong function of the AGN bolometric luminosity (in that case, the fraction of type 1 AGNs increases with bolometric luminosity). On the basis of the *WISE* and SDSS data, the CF of quasars measured by the ratio of the torus IR luminosity to the bolometric luminosity was also found to decrease with increasing bolometric luminosity (Mor & Trakhtenbrot 2011; Calderone et al. 2012; Ma & Wang 2013; Roseboom et al. 2013; Gu 2013). More recently, Toba et al. (2013) also reported a similar trend based on the *AKARI* MIR data. However, these findings were from samples containing several hundred objects. In contrast, Figure 19 includes 3,000 AGNs in total. Therefore, compared to these previous studies, our results are statistically robust. Furthermore, the large number of AGNs allows not only for different definitions of type 2 AGNs but also for omitting the influence of the contribution from their host galaxies and enables us to estimate the luminosity dependence of the CF considering only the AGN-dominated MIR objects. The *WISE* results also strongly support our previous *AKARI* results (Toba et al. 2013).

We note that the luminosity dependence of the CF we confirmed here is slightly weaker

Table 3—Continued

log L	Sy2s		Sy2s + LINERs		Sy2s + Composites		Sy2s + LINERs + Composites	
	CF	σ_{CF}	CF	σ_{CF}	CF	σ_{CF}	CF	σ_{CF}
10.2	0.47	0.05	0.51	0.05	0.55	0.07	0.58	0.07
10.6	0.38	0.04	0.44	0.04	0.45	0.04	0.49	0.04
11.0	0.29	0.04	0.36	0.05	0.33	0.04	0.40	0.05
11.4	0.11	0.04	0.17	0.05	0.26	0.09	0.30	0.09
11.8	0.06	0.06	0.19	0.12	0.15	0.09	0.23	0.13
12.2	0.56	0.69	0.56	0.69

than previous studies. This difference may be caused by removing a large number of objects that are affected by the contribution of their host galaxies particularly in the low-luminosity regime. Recently, Lusso et al. (2013) estimated the CF by computing the ratio of re-processed MIR emission to intrinsic nuclear bolometric luminosity. By subtracting the contribution from the host galaxies and correcting the reddening effect, they showed that the obtained CF is smaller than that without any correction especially for low luminosity, which yields a relatively weak luminosity dependence of the CF. Our result shows a similar tendency. Ultimately, we conclude that the CF depends on the MIR luminosity.

The redshift dependence of the CF based on the acknowledgment of its luminosity dependence is derived following the diagnostic method presented in Hasinger (2008). In that study, the data in each redshift bin was also fitted with a linear function. Hasinger (2008) first estimated the average value of the slope of the relation between the CF and luminosity in the redshift range 0.2–3.2 and then estimated the normalization value at a luminosity of $\log(L_X) = 43.75 \text{ erg s}^{-1}$, in the middle of the observed range, as a function of the redshift by keeping the slope fixed to the average value. To quantitatively examine the dependence of the CF on redshift, an attempt was made to correct the systematic selection effects, and it was found that this corrected normalization value (i.e., the CF at $\log(L_X) = 43.75 \text{ erg s}^{-1}$) increased with redshift up to $z \sim 2$. This method thus offers a simple way to examine the redshift dependence of the CF. In the case of our flux-limited sample, however, the above analysis would be still affected by the luminosity dependence of the CF because our data does not cover the same redshift range given any luminosity unlike Hasinger’s sample. This yields an “unfair” normalization value as a result of fitting in each separate redshift bin, and so to evaluate the data correctly using this method, we need to collect a complete sample that fills the luminosity–redshift space.

We selected a complete sample in luminosity–redshift space that enabled us to investigate the redshift dependence of the CF from unbiased data but at the cost of reducing the number of objects in the sample. The sample was divided into three redshift bins and four luminosity bins. The redshift bins were $0.05 \leq z < 0.1$, $0.1 \leq z < 0.15$, and $0.15 \leq z \leq 0.2$ in a luminosity range of $10^{10-11.6} L_\odot$. We note that these redshift bins are different from those presented in Figure 19 to ensure that the same luminosity range is covered in each redshift bin. In the same manner as Hasinger (2008), we investigated the dependence of the CF on redshift as follows: We first estimated the average value of the slope in the redshift range 0.05–0.2, and the estimated slope values for each type 2 definition are listed in Table 4, which are in good agreement with those of Hasinger (0.25 ± 0.06) at $0.015 < z < 0.2$.

We then estimated the normalization value at a luminosity of $\log[\nu L_\nu(22 \mu\text{m})] = 10.6$

L_{\odot} , in the middle of the observed range, as a function of redshift by keeping the slope fixed to the average value (Figure 20). We found that the data are well fitted by the linear function in each redshift bin. Figure 21 shows the normalization value of the CF at $\log[\nu L_{\nu}(22 \mu\text{m})] = 10.6 L_{\odot}$ as a function of the redshift. We found that the CF did not change significantly with the redshift for any type 2 AGN classification criteria. Therefore, we concluded that the CF did not have a redshift dependence for $z \leq 0.2$.

4.3. Uncertainties in the Luminosity Dependence

We consider in this section the uncertainties in the luminosity dependence of the CF. As described in Section 4.2, we employed the AGN wedge selection technique and investigated the luminosity dependence for selected AGN-dominated MIR objects. However, we also consider the uncertainties without using this technique for the benefit of users who refer to the data in Appendix C.

4.3.1. Influence of the Unknown galaxies

A total of 3,060 and 179 galaxies were classified as Unknown galaxies in the 12- and 22- μm samples, respectively. Even though these galaxies only constitute a small portion of the samples (1.4% and 0.7%, respectively), it is not clear that their influence on the CF can be ignored. Therefore, we estimated the effect of these objects by considering the most extreme possibility, i.e., all Unknown galaxies are type 2 AGNs. We should note that we investigated the influence using a sample in all redshift ranges because the number of Unknown galaxies is too small to estimate the CF with a high accuracy if they are divided into separate redshift bins as in Figure 19. We here show the result when considering the AGN wedge. As shown in Figure 22, the CF for this case also decreases with increasing luminosity. In the case of the all sample including the outside the AGN wedge, we also see a similar trend (see Figure 31 in Appendix C), and so we conclude that the influence of the Unknown galaxies can be

Table 4. Average value of the slope of the fitted linear function in each redshift bin.

	average value of slope
Sy2	-0.19 ± 0.06
Sy2 + LINER	-0.16 ± 0.06
Sy2 + Composite	-0.18 ± 0.07
Sy2 + LINER + Composite	-0.12 ± 0.08

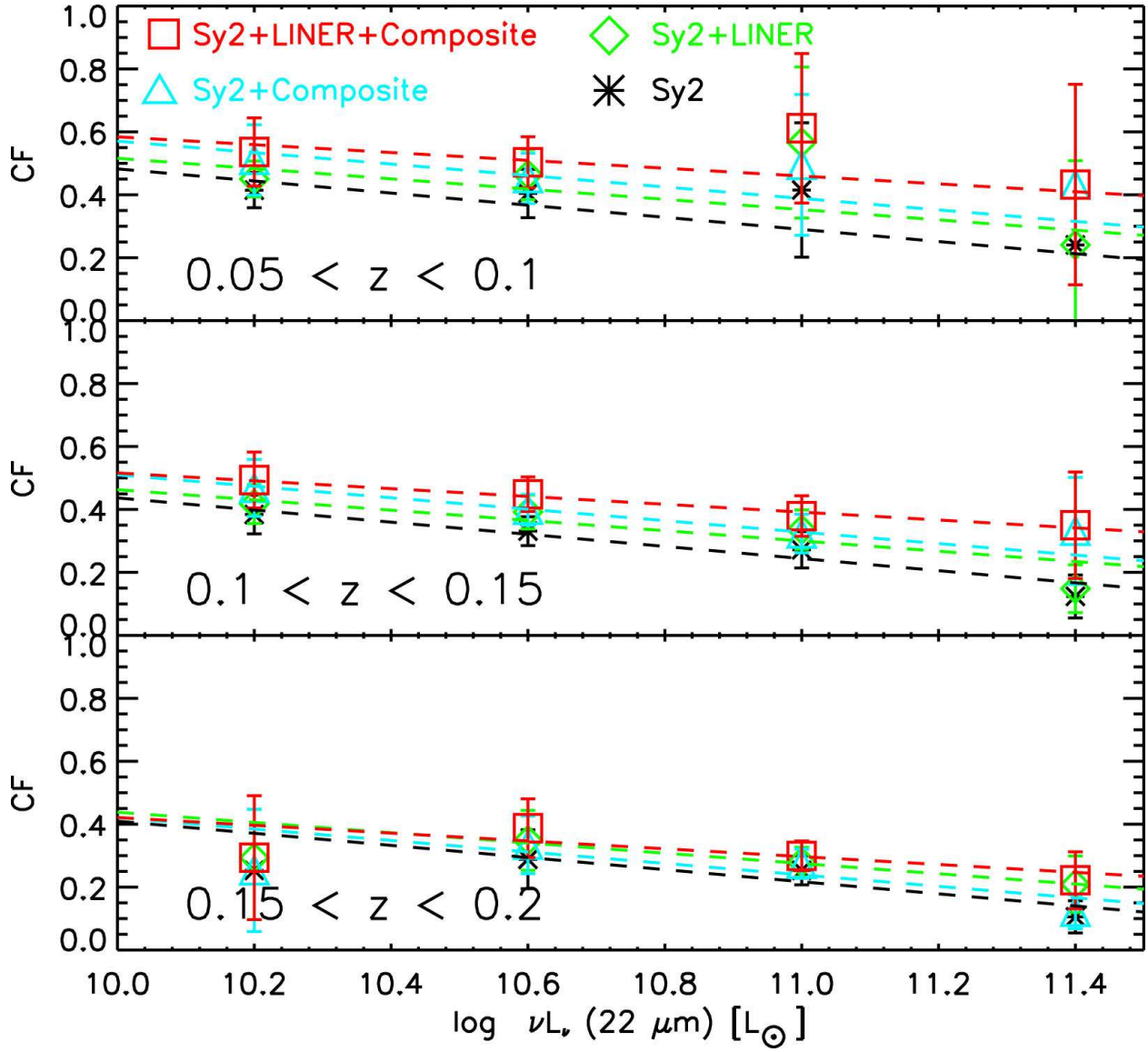


Fig. 20.— Variation in the CF with the 22- μm luminosity in different redshift bins. The dashed line shows the best-fit linear function with the slope fixed to the average value.

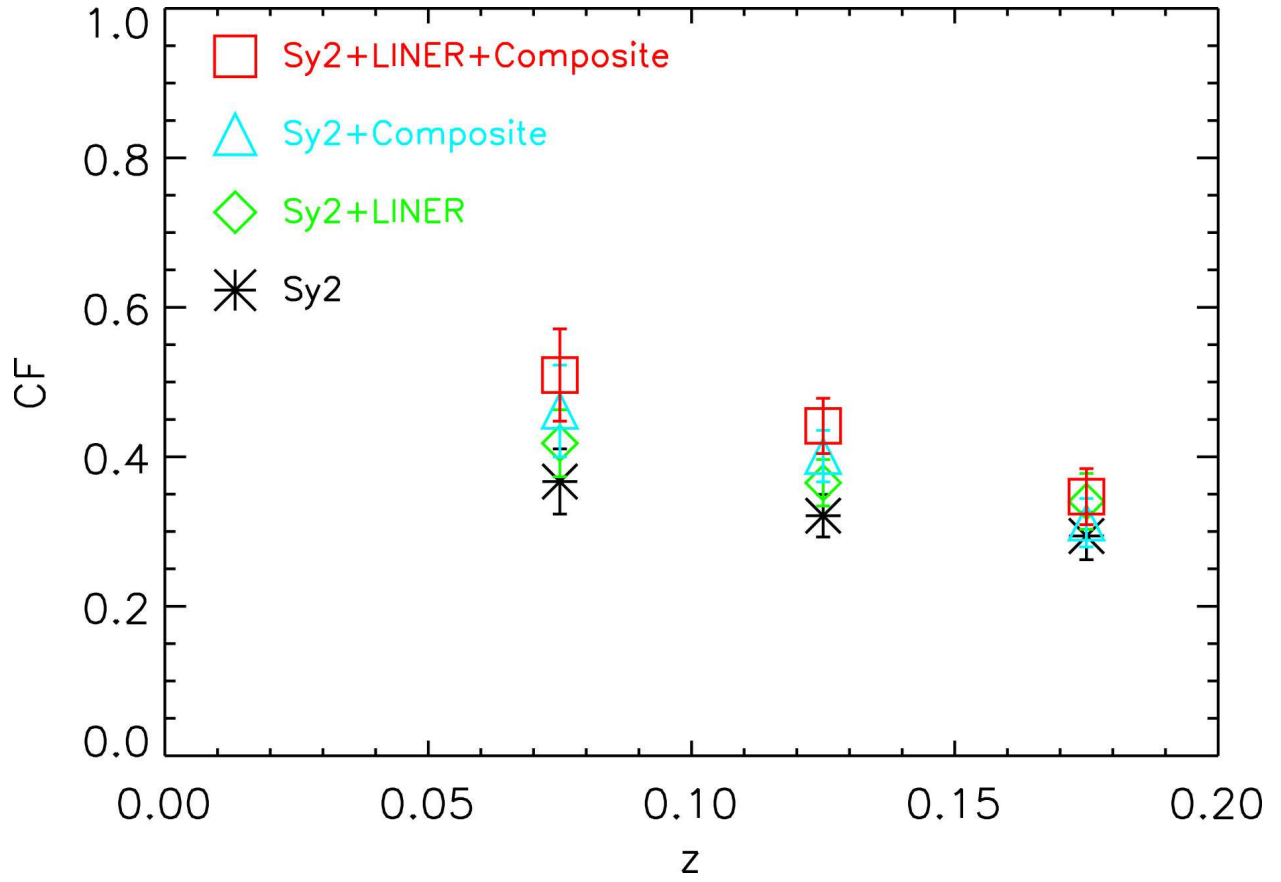


Fig. 21.— Dependence of the normalization of the CF at $\log[\nu L_\nu(22 \mu\text{m})] = 10.6 L_\odot$ on redshift.

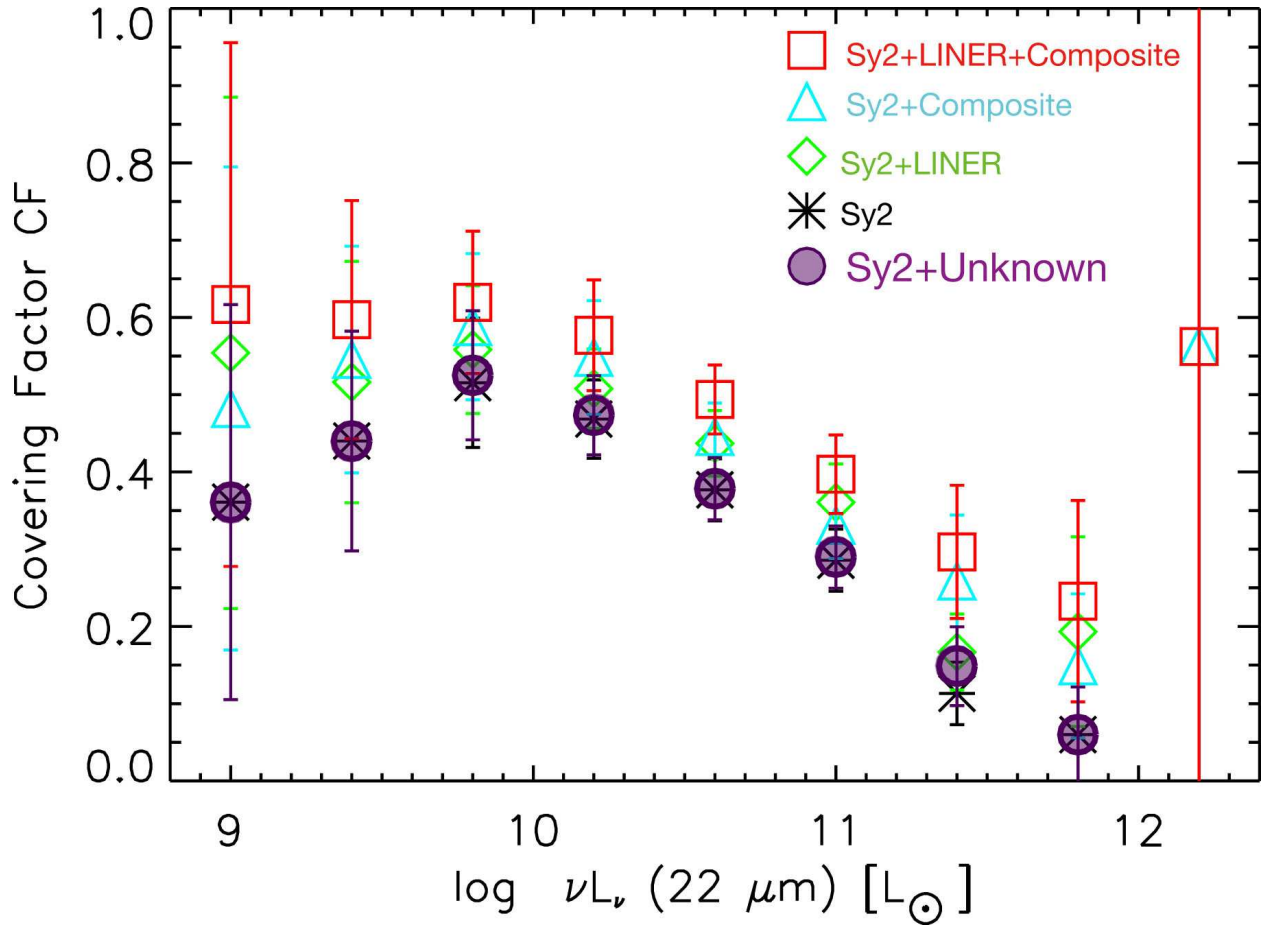


Fig. 22.— The CF as a function of the 22- μ m luminosities including the case for which all Unknown galaxies are type 2 AGNs (purple circles) at $z \leq 0.2$.

neglected.

4.3.2. Influence of rejected objects

When we cross-matched the *WISE* sample with the SDSS sample, we rejected 601,460 *WISE* sources that did not lie within the 3-arcsec search radius. If these rejected objects were galaxies, then this could have an effect on our results. We thus attempted to extract possible galaxy candidates according to the SDSS photometric information and data in the literature.

Figure 23 shows a flow chart of the process used for the extraction. The 601,460 *WISE*-rejected sources were first cross-matched with the SDSS DR8 photometric catalog, which contains 469,053,874 unique primary sources with all data cataloged in the `PhotoPrimary` table on the CAS. We again adopted a 3-arcsec search radius and selected 545,711 sources. Of these, we extracted sources that met the SDSS spectroscopic sample selection criteria, i.e., a `petroMag_r` value of less than 17.77 mag or a `psfMag_i` value of less than 19.1 mag, and considered their morphologies (see Section 2.1.2). The morphological information is listed under the column headed “type” in the `PhotoPrimary` table; point-like objects are labeled as “STAR” (possibly including quasars) and diffuse objects are labeled as “GALAXY”, based on the difference between the PSF and model magnitudes. It should be noted that there is no “QSO” category because it is difficult to distinguish stars and quasars based on the photometry only, unlike the case for the spectroscopy-based `SpecPhoto` table. Thus, an extraction of objects with (i) `petroMag_r` below 17.77 mag and `type` = “GALAXY” and (ii) `psfMag_i` below 19.1 mag and `type` = “STAR” yielded 46,497 sources (17,906 point-like sources and 28,591 diffuse sources). There were 55,749 sources that did not have any SDSS photometric information, and these were rejected. While some of these objects may be galaxies, the sources are optically too faint to be detected by SDSS imaging (the exposure time per band is ~ 60 s, and the detection limit (95% completeness) of the r-band for point sources is 22.2 mag). We also note that 499,214 faint sources were excluded both by this method and in the spectroscopic target selection (Eisenstein et al. 2001; Strauss et al. 2002). We discuss the influence of these optically faint *WISE* sources on our result in the end of this subsection.

For the 17,906 point-like sources (hereinafter, STAR/QSO sample), we examined their color properties to remove the star objects based on the $g - z$ versus $z - [3.4]$ color-color diagram. Wu et al. (2012) have also plotted this data for spectroscopically confirmed stars and quasars obtained from the SDSS DR7 and *WISE* catalogs and reported that most stars

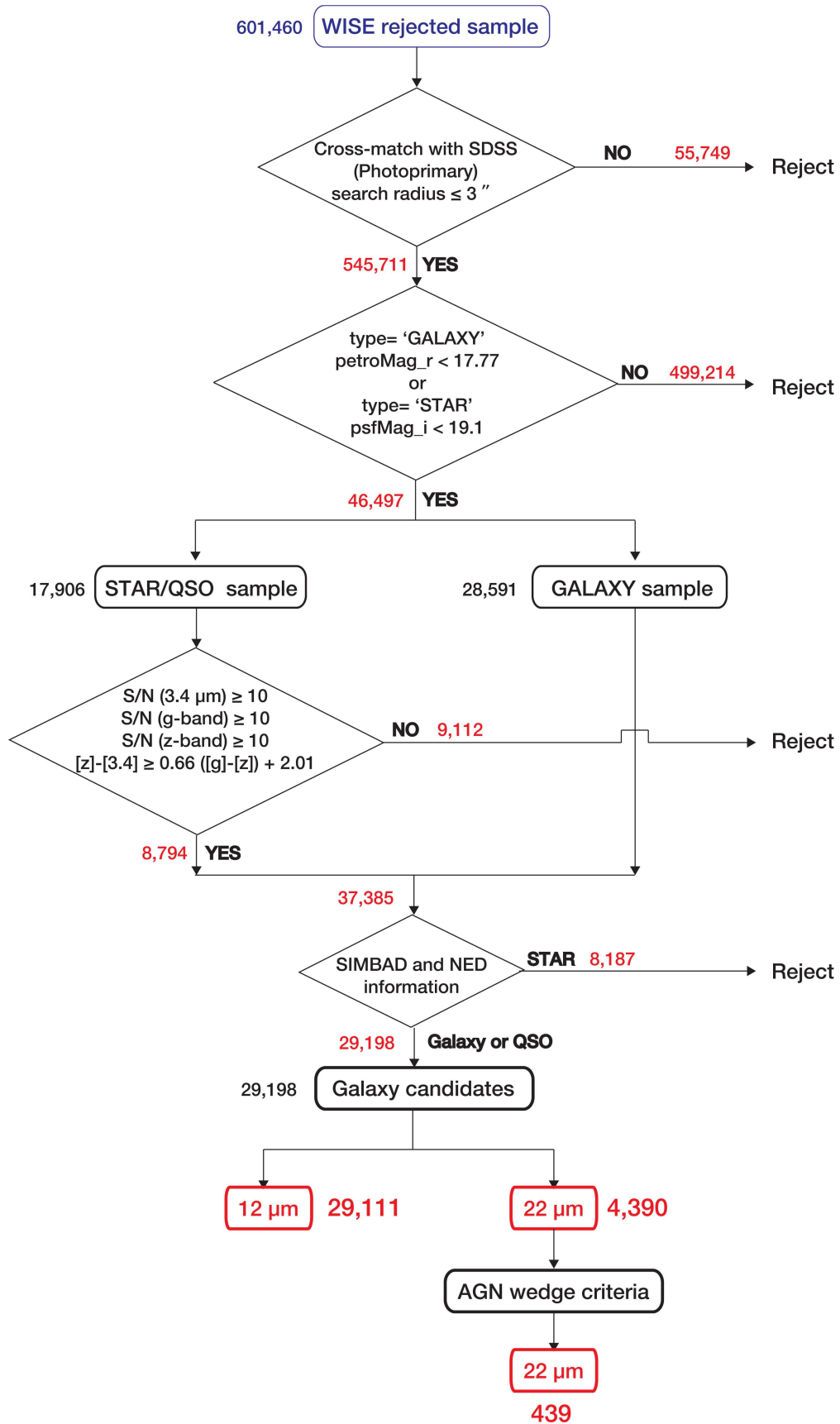


Fig. 23.— Flow chart for extracting the galaxy candidates from the *WISE*-rejected sample.

can be distinguished from quasars using following criterion:

$$z - [3.4] \leq 0.66 \times (g - z) + 2.01. \quad (19)$$

Some high- z ($z > 4$) quasars are actually lost in a field of stars when this criterion is adopted, as Wu et al. (2012) have mentioned. However, as we are focusing on only low- z quasars ($z \leq 0.3$), this criterion is useful. The distribution of the STAR/QSO sample in the color-color diagram is shown in Figure 24. To ensure the reliability of the color value, we examined the color for objects with a S/N of greater than 10 in the g , z , and $3.4\text{-}\mu\text{m}$ band photometry. For comparison, spectroscopically confirmed *WISE*-SDSS stars are also plotted in Figure 24. The criterion proposed by Wu et al. (2012) works well, and by adopting this criterion, 8,794 objects were selected as galaxy candidates.

Finally, we carefully removed stars from the $28,591 + 8,794 = 37,385$ galaxy candidates by utilizing the NASA/IPAC Extragalactic Database (NED⁴) and the Set of Identifications, Measurements, and Bibliography for Astronomical Data (SIMBAD⁵) database. The final galaxy-candidate sample consisted of 29,198 objects: 29,111 in the $12\text{-}\mu\text{m}$ sample and 4,390 in the $22\text{-}\mu\text{m}$ sample. As the *WISE*-SDSS sample contained 223,982 objects in the $12\text{-}\mu\text{m}$ sample and 25,721 objects in the $22\text{-}\mu\text{m}$ sample, the maximum uncertainty, therefore, caused by including these new galaxies would be $29,111/223,982 \sim 0.130$ (13.0%) for the $12\text{-}\mu\text{m}$ sample and $4,390/25,721 \sim 0.170$ (17.0%) for the $22\text{-}\mu\text{m}$ sample. Half of the galaxies in the *WISE*-SDSS sample were classified as SF in Section 2.2 (see Table 2), and we would expect half of the galaxy candidates to be SF, even if they are all galaxies. Hence, the influence on the estimated CF is expected to be small. In the context of considering the AGN wedge, there are 2,922 objects in the AGN wedge as shown in Table 5, which are summarized by the type classification in the case of considering AGN-dominated $22\text{-}\mu\text{m}$ sources. Among them, 439 objects could be galaxies as a consequence of adopting the AGN wedge technique for 2,922 objects. Thus the maximum uncertainty caused by including these galaxies would be $439/2,922 \sim 0.150$ (15.0%).

However, it must be noted that the above estimation is for optically bright (PetroMag_r < 17.77 for galaxies and psfMag_i for type 1 AGNs) MIR sources. Thus, some optically faint sources could be overlooked by our selection procedure. We thus attempted to estimate the influence of the optically faint type 2 AGNs on our results by using deeper spectroscopic data. The Galaxy And Mass Assembly (GAMA; Driver et al. 2009, 2011) program is a spectroscopic survey of $\sim 300,000$ galaxies down to $r < 19.8$ mag over ~ 290 deg² using the

⁴<http://ned.ipac.caltech.edu/>

⁵<http://simbad.u-strasbg.fr/simbad/>

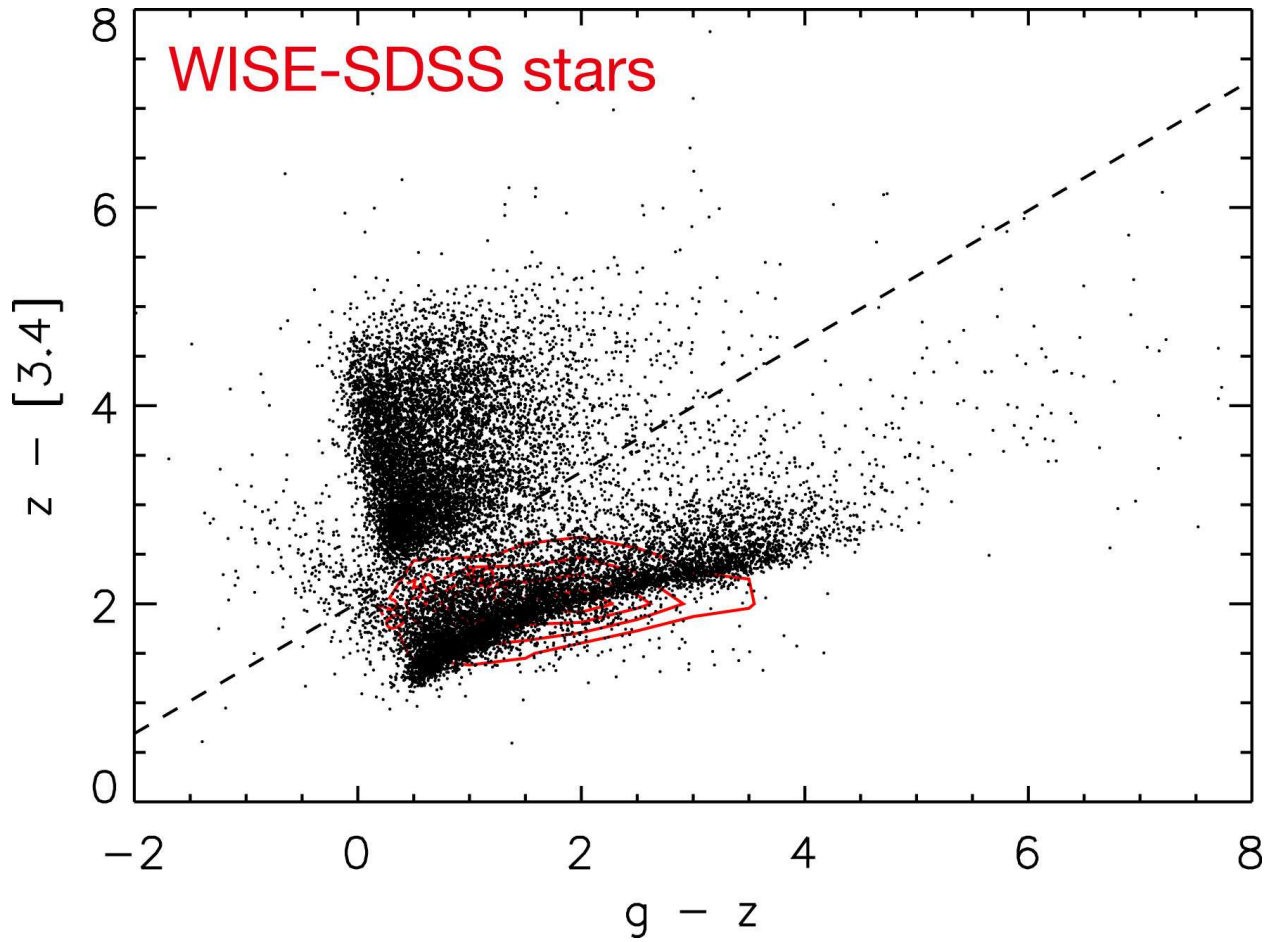


Fig. 24.— Distribution of the STAR/QSO sample in the $g - z$ versus $z - [3.4]$ color-color diagram. The red contours represent spectroscopically confirmed *WISE*-SDSS stars. The dashed line indicates the star-quasar separation criterion, $z - [3.4] = 0.66(g - z) + 2.01$, proposed by Wu et al. (2012).

AAOmega multi-object spectrograph on the Anglo-Australian Telescope (AAT). Partial data obtained in the first phase of the GAMA survey has been released as Data Release 2 (DR2; Liske et al. in preparation), and this catalog provides AAT/AAOmega spectra, redshifts, and a wealth of ancillary information for 72,225 objects located in three equatorial fields (referred to as G09, G12, and G15) covering 144 deg². The limiting Petrosian r magnitudes are 19.0 (G09 and G12) and 19.4 (G15), two magnitudes deeper than that of the SDSS spectroscopic catalog, but the survey area is smaller than that of the SDSS. Therefore, GAMA could be the best dataset for extracting optically faint WISE sources that were not detected by the SDSS spectroscopy. In what follows, we extract the optically faint sources and estimate the fraction of type 2 AGNs among the *WISE*-rejected sample by assuming that the spatial distributions of the optically faint sources in the GAMA field are the same as those in the SDSS spectroscopic field.

We first narrowed the *WISE*-rejected sample to sources within the G09, G12, and G15 regions, which yielded 8,023 sources (8,013 in the 12- μ m sample and 388 in the 22- μ m sample). These sources were then cross-identified with the GAMA DR2 by using a matching radius of 3 arcsec. In this study, we used the `EmLinesPhys` table, which includes the coordinates of each GAMA source and its redshift. As a result, 4,733 sources (hereinafter WISE-nonSDSS-GAMA objects) were selected (4,732 sources in the 12- μ m sample and 217 sources in the 22- μ m sample). We then extracted type 2 AGNs, based on the BPT diagram employed in Section 2.2, with the line information obtained from the `SpecLines` table (Hopkins et al. 2013). In addition, we narrowed the sample down to sources with a redshift smaller than 0.2, which were adopted to evaluate the luminosity and redshift dependence of the CF. This resulted in 163 objects being classified as type 2 AGNs at $z \leq 0.2$ (163 sources in the 12- μ m sample and 15 sources in the 22- μ m sample). In the case of the 22- μ m sample, 15/217 $\sim 7\%$ objects were type 2 AGNs. We note that this estimation is a lower limit because the GAMA could not detect almost 40% of the *WISE*-rejected sample (hereinafter WISE-nonSDSS-nonGAMA objects), and thus some optically faint sources with a `PetroMag_r` greater than 19.0 could be type 2 AGNs. We therefore investigated the possibility that these objects exist by using NED and SIMBAD. Among the 3,290 WISE-nonSDSS-nonGAMA objects, 2,492 and 424 objects were cross-identified with the NED and SIMBAD, respectively, by using matching radii of 3 arcsec, and we checked the existence of type 2 AGNs at $0.006 < z < 0.2$. We found that there were no objects that satisfied the above criteria, although NED and SIMBAD did not have complete spectroscopic classifications for all the galaxies. Therefore, the majority of the WISE-nonSDSS-nonGAMA objects are expected to be high- z (> 0.2) sources, and the maximum contribution ($\sim 7\%$) of type 2 AGN for the 22- μ m sample mentioned above should be a reasonable estimate. In terms of the CF (type 2 AGN fraction), this result indicates that the CF we derived in Section 4.2 is an

underestimation (see also Sections 4.4 and 4.5).

4.3.3. Influence of optically elusive buried AGNs

The type classification was based on the optical spectroscopic information (see Section 2.2), but if the central engine of an AGN is enshrouded by dust covering the entire solid angle, then the bulk of the optical emission will be absorbed by the dust, and it is thus difficult to classify objects using the BPT diagram. The presence of these “buried” AGNs has been reported by many authors including Oyabu et al. (2011), who identified two buried AGNs based on *AKARI* near-IR (NIR) spectroscopic observations. These objects do not show any AGN features in the optical spectra but do have a steep red continuum from the hot dust in the NIR spectra.

We examined the presence of buried AGNs based on their expected *WISE* color, which should be very red. Figure 25 shows the color–color diagram ($[3.4] - [4.6]$ versus $[4.6] - [12]$) for *WISE*–SDSS sample. The shaded regions representing different galaxy types indicate areas where the photometry of redshifted sample galaxies was synthesized using simulated SEDs (Wright et al. 2010). A few LINERs, SFs, and Composites are located in the obscured AGN region, defined by Wright et al. (2010), but the number of these obscured AGNs is very small. In the context of considering the AGN wedge, 1.2% of the SFs and 0.4% of the Unknown galaxies that exist in the AGN wedge may be candidates for buried AGNs (see Table 5). Their percentage of all AGN-dominated objects is very small (1.6% at most), and thus we conclude that their influence on the CF will also be small.

Table 5. Classifications of the objects in the AGN wedge for 22- μ m sample.

type	number (percentage)
type 1 AGNs	2,077 (71.1%)
type 2 AGNs	520 (17.8%)
LINER	130 (4.4%)
Composite	150 (5.1%)
SF	34 (1.2 %)
Unknown	11 (0.4 %)
All	2,922 (100 %)

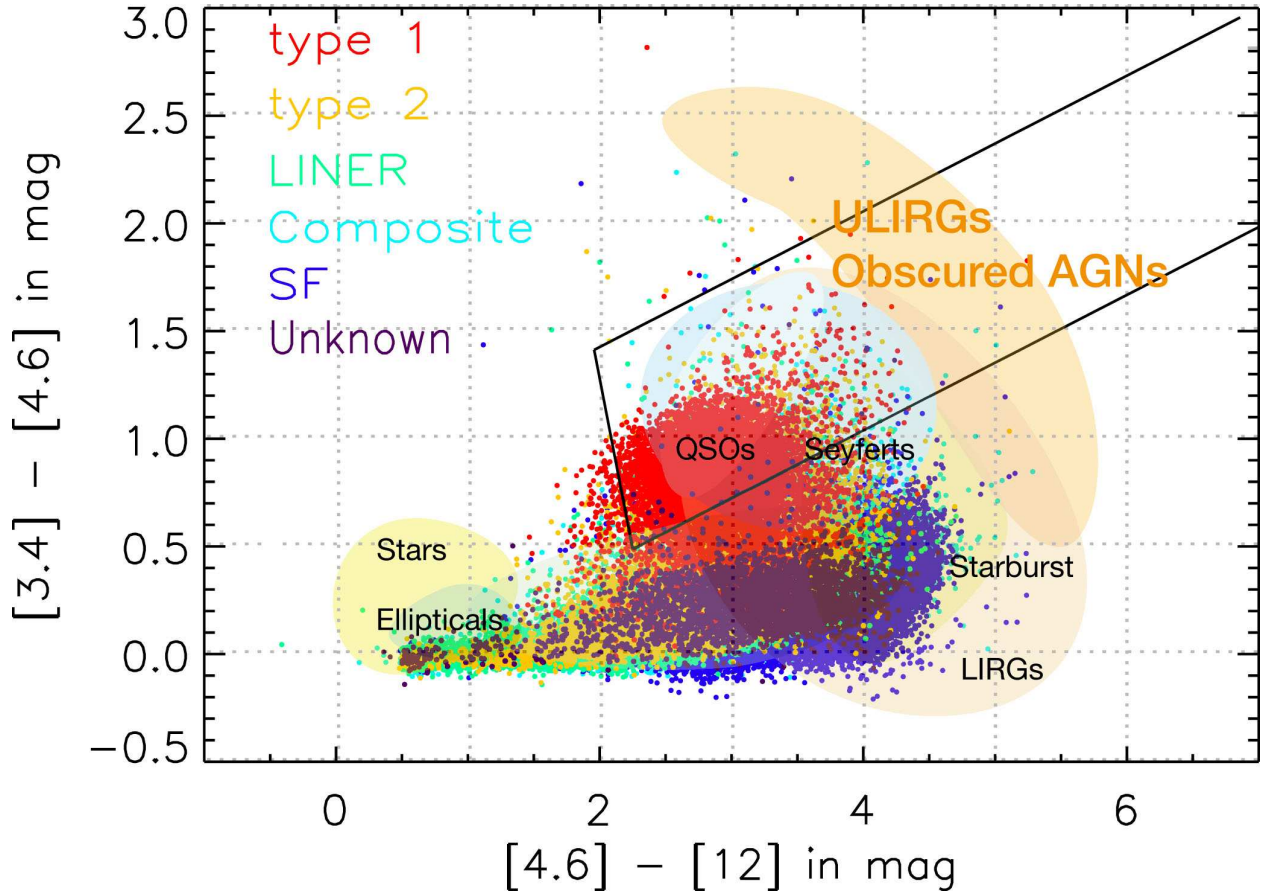


Fig. 25.— *WISE* color-color diagram of the *WISE*-SDSS galaxies. The shaded regions representing different galaxy types indicate areas where the photometry of redshifted sample galaxies was synthesized using simulated SEDs (Wright et al. 2010). The solid lines illustrate the AGN selection wedge defined from Mateos et al. (2012).

4.4. Interpretation of Luminosity Dependence of the Covering Factor

We consider here two dust torus models that may explain the luminosity dependence of the CF. We fit our results first to the receding torus model (Lawrence 1991), which argues that an expansion of the dust sublimation radius with luminosity will push the torus to larger radii and will therefore decrease its CF. In this model, the CF is described as a function of luminosity by (e.g., Simpson 1998, 2005)

$$CF = \left(1 + \frac{3L}{L_0}\right)^{-0.5}, \quad (20)$$

where L_0 is the luminosity at which the CF is equal to 0.5. Here, the luminosity is based on radiation not from the dust torus but from the total output of the central engine of the AGNs. Thus, the luminosity of concern here is not equivalent to the MIR luminosity. However, the radiation from the central engine is thought to be strongly correlated with that from the dust torus. For instance, Spinoglio et al. (1995) found that the bolometric luminosity of AGNs is proportional to the MIR luminosity, based on an examination of *IRAS* data. Ichikawa et al. (2012) obtained MIR photometric data for a total of 128 sources in the 9-, 12-, 18-, 22-, and 25- μm bands from *AKARI* and *WISE* as well as hard X-ray (14–195 keV) data from *Swift* BAT. They found a good correlation between the hard X-ray and MIR luminosities over three orders of magnitude ($9 < \log \nu L_\nu(9, 18 \mu\text{m}) < 12$), which is tighter than that between the hard-X-ray luminosity and far-IR (FIR) luminosities at 90 μm . This could indicate that the radiation from the central engine is directly connected to that from the dust torus. Therefore, the MIR luminosity should be a good tracer of the bolometric luminosity from the central engine.

It should be noted that we restrict the sample here to those objects at $z \leq 0.15$ to omit as much as possible the effects of optically faint WISE sources (see Section 4.3.2). The relationship between the CF and MIR luminosity, derived in Section 4.2, is compared in Figure 26 with that expected from the receding torus model. Here, L_0 is a free-parameter; its best-fit value and reduced chi-square value (χ^2/ν) are listed in Table 6. Figure 26 demonstrates that the receding torus model provides a good model for our data.

However, the receding torus model does not provide a unique explanation of the luminosity dependence; the assumption that the height of the torus is constant regardless of the luminosity is rather strict, and the value of the reduced chi-square for the CF fit is relatively large. We therefore also considered the modified receding torus model, which was proposed by Simpson (2005) and supported by Ricci et al. (2013) and Lusso et al. (2013). In this

model, the height of the torus (h) also depends on the luminosity of the AGNs,

$$CF = \left[1 + 3 \left(\frac{L}{L_0} \right)^{1-2\xi} \right]^{-0.5}, \quad (21)$$

where there are now two free-parameters: L_0 and ξ . The best-fit values and χ^2/ν for this model are also listed in Table 6, and the results are also shown in Figure 26. We found that the modified receding torus model appears to provide a better fit to the data. For this model, ξ takes positive values (~ 0.1 – 0.3 ; cf., Table 6.), which are consistent with those reported by Simpson (2005).

The luminosity dependence of the height of the torus ($h \propto L^{0.2-0.3}$) can be interpreted in the framework of the radiation-limited clumpy torus model. This model was originally suggested by Hönig & Beckert (2007), who investigated the influence of the dust distribution on the Eddington limit of the torus and concluded that the torus was a clumpy torus comprised of self-gravitating, optically thick dust clouds. Clouds at small radii from the central black hole are directly exposed to the AGN radiation pressure and forced out to larger distances, while distant clouds are shielded from the AGN radiation by the clouds at small radii. Both effects determine the size of the torus. This model gives the luminosity dependence of the height as $h \propto L^{0.25}$, which is in good agreement with our measurements.

4.5. Comparison to Optical and Hard X-ray Results

Finally, we compare our measurement of the CF based on the MIR data with that based on optical and hard X-ray data. Any comparison to results obtained from a different data set should be undertaken carefully because the luminosity and redshift ranges may be different. In particular, as there is no consensus on the redshift dependence of the CF at $z > 0.2$, if the CF depends strongly on redshift as reported by previous studies (e.g., La Franca et al.

Table 6. Fitting parameters of the receding torus model and modified receding torus model for the 22- μm sample in the AGN wedge.

	Receding Tours Mode			Modified Receding Torus Mode			
	L_0	χ^2/ν	χ^2_ν	L_0	ξ	χ^2/ν	χ^2_ν
Sy2s	$(8.33 \pm 1.41) \times 10^9$	16.34/6	2.72	$(4.20 \pm 2.08) \times 10^9$	(0.25 ± 0.07)	5.26/5	1.05
Sy2s + LINERs	$(1.19 \pm 0.20) \times 10^{10}$	15.40/7	2.20	$(8.44 \pm 3.17) \times 10^9$	(0.26 ± 0.07)	4.55/6	0.76
Sy2s + Composites	$(1.47 \pm 0.27) \times 10^{10}$	12.74/6	2.12	$(9.51 \pm 0.45) \times 10^9$	(0.29 ± 0.07)	1.72/5	0.34
Sy2s + LINERs + Composites	$(1.96 \pm 0.36) \times 10^{10}$	13.52/7	1.93	$(1.87 \pm 0.83) \times 10^{10}$	(0.32 ± 0.07)	1.09/6	0.18

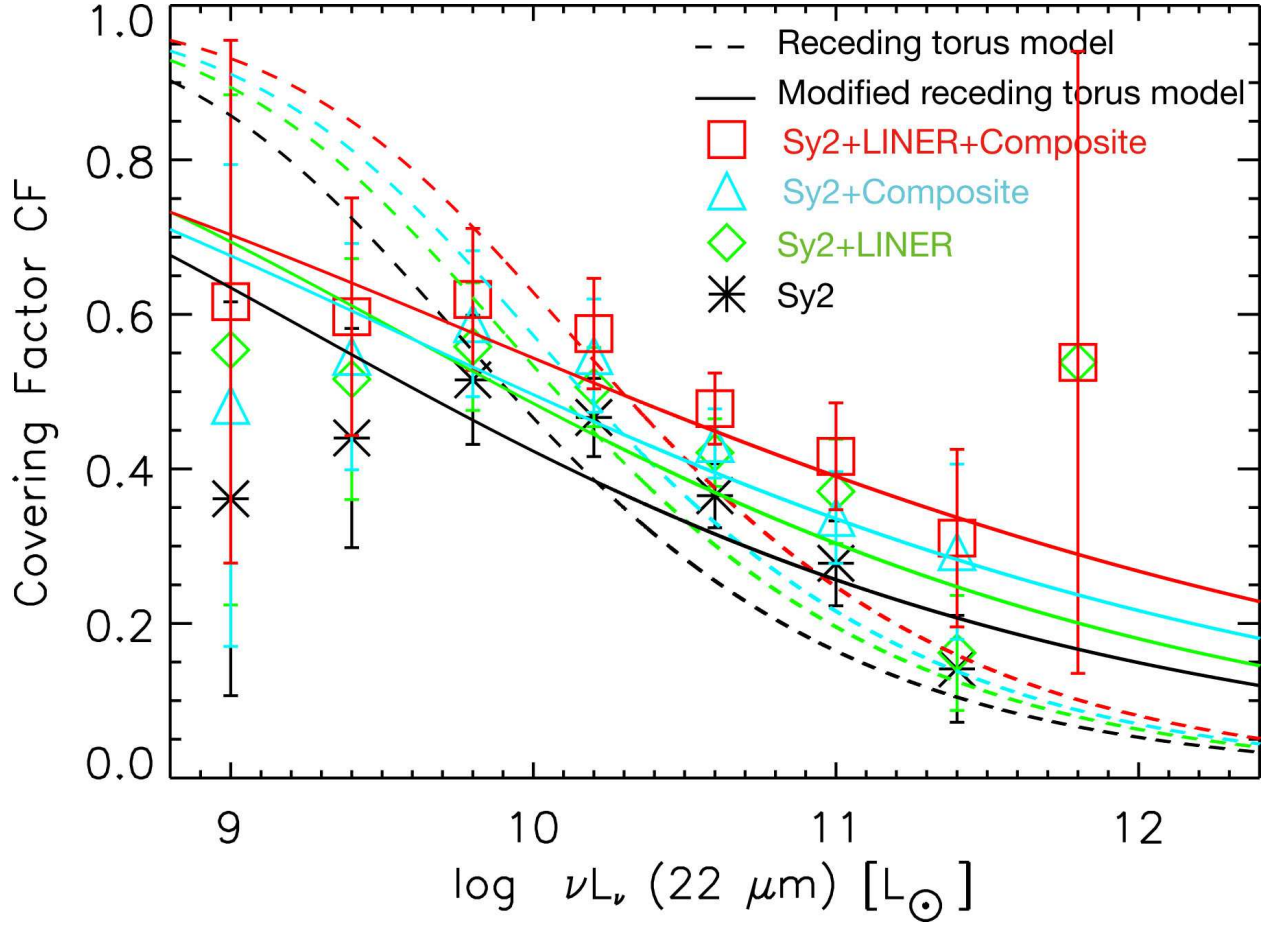


Fig. 26.— The CF as a function of the 22- μm luminosity for AGN-dominated MIR sources at $z \leq 0.15$. The dashed line shows the best-fit curve determined with the receding torus model. The solid line shows the best-fit curve determined with the modified receding torus model.

2005; Hasinger 2008), then this would affect any comparisons. Hence, we compared our results with those obtained from Simpson (2005) and Hasinger (2008), who presented the relationship between the CF and the [OIII] luminosity at $z < 0.3$ (Simpson 2005) and the hard X-ray (2–10 keV) luminosity (Hasinger 2008) at $z < 0.2^6$. It should be noted that here we also restrict the sample to those objects at $z \leq 0.15$ to omit as much as possible the effects of optically faint WISE sources (see Section 4.3.2).

We also compared the results with those obtained from higher energy X-ray band data, because the 2–10-keV-band-based surveys could fail to detect heavily obscured luminous AGN, as has been reported by, e.g., Mateos et al. (2012). We referred to two papers: Beckmann et al. (2009), who analyzed data for 199 AGNs supposedly detected by *INTEGRAL* above 20 keV and reported a negative correlation between the fraction of absorbed/type 2 AGNs and the hard X-ray (20–100 keV) luminosity; and Burlon et al. (2011), who also reported the same correlation on the basis of 15–55-keV data. The sample data in both papers have been examined, and thus we estimated the CF using the data at $z \leq 0.15$. We assume here that the dependence of the CF on redshift is very weak or almost constant even at $z \leq 0.3$, which enables us to compare directly the luminosity dependence without considering the effect of the redshift dependence.

For the comparison, we converted the [OIII] luminosity ($L_{[\text{OIII}]}$) and hard X-ray luminosity (L_X) to the 22- μm luminosity (L_{MIR}) using the following conversion formulae:

$$\log \left(\frac{L_{\text{MIR}}}{10^{43}} \right) = (2.36 \pm 0.01) + (0.76 \pm 0.01) \log \left(\frac{L_{[\text{OIII}]}}{10^{43}} \right), \quad (22)$$

$$\log \left(\frac{L_{\text{MIR}}}{10^{43}} \right) = (0.19 \pm 0.05) + (1.11 \pm 0.07) \log \left(\frac{L_X}{10^{43}} \right), \quad (23)$$

$$\log \left(\frac{L_{\text{MIR}}}{10^{43}} \right) = (0.27 \pm 0.05) + (0.89 \pm 0.04) \log \left(\frac{L_{X(14-195 \text{ keV})}}{10^{43}} \right), \quad (24)$$

where the luminosities are normalized to $10^{43} \text{ erg s}^{-1}$. For the [OIII] luminosity, we calculated the conversion factors by plotting $\log L_{[\text{OIII}]}$ versus $\log[\nu L_\nu(22 \mu\text{m})]$, as shown in Figure 27. To ensure the accuracy of the conversion, high-SN (>10) objects (type 1AGNs, type 2 AGNs, LINERs, and Composites) are plotted. For the hard X-ray luminosity, we used Equation (5) in Gandhi et al. (2009) and Equation (2) when considering the entire sample at 18 μm in Matsuta et al. (2012). As Gandhi et al. (2009) derived the relationship between the 12.3- μm and hard X-ray luminosity, the intrinsic error associated with the conversion in this case will be somewhat different to that of Equation (23). Similarly, Matsuta et al. (2012) derived the

⁶Hasinger (2008) also treats the high redshift data ($z < 5.2$), but we only use the data in the $0.015 < z < 0.2$ redshift bin for the comparison. See Figure 8 in Hasinger (2008).

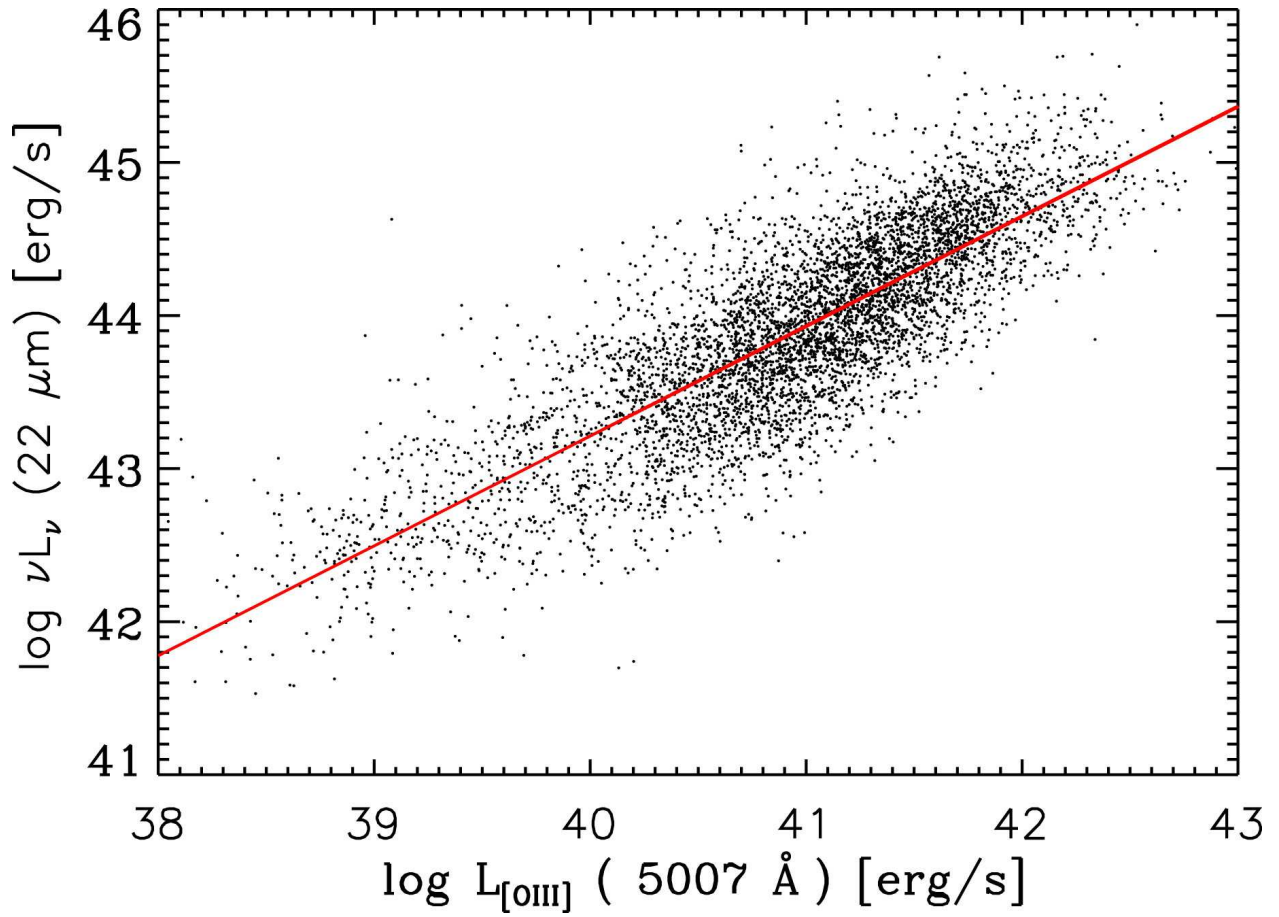


Fig. 27.— Plot of $\log L_{[\text{OIII}]}$ versus $\nu L_{\nu}(22 \text{ \mu m})$. The solid red line shows the best-fit linear function.

relationship between the 18- μm and hard X-ray (14–195 keV) luminosity from *AKARI* and *Swift*-BAT, respectively, and thus some uncertainty may arise from the conversion.

Figure 28 compares our measurements with those of the optical (Simpson 2005), hard X-ray (Hasinger 2008), 15–55-keV (Burlon et al. 2011), and 20–100-keV (Beckmann et al. 2009) studies. Uncertainties (1σ level) in the CFs obtained from Beckmann et al. (2009) and Burlon et al. (2011) were estimated by binomial statistics (see Gehrels 1986) in the same manner as Burlon et al. (2011). The optically-based CF has a larger value than ours over a wide range of luminosities, but the shape of the decrease is similar. To examine the reasons for the differences, the CFs obtained from objects including Sy2 + LINER + Composite galaxies, which are the total sample including the AGN outside the wedge, are also plotted (data are available in Table 11). In that case, the optical data are in good agreement with ours, which indicates that the optical ([OIII])-based selection could be affected by host galaxy contributions. Indeed, Caccianiga et al. (2007), who investigated the nature of all sources (35 in total) in the *XMM-Newton* bright serendipitous survey, showed an optical spectrum dominated by the light from the host galaxy with no evidence (or little evidence) for the presence of an AGN. In contrast, the hard X-ray based CF are consistent with ours, although our MIR-emission-based data exceed the 2–10 keV data by a substantial amount, which indicates that 2–10 keV based surveys fail to detect heavily obscured/absorbed luminous AGN as expected above. Ultimately, our MIR selection with the AGN wedge may avoid the problems associated with optical selection, as well as hard X-ray (>2 keV) based studies. We note that the CF derived from the 22- μm sample in the AGN wedge would be an underestimate due to the lack of optically faint (PetroMag_r > 17.7) MIR sources as described in Section 4.3.2. Thus, there may be a small difference between our MIR results and the optical results, although it may be difficult to fill in the gap using only optically faint type 2 AGNs.

5. SUMMARY

Using the *WISE* MIR all-sky survey, we constructed 12- and 22- μm LFs for all types of local galaxies. Using complete optical spectroscopy of emission lines, we classified the galaxies based on the cataloged classifications in the SDSS and their emission line ratios ([NII]/H α and [OIII]/H β). We classified the *WISE* sources into type 1 AGNs, type 2 AGNs, LINERs, Composites, and SFs. We then calculated the number densities of the type 1 and type 2 AGNs by integrating each LF and estimated the CF of the dust torus (the fraction of type 2 AGNs among all AGNs). In particular, we examined the luminosity and redshift dependence of the CF for $\sim 3,000$ AGN-dominated MIR sources which were extracted by

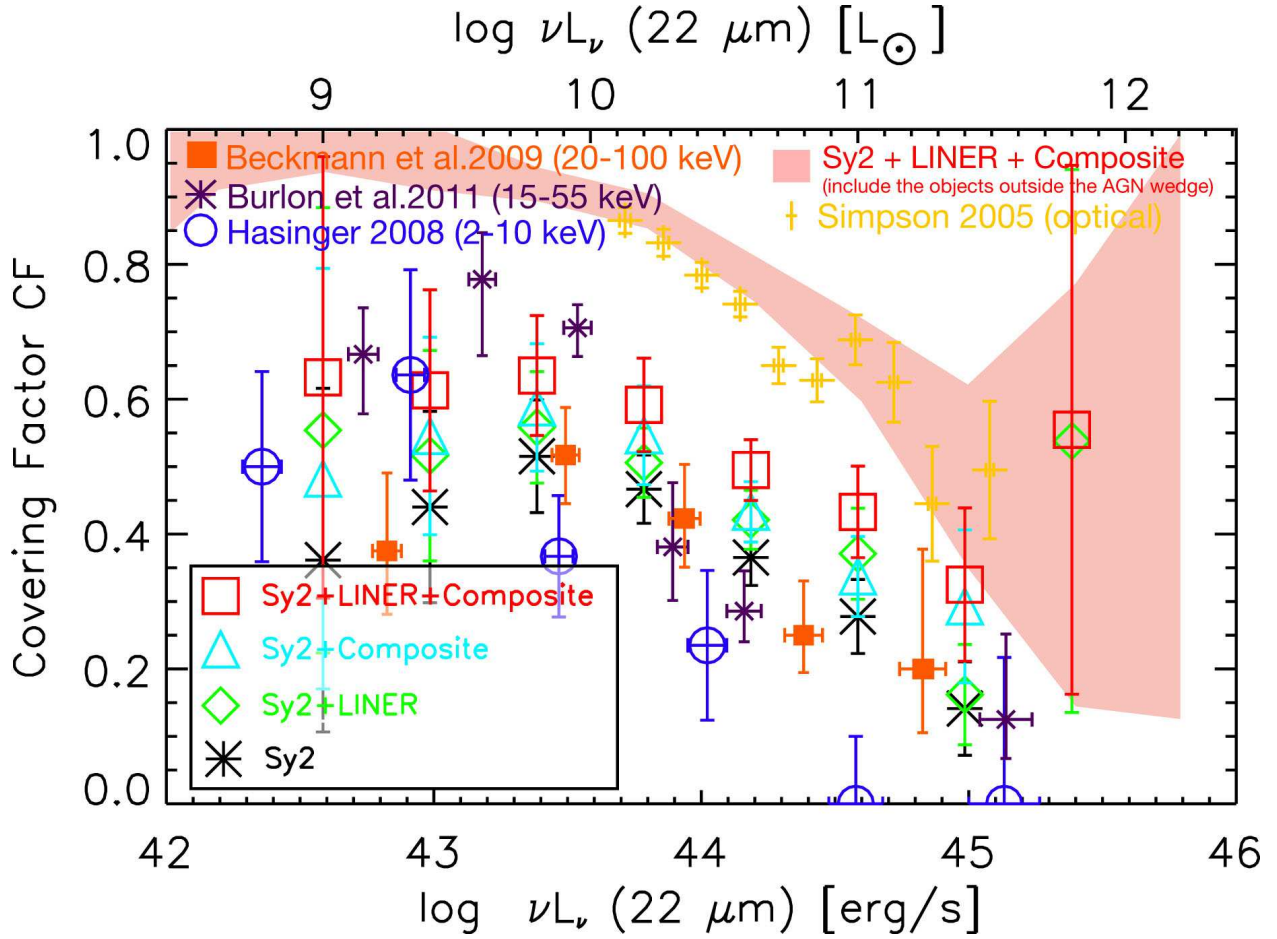


Fig. 28.— Comparison of our measured CF ($z \leq 0.15$) with those of optical (yellow plus: Simpson 2005), hard X-ray (blue circle: Hasinger 2008), 15–55-keV (purple asterisk: Burlon et al. 2011), and 20–100-keV (orange filled square: Beckmann et al. 2009) studies. Errors in the CFs estimated from Beckmann et al. (2009) and Burlon et al. (2011) were determined using binomial statistics (see Gehrels 1986), drawn at the 1σ level. The CFs including Sy2 + LINER + Composite galaxies, which are the total sample including the outside the AGN wedge, are also plotted (red shaded region; see Appendix C). The conversion uncertainty, represented in Figure, is shown as the horizontal error bars for the optical and hard X-ray measurements.

examining their MIR colors. The main results are as follows:

1. Less luminous AGNs in the MIR region are affected by a contribution from their host SF.
2. The CF decreases with increasing 22- μm luminosity regardless of the choice of type 2 AGN classification criteria, although this dependence is relatively weaker than previous studies.
3. The CF does not change significantly with the redshift ($z < 0.2$).
4. The luminosity dependence of the CF can be interpreted using the receding torus model. This luminosity dependence is better described by the modified receding torus model in which the height of the torus is parameterized.
5. Measurements of the CF based on optical survey data exceed our data but are in good agreement if contributions of the host galaxy (i.e., without adopting the AGN wedge selection) are not considered. In contrast, measurements of the CF based on hard X-ray survey data are almost consistent with ours. These trends may indicate that optical survey data is affected by the host galaxy contribution.

Our study has confirmed and extended previous results obtained with *IRAS*, *Spitzer*, and *AKARI* by constructing a much larger MIR-selected sample with *WISE*. The large number of galaxies in the sample we obtained here means that the variation in the CF with the luminosity and redshift is described with a higher statistical accuracy and lower systematic errors than previous results. We emphasize that a luminosity-dependent torus geometry destroys the simplicity of the original torus unification scheme and now requires that at least one new free function must be determined. Our results are inconsistent with the simplest unified scheme, which expects that the CF is independent of the luminosity. A modification of this simple zero-order unification scheme is required. The present results with WISE have provided us with an important local benchmark for AGN studies at high redshifts.

The authors gratefully acknowledge the anonymous referee for a careful reading of the manuscript and very helpful comments. We are also deeply thankful to Drs Guenther Hasinger (Institute for Astronomy) and Chris Simpson (Liverpool John Moores University) who kindly provided data for comparison. We also thank Drs Tadayasu Dotani (ISAS/JAXA), Yoshihiro Ueda (Kyoto University), Tohru Nagao (Ehime University), and Akihiro Doi (ISAS/JAXA) for their relevant comments.

This publication makes use of data products from the Wide-field Infrared Survey Explorer, which is a joint project of the University of California, Los Angeles, and the Jet Propulsion Laboratory/California Institute of Technology, funded by the National Aeronautics and Space Administration. Funding for SDSS-III has been provided by the Alfred P. Sloan Foundation, the Participating Institutions, the National Science Foundation, and the U.S. Department of Energy Office of Science. The SDSS-III web site is <http://www.sdss3.org/>. SDSS-III is managed by the Astrophysical Research Consortium for the Participating Institutions of the SDSS-III Collaboration including the University of Arizona, the Brazilian Participation Group, Brookhaven National Laboratory, University of Cambridge, Carnegie Mellon University, University of Florida, the French Participation Group, the German Participation Group, Harvard University, the Instituto de Astrofísica de Canarias, the Michigan State/Notre Dame/JINA Participation Group, Johns Hopkins University, Lawrence Berkeley National Laboratory, Max Planck Institute for Astrophysics, Max Planck Institute for Extraterrestrial Physics, New Mexico State University, New York University, Ohio State University, Pennsylvania State University, University of Portsmouth, Princeton University, the Spanish Participation Group, University of Tokyo, University of Utah, Vanderbilt University, University of Virginia, University of Washington, and Yale University. This research has made use of the SIMBAD database, operated at CDS, Strasbourg, France. Also, this research has made use of the NASA/IPAC Extragalactic Database (NED) which is operated by the Jet Propulsion Laboratory, California Institute of Technology, under contract with the National Aeronautics and Space Administration. GAMA is a joint European-Australasian project based around a spectroscopic campaign using the Anglo-Australian Telescope. The GAMA input catalogue is based on data taken from the Sloan Digital Sky Survey and the UKIRT Infrared Deep Sky Survey. Complementary imaging of the GAMA regions is being obtained by a number of independent survey programs including GALEX MIS, VST KiDS, VISTA VIKING, WISE, Herschel-ATLAS, GMRT and ASKAP providing UV to radio coverage. GAMA is funded by the STFC (UK), the ARC (Australia), the AAO, and the participating institutions. The GAMA website is <http://www.gama-survey.org/>. P.G. acknowledges support from STFC grant reference ST/J00369711.

A. The V/V_{\max} Test

Before constructing the LFs in Section 2.3, we performed the standard V/V_{\max} test (Schmidt 1968) to examine whether the spatial distribution of the sources in a sample is uniform. Here, V is the volume enclosed at the redshift of an object, and V_{\max} is the volume that would be enclosed at the maximum redshift at which the object could be detected.

If the sample is complete, the mean value of V/V_{\max} should be 0.5. However, the redshift evolution (i.e., the increase in the number density and/or luminosity of the sources with their redshift) is expected to increase this value. For example, Rodighiero et al. (2010) reported that the bolometric IR luminosity density evolves as $(1+z)^{3.8\pm 0.4}$ in the redshift interval $0 < z < 1$ based on a combination of data from deep *Spitzer* surveys of the VIMOS VLT Deep Survey (VVDS-SWIRE) and GOODS fields. In fact, the average value of V/V_{\max} for the *WISE*-SDSS sample is 0.51 ± 0.001 for the 12- μm sample and 0.52 ± 0.001 for the 22- μm sample. This means that our sample ($0.006 \leq z \leq 0.3$) could also be expected to be affected by redshift evolution. However, the average values for each redshift bin (we assumed that there is no evolution within a small redshift range) are close to 0.5. Note that the redshift interval in each redshift bin is the same as that in Section 3.1.

Figures 29 and 30 show the average values of V/V_{\max} , $\langle V/V_{\max} \rangle$ for each galaxy type at 12 and 22 μm in different redshift bin. The average values are distributed around 0.5.

B. Luminosity Functions

The LF data for each galaxy type in each redshift bin are summarized in Tables 7, 8, and 9. Note that the data in Table 7 is used in Figure 10, those in Tables 8 and 9 are used in Figure 12, and those in Tables 8 and 9 are used in Figures 13 and 14 (see Section 3.1).

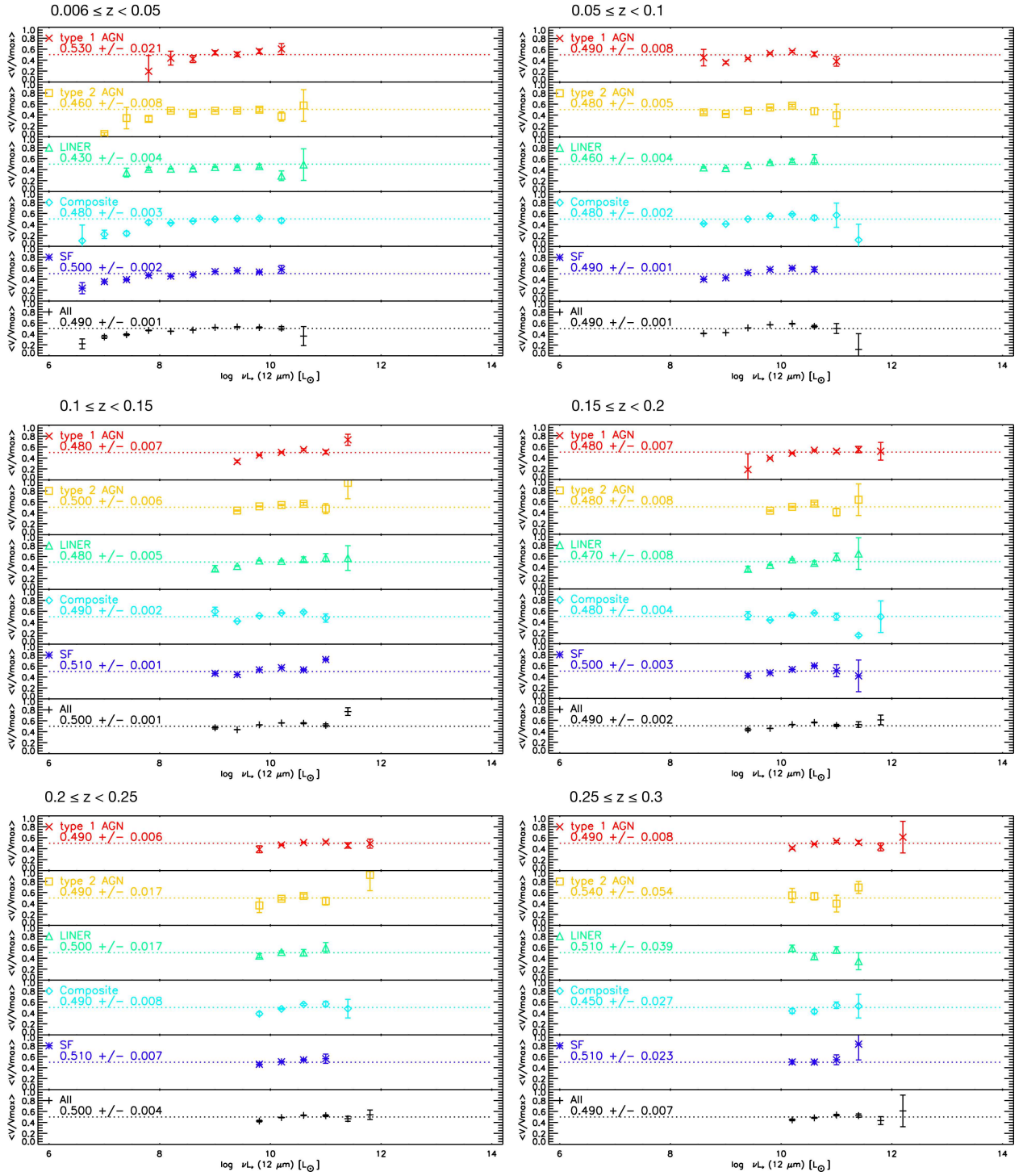


Fig. 29.— Average values of V/V_{\max} for different galaxy types as a function of the 12- μm luminosity in each redshift bin.

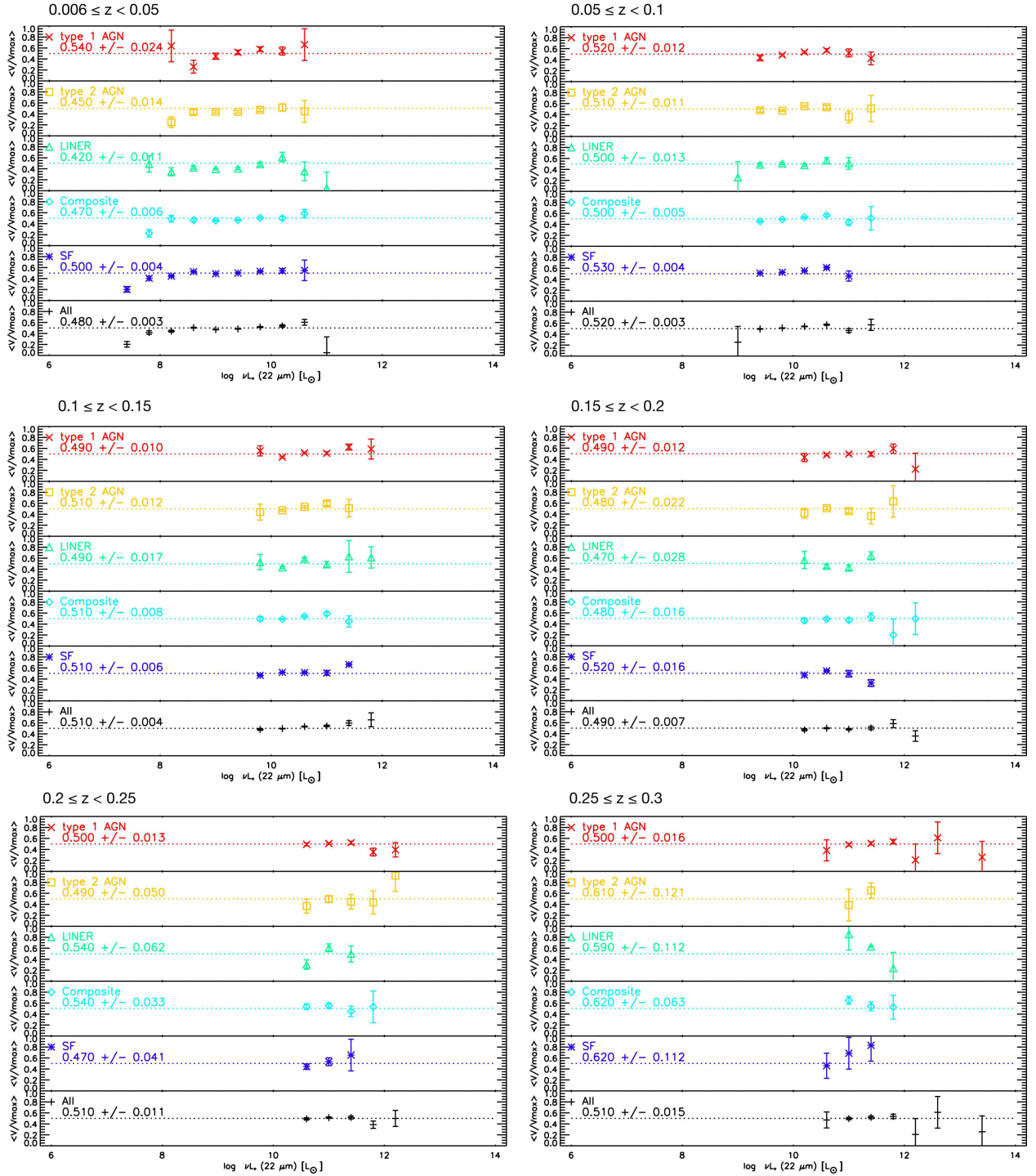


Fig. 30.— Average values of V/V_{\max} for different galaxy types as a function of the 22- μm luminosity in each redshift bin.

Table 7. LFs of all the galaxies at 12 and 22 μm for each redshift bin.

$\log L^{\text{a}}$	12 μm			22 μm		
	ϕ^{b}	σ_{ϕ}^{b}	N	ϕ	σ_{ϕ}	N
$0.006 \leq z < 0.05$						
6.60	1.05×10^{-3}	4.18×10^{-4}	7	0
7.00	3.04×10^{-3}	3.51×10^{-4}	99	0
7.40	1.93×10^{-3}	1.19×10^{-4}	315	2.34×10^{-3}	7.70×10^{-4}	14
7.80	1.77×10^{-3}	5.49×10^{-5}	1255	1.59×10^{-3}	2.13×10^{-4}	72
8.20	2.52×10^{-3}	3.49×10^{-5}	6198	1.23×10^{-3}	8.65×10^{-5}	242
8.60	2.41×10^{-3}	2.11×10^{-5}	13939	1.19×10^{-3}	3.99×10^{-5}	1049
9.00	1.78×10^{-3}	1.78×10^{-5}	10972	1.05×10^{-3}	2.02×10^{-5}	3159
9.40	6.43×10^{-4}	1.02×10^{-5}	4003	4.72×10^{-4}	1.01×10^{-5}	2863
9.80	1.15×10^{-4}	4.30×10^{-6}	717	1.41×10^{-4}	4.78×10^{-6}	877
10.2	1.04×10^{-5}	1.29×10^{-6}	65	2.67×10^{-5}	2.08×10^{-6}	166
10.6	3.26×10^{-7}	2.27×10^{-7}	2	3.40×10^{-6}	7.36×10^{-7}	21
11.0	0	1.61×10^{-7}	1.61×10^{-7}	1
$0.05 \leq z < 0.1$						
8.60	8.52×10^{-4}	2.12×10^{-5}	3935	0
9.00	1.67×10^{-3}	1.37×10^{-5}	32320	2.52×10^{-6}	2.52×10^{-6}	1
9.40	1.22×10^{-3}	6.99×10^{-6}	42700	3.45×10^{-4}	1.30×10^{-5}	1956
9.80	3.31×10^{-4}	3.04×10^{-6}	13093	2.00×10^{-4}	3.20×10^{-6}	5144
10.2	3.79×10^{-5}	9.84×10^{-7}	1542	6.17×10^{-5}	1.52×10^{-6}	2315
10.6	3.43×10^{-6}	2.87×10^{-7}	143	1.19×10^{-5}	5.91×10^{-7}	460
11.0	2.72×10^{-7}	7.96×10^{-8}	11	1.30×10^{-6}	1.85×10^{-7}	52
11.4	3.35×10^{-8}	3.35×10^{-8}	1	2.24×10^{-7}	7.53×10^{-8}	9
$0.1 \leq z < 0.15$						
9.00	3.28×10^{-5}	5.65×10^{-6}	146	0
9.40	5.53×10^{-4}	7.57×10^{-6}	20716	0
9.80	4.60×10^{-4}	4.37×10^{-6}	32978	2.23×10^{-5}	1.92×10^{-6}	294
10.2	8.95×10^{-5}	1.18×10^{-6}	8071	5.45×10^{-5}	1.44×10^{-6}	2785
10.6	8.10×10^{-6}	3.06×10^{-7}	796	1.47×10^{-5}	4.65×10^{-7}	1313
11.0	8.51×10^{-7}	8.95×10^{-8}	91	3.08×10^{-6}	1.99×10^{-7}	295
11.4	9.43×10^{-8}	2.92×10^{-8}	10	4.67×10^{-7}	7.88×10^{-8}	44
11.8	0	4.69×10^{-8}	2.06×10^{-8}	5
$0.15 \leq z < 0.2$						
9.40	1.04×10^{-5}	2.72×10^{-6}	126	0
9.80	1.50×10^{-4}	2.82×10^{-6}	10858	0

Table 7—Continued

log L^a	12 μm			22 μm		
	ϕ^b	σ_ϕ^b	N	ϕ	σ_ϕ	N
10.2	8.12×10^{-5}	1.38×10^{-6}	9591	4.96×10^{-6}	5.84×10^{-7}	175
10.6	1.02×10^{-5}	3.29×10^{-7}	1595	8.45×10^{-6}	4.99×10^{-7}	856
11.0	1.14×10^{-6}	8.45×10^{-8}	208	2.80×10^{-6}	1.86×10^{-7}	431
11.4	1.53×10^{-7}	2.82×10^{-8}	30	4.96×10^{-7}	6.92×10^{-8}	83
11.8	2.31×10^{-8}	1.19×10^{-8}	4	9.80×10^{-8}	2.72×10^{-8}	17
12.2	0	1.32×10^{-8}	9.58×10^{-9}	2
0.2 $\leq z < 0.25$						
9.80	5.25×10^{-6}	4.46×10^{-7}	313	0
10.2	2.50×10^{-5}	6.73×10^{-7}	3363	0
10.6	8.10×10^{-6}	3.04×10^{-7}	1667	1.40×10^{-6}	1.59×10^{-7}	161
11.0	1.14×10^{-6}	8.25×10^{-8}	306	1.56×10^{-6}	1.04×10^{-7}	376
11.4	1.39×10^{-7}	2.17×10^{-8}	42	4.42×10^{-7}	4.67×10^{-8}	120
11.8	2.57×10^{-8}	8.97×10^{-9}	8	5.39×10^{-8}	1.37×10^{-8}	16
12.2	0	1.37×10^{-8}	6.42×10^{-9}	4
0.25 $\leq z \leq 0.3$						
10.2	1.96×10^{-6}	2.28×10^{-7}	284	0
10.6	3.34×10^{-6}	3.54×10^{-7}	940	6.15×10^{-8}	2.87×10^{-8}	5
11.0	1.15×10^{-6}	7.58×10^{-8}	435	8.97×10^{-7}	3.37×10^{-7}	156
11.4	2.12×10^{-7}	2.48×10^{-8}	83	3.76×10^{-7}	4.73×10^{-8}	138
11.8	1.59×10^{-8}	6.01×10^{-9}	7	1.08×10^{-7}	1.82×10^{-8}	41
12.2	2.24×10^{-9}	2.24×10^{-9}	1	2.24×10^{-9}	2.24×10^{-9}	1
12.6	0	2.24×10^{-9}	2.24×10^{-9}	1
13.4	0	2.24×10^{-9}	2.24×10^{-9}	1
0.006 $\leq z \leq 0.3$						
6.60	1.05×10^{-3}	4.18×10^{-4}	7	0
7.00	3.04×10^{-3}	3.51×10^{-4}	99	0
7.40	1.93×10^{-3}	1.19×10^{-4}	315	2.34×10^{-3}	7.70×10^{-4}	14
7.80	1.77×10^{-3}	5.49×10^{-5}	1255	1.59×10^{-3}	2.13×10^{-4}	72
8.20	2.52×10^{-3}	3.49×10^{-5}	6198	1.23×10^{-3}	8.65×10^{-5}	242
8.60	2.13×10^{-3}	1.80×10^{-5}	17874	1.19×10^{-3}	3.99×10^{-5}	1049
9.00	1.71×10^{-3}	1.09×10^{-5}	43438	1.05×10^{-3}	2.02×10^{-5}	3160
9.40	1.06×10^{-3}	5.01×10^{-6}	67543	4.58×10^{-4}	8.66×10^{-6}	4819
9.80	4.24×10^{-4}	2.22×10^{-6}	57959	1.91×10^{-4}	2.69×10^{-6}	6315
10.2	9.04×10^{-5}	7.66×10^{-7}	22916	6.38×10^{-5}	1.07×10^{-6}	5441
10.6	1.08×10^{-5}	2.02×10^{-7}	5143	1.56×10^{-5}	4.03×10^{-7}	2816
11.0	1.34×10^{-6}	5.51×10^{-8}	1051	3.30×10^{-6}	1.38×10^{-7}	1311
11.4	2.04×10^{-7}	3.15×10^{-8}	166	6.21×10^{-7}	5.10×10^{-8}	394

Table 7—Continued

log L^a	12 μm			22 μm		
	ϕ^b	σ_ϕ^b	N	ϕ	σ_ϕ	N
11.8	2.00×10^{-8}	5.27×10^{-9}	19	9.31×10^{-8}	1.22×10^{-8}	79
12.2	8.92×10^{-10}	8.92×10^{-10}	1	9.14×10^{-9}	4.24×10^{-9}	7
12.6	0	8.92×10^{-10}	8.92×10^{-10}	1
13.4	0	8.92×10^{-10}	8.92×10^{-10}	1

Note. — Table 7 is published in its entirety in the electronic edition of the *Astrophysical Journal*. A portion is shown here for guidance regarding its form and content.

^a L_\odot

^b $\text{Mpc}^{-3} \text{Mag}^{-1}$

Table 8. The 12- μ m LFs for each galaxy category at each redshift.

log L^a	type 1			type 2			LINER			Composite			SF			Unknown		
	ϕ^b	σ_ϕ^b	N	ϕ	σ_ϕ	N	ϕ	σ_ϕ	N	ϕ	σ_ϕ	N	ϕ	σ_ϕ	N	ϕ	σ_ϕ	N
$0.006 \leq z < 0.05$																		
6.60	0	0	0	1.14×10^{-4}	1.14×10^{-4}	1	9.40×10^{-4}	4.03×10^{-4}	6	0
7.00	0	6.98×10^{-5}	5.49×10^{-5}	2	0	1.47×10^{-4}	6.74×10^{-5}	5	2.82×10^{-3}	3.40×10^{-4}	92	0
7.40	0	7.72×10^{-6}	5.37×10^{-6}	2	4.17×10^{-5}	1.69×10^{-5}	8	6.11×10^{-5}	1.97×10^{-5}	12	1.82×10^{-3}	1.16×10^{-4}	293	0
7.80	1.39×10^{-6}	1.39×10^{-6}	1	3.29×10^{-5}	7.14×10^{-6}	26	1.21×10^{-4}	1.39×10^{-5}	88	1.21×10^{-4}	1.34×10^{-5}	94	1.48×10^{-3}	5.07×10^{-5}	1038	1.20×10^{-5}	4.29×10^{-6}	8
8.20	3.46×10^{-6}	1.37×10^{-6}	7	6.79×10^{-5}	5.77×10^{-6}	160	2.50×10^{-4}	1.05×10^{-5}	649	2.76×10^{-4}	1.11×10^{-5}	712	1.90×10^{-3}	3.06×10^{-5}	4613	2.48×10^{-5}	3.59×10^{-6}	57
8.60	1.78×10^{-6}	5.36×10^{-7}	11	5.77×10^{-5}	3.16×10^{-6}	339	2.57×10^{-4}	6.55×10^{-6}	1549	3.61×10^{-4}	7.90×10^{-6}	2151	1.71×10^{-3}	1.80×10^{-5}	9772	1.96×10^{-5}	1.82×10^{-6}	117
9.00	1.07×10^{-5}	1.34×10^{-6}	65	5.09×10^{-5}	2.87×10^{-6}	316	1.76×10^{-4}	5.31×10^{-6}	1092	3.49×10^{-4}	8.90×10^{-6}	2133	1.18×10^{-3}	1.40×10^{-5}	7284	1.33×10^{-5}	1.48×10^{-6}	82
9.40	7.41×10^{-6}	1.09×10^{-6}	46	2.94×10^{-5}	2.17×10^{-6}	183	6.34×10^{-5}	3.19×10^{-6}	395	1.71×10^{-4}	5.25×10^{-6}	1062	3.68×10^{-4}	7.70×10^{-6}	2291	4.25×10^{-6}	8.23×10^{-7}	26
9.80	6.19×10^{-6}	9.94×10^{-7}	38	9.03×10^{-6}	1.20×10^{-6}	56	1.27×10^{-5}	1.43×10^{-6}	79	3.44×10^{-5}	2.36×10^{-6}	214	5.22×10^{-5}	2.89×10^{-6}	325	8.13×10^{-7}	3.59×10^{-7}	5
10.2	1.29×10^{-6}	4.54×10^{-7}	8	1.61×10^{-6}	5.08×10^{-7}	10	9.67×10^{-7}	3.93×10^{-7}	6	4.35×10^{-6}	8.34×10^{-7}	27	2.25×10^{-6}	6.01×10^{-7}	14	0
10.6	0	1.61×10^{-7}	1.61×10^{-7}	1	1.61×10^{-7}	1.61×10^{-7}	1	0	0	0
$0.05 \leq z < 0.1$																		
8.60	5.22×10^{-7}	2.53×10^{-7}	4	2.38×10^{-5}	3.02×10^{-6}	106	9.21×10^{-5}	6.06×10^{-6}	473	1.22×10^{-4}	6.46×10^{-6}	600	6.07×10^{-4}	1.90×10^{-5}	2715	7.18×10^{-6}	1.50×10^{-6}	37
9.00	3.64×10^{-6}	4.47×10^{-7}	86	4.19×10^{-5}	1.94×10^{-6}	869	1.12×10^{-4}	2.37×10^{-6}	2759	2.84×10^{-4}	5.00×10^{-6}	6136	1.21×10^{-3}	1.24×10^{-5}	22108	1.71×10^{-5}	1.11×10^{-6}	362
9.40	9.85×10^{-6}	4.98×10^{-7}	402	3.87×10^{-5}	1.19×10^{-6}	1410	5.55×10^{-5}	1.25×10^{-6}	2179	2.55×10^{-4}	3.15×10^{-6}	9221	8.48×10^{-4}	5.94×10^{-6}	29012	1.29×10^{-5}	6.78×10^{-7}	476
9.80	9.77×10^{-6}	4.83×10^{-7}	409	1.49×10^{-5}	6.41×10^{-7}	590	1.14×10^{-5}	5.43×10^{-7}	457	8.43×10^{-5}	1.64×10^{-6}	3263	2.08×10^{-4}	2.35×10^{-6}	8259	2.95×10^{-6}	2.81×10^{-7}	115
10.2	4.46×10^{-6}	3.28×10^{-7}	186	3.47×10^{-6}	2.96×10^{-7}	140	1.73×10^{-6}	2.04×10^{-7}	72	1.07×10^{-5}	5.31×10^{-7}	431	1.73×10^{-5}	6.66×10^{-7}	706	1.93×10^{-7}	7.66×10^{-8}	7
10.6	9.87×10^{-7}	1.54×10^{-7}	41	4.35×10^{-7}	1.01×10^{-7}	18	2.29×10^{-7}	7.29×10^{-8}	9	8.85×10^{-7}	1.45×10^{-7}	37	8.89×10^{-7}	1.46×10^{-7}	37	2.38×10^{-8}	2.38×10^{-8}	1
11.0	1.29×10^{-7}	5.42×10^{-8}	5	7.41×10^{-8}	4.14×10^{-8}	3	0	8.09×10^{-8}	4.24×10^{-8}	3	0	0
11.4	0	0	0	3.35×10^{-8}	3.35×10^{-8}	1	0	0
$0.1 \leq z < 0.15$																		
9.00	0	0	4.64×10^{-6}	1.09×10^{-6}	27	8.05×10^{-6}	4.87×10^{-6}	12	1.93×10^{-5}	2.54×10^{-6}	105	8.68×10^{-7}	7.30×10^{-7}	2
9.40	1.70×10^{-6}	1.79×10^{-7}	113	1.66×10^{-5}	8.40×10^{-7}	686	2.96×10^{-5}	1.01×10^{-6}	1541	1.21×10^{-4}	3.49×10^{-6}	5162	3.75×10^{-4}	6.56×10^{-6}	12757	9.75×10^{-6}	5.77×10^{-7}	457
9.80	6.57×10^{-6}	2.52×10^{-7}	697	1.66×10^{-5}	6.21×10^{-7}	1291	1.38×10^{-5}	4.76×10^{-7}	1191	1.07×10^{-4}	2.11×10^{-6}	8041	3.09×10^{-4}	3.72×10^{-6}	21268	6.33×10^{-6}	3.59×10^{-7}	490
10.2	5.77×10^{-6}	2.32×10^{-7}	622	5.56×10^{-6}	2.87×10^{-7}	484	3.53×10^{-6}	2.39×10^{-7}	307	2.30×10^{-5}	6.22×10^{-7}	2035	5.08×10^{-5}	8.98×10^{-7}	4546	8.12×10^{-7}	9.99×10^{-8}	77

Table 8—Continued

log L^a	type 1			type 2			LINER			Composite			SF			Unknown		
	ϕ^b	σ_ϕ^b	N	ϕ	σ_ϕ	N	ϕ	σ_ϕ	N	ϕ	σ_ϕ	N	ϕ	σ_ϕ	N	ϕ	σ_ϕ	N
10.6	2.13×10^{-6}	1.42×10^{-7}	229	1.14×10^{-6}	1.14×10^{-7}	109	5.07×10^{-7}	8.30×10^{-8}	46	2.21×10^{-6}	1.68×10^{-7}	206	2.02×10^{-6}	1.54×10^{-7}	199	8.94×10^{-8}	3.88×10^{-8}	7
11.0	5.46×10^{-7}	7.07×10^{-8}	59	9.58×10^{-8}	3.04×10^{-8}	10	5.62×10^{-8}	2.30×10^{-8}	6	1.15×10^{-7}	3.34×10^{-8}	12	4.16×10^{-8}	2.10×10^{-8}	4	0
11.4	6.53×10^{-8}	2.44×10^{-8}	7	9.20×10^{-9}	9.20×10^{-9}	1	2.07×10^{-8}	1.32×10^{-8}	2	0	0	0
$0.15 \leq z < 0.2$																		
9.40	2.69×10^{-7}	2.69×10^{-7}	1	0	1.25×10^{-6}	2.53×10^{-7}	32	2.35×10^{-6}	6.46×10^{-7}	18	6.21×10^{-6}	2.61×10^{-6}	69	3.46×10^{-7}	1.47×10^{-7}	6
9.80	2.44×10^{-6}	4.13×10^{-7}	280	5.82×10^{-6}	4.06×10^{-7}	441	7.67×10^{-6}	4.39×10^{-7}	773	3.78×10^{-5}	1.18×10^{-6}	3076	9.17×10^{-5}	2.44×10^{-6}	5882	4.29×10^{-6}	2.77×10^{-7}	406
10.2	4.51×10^{-6}	1.56×10^{-7}	880	4.97×10^{-6}	4.66×10^{-7}	532	2.59×10^{-6}	1.98×10^{-7}	349	2.01×10^{-5}	6.38×10^{-7}	2411	4.78×10^{-5}	1.10×10^{-6}	5246	1.28×10^{-6}	1.29×10^{-7}	173
10.6	2.34×10^{-6}	1.08×10^{-7}	468	8.80×10^{-7}	9.16×10^{-8}	128	4.36×10^{-7}	6.79×10^{-8}	61	2.77×10^{-6}	1.99×10^{-7}	381	3.65×10^{-6}	2.08×10^{-7}	545	7.59×10^{-8}	2.34×10^{-8}	12
11.0	7.14×10^{-7}	5.98×10^{-8}	143	1.19×10^{-7}	2.90×10^{-8}	19	8.95×10^{-8}	2.93×10^{-8}	13	1.46×10^{-7}	3.36×10^{-8}	23	6.73×10^{-8}	2.71×10^{-8}	10	0
11.4	1.28×10^{-7}	2.59×10^{-8}	25	4.96×10^{-9}	4.96×10^{-9}	1	4.96×10^{-9}	4.96×10^{-9}	1	1.30×10^{-8}	7.67×10^{-9}	2	4.96×10^{-9}	4.96×10^{-9}	1	0
11.8	1.61×10^{-8}	8.68×10^{-9}	3	0	0	8.20×10^{-9}	8.20×10^{-9}	1	0	0
$0.2 \leq z < 0.25$																		
9.80	3.85×10^{-7}	1.23×10^{-7}	16	1.10×10^{-7}	4.89×10^{-8}	5	7.70×10^{-7}	1.79×10^{-7}	54	1.61×10^{-6}	2.68×10^{-7}	81	2.05×10^{-6}	2.66×10^{-7}	131	3.45×10^{-7}	8.31×10^{-8}	26
10.2	2.88×10^{-6}	1.19×10^{-7}	752	1.23×10^{-6}	1.72×10^{-7}	158	1.07×10^{-6}	1.18×10^{-7}	195	6.95×10^{-6}	3.72×10^{-7}	836	1.23×10^{-5}	5.01×10^{-7}	1341	5.43×10^{-7}	7.81×10^{-8}	81
10.6	2.80×10^{-6}	9.69×10^{-8}	862	3.67×10^{-7}	6.90×10^{-8}	59	1.82×10^{-7}	4.32×10^{-8}	29	1.88×10^{-6}	1.68×10^{-7}	285	2.81×10^{-6}	2.19×10^{-7}	420	6.05×10^{-8}	2.30×10^{-8}	12
11.0	7.68×10^{-7}	4.96×10^{-8}	241	1.01×10^{-7}	2.85×10^{-8}	19	2.63×10^{-8}	1.02×10^{-8}	7	1.77×10^{-7}	5.21×10^{-8}	27	5.97×10^{-8}	2.64×10^{-8}	10	8.04×10^{-9}	4.80×10^{-9}	2
11.4	1.22×10^{-7}	1.98×10^{-8}	38	0	0	1.22×10^{-8}	7.40×10^{-9}	3	0	4.97×10^{-9}	4.97×10^{-9}	1
11.8	2.25×10^{-8}	8.39×10^{-9}	7	3.17×10^{-9}	3.17×10^{-9}	1	0	0	0	0
$0.25 \leq z \leq 0.3$																		
10.2	9.32×10^{-7}	1.47×10^{-7}	163	3.22×10^{-8}	1.74×10^{-8}	4	1.00×10^{-7}	2.63×10^{-8}	20	3.19×10^{-7}	7.44×10^{-8}	42	5.37×10^{-7}	1.53×10^{-7}	49	3.95×10^{-8}	2.16×10^{-8}	6
10.6	2.05×10^{-6}	8.66×10^{-8}	753	9.37×10^{-8}	2.44×10^{-8}	19	3.90×10^{-7}	3.30×10^{-7}	18	3.07×10^{-7}	5.24×10^{-8}	60	4.78×10^{-7}	7.52×10^{-8}	82	2.22×10^{-8}	8.11×10^{-9}	8
11.0	9.32×10^{-7}	4.86×10^{-8}	399	4.81×10^{-8}	3.44×10^{-8}	4	6.08×10^{-9}	3.55×10^{-9}	2	1.17×10^{-7}	4.40×10^{-8}	17	4.73×10^{-8}	1.63×10^{-8}	12	2.59×10^{-9}	2.59×10^{-9}	1
11.4	1.81×10^{-7}	2.17×10^{-8}	76	1.03×10^{-8}	6.13×10^{-9}	2	1.20×10^{-8}	7.50×10^{-9}	2	1.02×10^{-8}	6.58×10^{-9}	2	4.67×10^{-9}	4.67×10^{-9}	1	0
11.8	1.59×10^{-8}	6.01×10^{-9}	7	0	0	0	0	0
12.2	2.24×10^{-9}	2.24×10^{-9}	1	0	0	0	0	0

Table 8—Continued

type 1			type 2			LINER			Composite			SF		Unknown				
$\log L^a$	ϕ^b	σ_ϕ^b	N	ϕ	σ_ϕ	N	ϕ	σ_ϕ	N	ϕ	σ_ϕ	N	ϕ	σ_ϕ	N	ϕ	σ_ϕ	N
$0.006 \leq z \leq 0.3$																		
6.60	0	0	0	1.14×10^{-4}	1.14×10^{-4}	1	9.40×10^{-4}	4.03×10^{-4}	6	0
7.00	0	6.96×10^{-5}	5.49×10^{-5}	2	0	1.47×10^{-4}	6.74×10^{-5}	5	2.82×10^{-3}	3.40×10^{-4}	92	0
7.40	0	7.56×10^{-6}	5.37×10^{-6}	2	4.16×10^{-5}	1.69×10^{-5}	8	6.10×10^{-5}	1.97×10^{-5}	12	1.82×10^{-3}	1.16×10^{-4}	293	0
7.80	1.39×10^{-6}	1.39×10^{-6}	1	3.28×10^{-5}	7.14×10^{-6}	26	1.21×10^{-4}	1.39×10^{-5}	88	1.21×10^{-4}	1.34×10^{-5}	94	1.48×10^{-3}	5.07×10^{-5}	1038	1.19×10^{-5}	4.29×10^{-6}	8
8.20	3.30×10^{-6}	1.37×10^{-6}	7	6.78×10^{-5}	5.77×10^{-6}	160	2.50×10^{-4}	1.05×10^{-5}	649	2.76×10^{-4}	1.11×10^{-5}	712	1.90×10^{-3}	3.06×10^{-5}	4613	2.46×10^{-5}	3.59×10^{-6}	57
8.60	1.51×10^{-6}	4.11×10^{-7}	15	5.34×10^{-5}	2.72×10^{-6}	445	2.21×10^{-4}	5.28×10^{-6}	2022	3.10×10^{-4}	6.45×10^{-6}	2751	1.53×10^{-3}	1.56×10^{-5}	12487	1.80×10^{-5}	1.56×10^{-6}	154
9.00	5.98×10^{-6}	6.57×10^{-7}	151	4.32×10^{-5}	1.41×10^{-6}	1185	1.25×10^{-4}	2.18×10^{-6}	3878	3.03×10^{-4}	6.13×10^{-6}	8281	1.22×10^{-3}	8.56×10^{-6}	29497	1.65×10^{-5}	9.20×10^{-7}	446
9.40	6.78×10^{-6}	3.54×10^{-7}	562	3.40×10^{-5}	8.92×10^{-7}	2279	4.85×10^{-5}	8.91×10^{-7}	4146	2.23×10^{-4}	2.24×10^{-6}	15462	7.40×10^{-4}	4.26×10^{-6}	44129	1.29×10^{-5}	4.91×10^{-7}	965
9.80	6.73×10^{-6}	2.36×10^{-7}	1440	1.70×10^{-5}	4.64×10^{-7}	2383	1.46×10^{-5}	4.21×10^{-7}	2554	1.03×10^{-4}	1.13×10^{-6}	14675	2.77×10^{-4}	1.77×10^{-6}	35865	6.18×10^{-6}	2.41×10^{-7}	1042
10.2	5.14×10^{-6}	1.42×10^{-7}	2611	6.13×10^{-6}	2.27×10^{-7}	1328	3.54×10^{-6}	1.49×10^{-7}	949	2.44×10^{-5}	4.20×10^{-7}	5782	5.01×10^{-5}	5.56×10^{-7}	11902	1.12×10^{-6}	7.85×10^{-8}	344
10.6	2.72×10^{-6}	7.05×10^{-8}	2353	1.16×10^{-6}	7.62×10^{-8}	334	5.36×10^{-7}	5.24×10^{-8}	164	2.89×10^{-6}	1.16×10^{-7}	969	3.37×10^{-6}	1.16×10^{-7}	1283	1.08×10^{-7}	2.26×10^{-8}	40
11.0	8.62×10^{-7}	3.37×10^{-8}	847	1.51×10^{-7}	2.75×10^{-8}	55	6.34×10^{-8}	1.41×10^{-8}	28	1.93×10^{-7}	2.63×10^{-8}	82	7.18×10^{-8}	1.57×10^{-8}	36	2.89×10^{-9}	9.68×10^{-9}	3
11.4	1.45×10^{-7}	1.26×10^{-8}	146	7.93×10^{-9}	3.89×10^{-9}	4	1.12×10^{-8}	5.52×10^{-9}	5	3.91×10^{-8}	2.81×10^{-8}	8	2.02×10^{-9}	1.44×10^{-9}	2	1.79×10^{-9}	1.79×10^{-9}	1
11.8	1.54×10^{-8}	3.75×10^{-9}	17	9.44×10^{-10}	9.44×10^{-10}	1	0	3.59×10^{-9}	3.59×10^{-9}	1	0	0

Note. — Table 8 is published in its entirety in the electronic edition of the *Astrophysical Journal*. A portion is shown here for guidance regarding its form and content.

^a L_\odot

^b $\text{Mpc}^{-3} \text{Mag}^{-1}$

Table 9. The 22- μm LFs for each galaxy category at each redshift.

$\log L^a$	type 1			type 2			LINER			Composite			SF			Unknown		
	ϕ^b	σ_ϕ^b	N	ϕ	σ_ϕ	N	ϕ	σ_ϕ	N	ϕ	σ_ϕ	N	ϕ	σ_ϕ	N	ϕ	σ_ϕ	N
$0.006 \leq z < 0.05$																		
7.40	0	0	0	0	2.34×10^{-3}	7.70×10^{-4}	14	0
7.80	0	0	4.48×10^{-5}	2.24×10^{-5}	4	1.29×10^{-4}	6.72×10^{-5}	4	1.40×10^{-3}	2.00×10^{-4}	63	1.93×10^{-5}	1.93×10^{-5}	1
8.20	6.02×10^{-6}	6.02×10^{-6}	1	5.08×10^{-5}	1.82×10^{-5}	9	5.92×10^{-5}	1.78×10^{-5}	13	1.03×10^{-4}	2.27×10^{-5}	24	1.01×10^{-3}	7.92×10^{-5}	195	0
8.60	1.57×10^{-6}	1.01×10^{-6}	2	2.87×10^{-5}	5.96×10^{-6}	27	9.30×10^{-5}	1.08×10^{-5}	88	1.62×10^{-4}	1.36×10^{-5}	163	9.00×10^{-4}	3.53×10^{-5}	761	1.01×10^{-5}	3.80×10^{-6}	8
9.00	7.87×10^{-6}	1.74×10^{-6}	22	3.43×10^{-5}	3.58×10^{-6}	104	9.44×10^{-5}	6.01×10^{-6}	283	2.06×10^{-4}	8.68×10^{-6}	648	7.04×10^{-4}	1.66×10^{-5}	2079	7.35×10^{-6}	1.63×10^{-6}	23
9.40	7.59×10^{-6}	1.13×10^{-6}	46	2.23×10^{-5}	1.90×10^{-6}	138	2.90×10^{-5}	2.17×10^{-6}	179	1.26×10^{-4}	6.57×10^{-6}	746	2.85×10^{-4}	6.97×10^{-6}	1737	2.77×10^{-6}	6.72×10^{-7}	17
9.80	6.19×10^{-6}	9.94×10^{-7}	38	1.23×10^{-5}	1.41×10^{-6}	76	9.35×10^{-6}	1.23×10^{-6}	58	4.78×10^{-5}	2.78×10^{-6}	296	6.53×10^{-5}	3.24×10^{-6}	406	5.14×10^{-7}	2.80×10^{-7}	3
10.2	2.26×10^{-6}	6.01×10^{-7}	14	3.38×10^{-6}	7.36×10^{-7}	21	2.26×10^{-6}	6.01×10^{-7}	14	1.08×10^{-5}	1.33×10^{-6}	67	7.88×10^{-6}	1.12×10^{-6}	49	1.61×10^{-7}	1.61×10^{-7}	1
10.6	1.61×10^{-7}	1.61×10^{-7}	1	3.34×10^{-7}	2.27×10^{-7}	2	3.25×10^{-7}	2.27×10^{-7}	2	2.11×10^{-6}	5.80×10^{-7}	13	5.02×10^{-7}	2.79×10^{-7}	3	0
11.0	0	0	1.61×10^{-7}	1.61×10^{-7}	1	0	0	0
$0.05 \leq z < 0.1$																		
9.00	0	0	2.52×10^{-6}	2.52×10^{-6}	1	0	0	0
9.40	4.08×10^{-6}	8.13×10^{-7}	31	1.32×10^{-5}	1.72×10^{-6}	82	1.37×10^{-5}	1.89×10^{-6}	86	7.81×10^{-5}	7.00×10^{-6}	423	2.32×10^{-4}	1.04×10^{-5}	1319	3.84×10^{-6}	2.15×10^{-6}	15
9.80	7.40×10^{-6}	5.32×10^{-7}	220	1.31×10^{-5}	7.98×10^{-7}	322	8.01×10^{-6}	6.14×10^{-7}	199	5.44×10^{-5}	1.61×10^{-6}	1400	1.16×10^{-4}	2.51×10^{-6}	2972	1.26×10^{-6}	2.49×10^{-7}	31
10.2	5.29×10^{-6}	3.56×10^{-7}	221	6.02×10^{-6}	3.97×10^{-7}	239	3.54×10^{-6}	3.18×10^{-7}	135	2.29×10^{-5}	1.06×10^{-6}	809	2.35×10^{-5}	8.96×10^{-7}	895	4.63×10^{-7}	1.23×10^{-7}	16
10.6	1.98×10^{-6}	2.21×10^{-7}	82	1.81×10^{-6}	2.14×10^{-7}	73	6.69×10^{-7}	1.26×10^{-7}	28	4.36×10^{-6}	3.70×10^{-7}	162	3.06×10^{-6}	3.17×10^{-7}	113	5.12×10^{-8}	3.39×10^{-8}	2
11.0	2.96×10^{-7}	8.59×10^{-8}	12	1.73×10^{-7}	6.34×10^{-8}	7	1.59×10^{-7}	6.64×10^{-8}	6	5.15×10^{-7}	1.21×10^{-7}	20	1.31×10^{-7}	5.46×10^{-8}	5	5.20×10^{-8}	3.40×10^{-8}	2
11.4	7.52×10^{-8}	4.15×10^{-8}	3	5.03×10^{-8}	3.38×10^{-8}	2	0	1.05×10^{-7}	5.32×10^{-8}	4	0	0
$0.1 \leq z < 0.15$																		
9.80	7.10×10^{-7}	2.52×10^{-7}	9	2.82×10^{-7}	1.37×10^{-7}	5	1.01×10^{-6}	7.64×10^{-7}	6	4.37×10^{-6}	7.36×10^{-7}	55	1.57×10^{-5}	1.55×10^{-6}	216	2.88×10^{-7}	2.22×10^{-7}	3
10.2	3.98×10^{-6}	2.72×10^{-7}	271	5.47×10^{-6}	4.27×10^{-7}	258	2.69×10^{-6}	2.61×10^{-7}	147	1.75×10^{-5}	9.04×10^{-7}	811	2.41×10^{-5}	9.40×10^{-7}	1269	7.34×10^{-7}	1.83×10^{-7}	29
10.6	2.86×10^{-6}	1.64×10^{-7}	307	2.14×10^{-6}	1.76×10^{-7}	188	1.08×10^{-6}	1.42×10^{-7}	90	4.90×10^{-6}	2.68×10^{-7}	420	3.63×10^{-6}	2.54×10^{-7}	298	1.16×10^{-7}	4.18×10^{-8}	10
11.0	1.01×10^{-6}	9.67×10^{-8}	109	5.25×10^{-7}	7.54×10^{-8}	52	3.75×10^{-7}	9.54×10^{-8}	27	7.83×10^{-7}	9.35×10^{-8}	75	3.79×10^{-7}	8.18×10^{-8}	31	9.20×10^{-9}	9.20×10^{-9}	1
11.4	2.42×10^{-7}	4.70×10^{-8}	26	4.08×10^{-8}	1.88×10^{-8}	4	9.20×10^{-9}	9.20×10^{-9}	1	1.30×10^{-7}	5.37×10^{-8}	9	4.94×10^{-8}	2.54×10^{-8}	3	1.18×10^{-8}	1.18×10^{-8}	1
11.8	2.85×10^{-8}	1.60×10^{-8}	3	0	2.21×10^{-8}	1.35×10^{-8}	2	0	0	0

Table 9—Continued

log L^a	type 1			type 2			LINER			Composite			SF			Unknown		
	ϕ^b	σ_ϕ^b	N	ϕ	σ_ϕ	N	ϕ	σ_ϕ	N	ϕ	σ_ϕ	N	ϕ	σ_ϕ	N	ϕ	σ_ϕ	N
$0.15 \leq z < 0.2$																		
10.2	4.25×10^{-7}	1.30×10^{-7}	16	7.00×10^{-7}	2.71×10^{-7}	14	1.10×10^{-7}	5.68×10^{-8}	4	9.60×10^{-7}	2.18×10^{-7}	39	2.76×10^{-6}	4.47×10^{-7}	101	1.93×10^{-8}	1.93×10^{-8}	1
10.6	1.82×10^{-6}	1.25×10^{-7}	273	1.64×10^{-6}	3.62×10^{-7}	102	6.35×10^{-7}	1.25×10^{-7}	50	2.44×10^{-6}	2.26×10^{-7}	229	1.89×10^{-6}	1.87×10^{-7}	198	3.07×10^{-8}	1.67×10^{-8}	4
11.0	1.18×10^{-6}	7.69×10^{-8}	235	5.23×10^{-7}	7.24×10^{-8}	69	1.77×10^{-7}	3.47×10^{-8}	29	6.40×10^{-7}	1.25×10^{-7}	67	2.52×10^{-7}	7.95×10^{-8}	26	3.20×10^{-8}	1.51×10^{-8}	5
11.4	2.65×10^{-7}	3.70×10^{-8}	52	3.37×10^{-8}	1.42×10^{-8}	6	6.15×10^{-8}	2.60×10^{-8}	8	1.16×10^{-7}	4.94×10^{-8}	13	1.67×10^{-8}	8.79×10^{-9}	3	4.96×10^{-9}	4.96×10^{-9}	1
11.8	7.22×10^{-8}	1.88×10^{-8}	14	4.96×10^{-9}	4.96×10^{-9}	1	0	4.96×10^{-9}	4.96×10^{-9}	1	0	1.85×10^{-8}	1.85×10^{-8}	1
12.2	4.96×10^{-9}	4.96×10^{-9}	1	0	0	8.20×10^{-9}	8.20×10^{-9}	1	0	0
$0.2 \leq z < 0.25$																		
10.6	6.83×10^{-7}	9.31×10^{-8}	97	1.84×10^{-8}	1.16×10^{-8}	2	1.40×10^{-8}	8.31×10^{-9}	2	4.22×10^{-7}	1.15×10^{-7}	32	2.53×10^{-7}	5.67×10^{-8}	27	1.50×10^{-8}	1.50×10^{-8}	11
11.0	1.06×10^{-6}	6.36×10^{-8}	305	1.24×10^{-7}	3.98×10^{-8}	19	4.41×10^{-8}	1.96×10^{-8}	7	2.49×10^{-7}	6.36×10^{-8}	32	7.53×10^{-8}	2.89×10^{-8}	11	6.65×10^{-9}	4.71×10^{-9}	1
11.4	3.28×10^{-7}	3.27×10^{-8}	102	3.92×10^{-8}	1.60×10^{-8}	7	1.24×10^{-8}	7.40×10^{-9}	3	5.42×10^{-8}	2.77×10^{-8}	6	3.17×10^{-9}	3.17×10^{-9}	1	4.97×10^{-9}	4.97×10^{-9}	1
11.8	4.17×10^{-8}	1.16×10^{-8}	13	7.23×10^{-9}	4.57×10^{-9}	2	0	5.89×10^{-9}	5.89×10^{-9}	1	0	0
12.2	1.05×10^{-8}	5.58×10^{-9}	3	3.17×10^{-9}	3.17×10^{-9}	1	0	0	0	0
$0.25 \leq z \leq 0.3$																		
10.6	3.40×10^{-8}	2.09×10^{-8}	3	0	0	0	2.98×10^{-8}	1.98×10^{-8}	2	0
11.0	4.98×10^{-7}	5.78×10^{-8}	146	3.08×10^{-9}	3.08×10^{-9}	1	3.30×10^{-7}	3.30×10^{-7}	1	6.32×10^{-8}	3.69×10^{-8}	7	5.09×10^{-9}	5.09×10^{-9}	1	0
11.4	2.91×10^{-7}	2.61×10^{-8}	127	4.67×10^{-8}	3.41×10^{-8}	4	8.44×10^{-9}	6.59×10^{-9}	2	2.70×10^{-8}	1.84×10^{-8}	4	4.67×10^{-9}	4.67×10^{-9}	1	0
11.8	9.65×10^{-8}	1.67×10^{-8}	38	0	3.58×10^{-9}	3.58×10^{-9}	1	1.02×10^{-8}	6.58×10^{-9}	2	0	0
12.2	2.24×10^{-9}	2.24×10^{-9}	1	0	0	0	0	0
12.6	2.24×10^{-9}	2.24×10^{-9}	1	0	0	0	0	0
13.4	2.24×10^{-9}	2.24×10^{-9}	1	0	0	0	0	0
$0.006 \leq z \leq 0.3$																		
7.40	0	0	0	0	2.34×10^{-3}	7.70×10^{-4}	14	0
7.80	0	0	4.46×10^{-5}	2.24×10^{-5}	4	1.29×10^{-4}	6.72×10^{-5}	4	1.40×10^{-3}	2.00×10^{-4}	63	1.93×10^{-5}	1.93×10^{-5}	1

C. Luminosity and Redshift Dependences of the CF for the Sample Including the Outside the AGN wedge

In Section 4.2, we demonstrated that the MIR emission from optically classified (especially for less luminous) AGNs could be substantially affected by emission from their host galaxies, and we attempted to extract the AGN-dominated MIR objects based on their MIR colors (AGN wedge selection) to calculate the CF. We also discussed only 22- μm -selected AGNs in Section 4.2 to omit the influence of the PAH contribution. Nevertheless, it is worthwhile presenting the estimated CF for the sample including the outside the AGN wedge (i.e., without considering the AGN wedge) and a CF estimate from the 12- μm sample. Hence, we show the values of the CF based on the 12- and 22- μm *WISE*-SDSS sample. Figures 31 and 32 represent the resultant CF at $0.006 \leq z \leq 0.2$ and in each redshift bin, respectively. The data in these figures are also given in Tables 10 and 11. As described in Section 4.2, the CF seems to be overestimated particularly in the low-luminosity region, compared to those in Figure 19. In addition, when comparing Figures 26 and 31 (right), there are many low luminosity type 2 AGNs that are missing from the “wedge” selected sample that are classed as AGN in the SDSS. In Section 4.4, we performed model fitting to the data in the AGN wedge and concluded that the modified receding torus model explains the data well. Since only AGN-dominant MIR sources were considered for Figure 26, the behavior of these sources likely represents the true luminosity dependence of the CF unbiased by host emission, although some uncertainties (e.g., the influence of the optically-faint MIR sources) still remain as described in Section 4.3.2. Nevertheless, a more complete AGN sample obtained by using only the SDSS may give a more reliable picture at the low luminosity end when discussing the torus model.

Table 9—Continued

log L^a	type 1			type 2			LINER			Composite			SF			Unknown		
	ϕ^b	σ_ϕ^b	N	ϕ	σ_ϕ	N	ϕ	σ_ϕ	N	ϕ	σ_ϕ	N	ϕ	σ_ϕ	N	ϕ	σ_ϕ	N
8.20	6.02×10^{-6}	6.02×10^{-6}	1	5.06×10^{-5}	1.82×10^{-5}	9	5.90×10^{-5}	1.78×10^{-5}	13	1.03×10^{-4}	2.27×10^{-5}	24	1.01×10^{-3}	7.92×10^{-5}	195	0
8.60	1.41×10^{-6}	9.94×10^{-7}	2	2.85×10^{-5}	5.96×10^{-6}	27	9.28×10^{-5}	1.08×10^{-5}	88	1.62×10^{-4}	1.36×10^{-5}	163	8.99×10^{-4}	3.53×10^{-5}	761	9.91×10^{-6}	3.80×10^{-6}	8
9.00	7.71×10^{-6}	1.74×10^{-6}	22	3.41×10^{-5}	3.58×10^{-6}	104	9.45×10^{-5}	6.01×10^{-6}	284	2.06×10^{-4}	8.68×10^{-6}	648	7.04×10^{-4}	1.66×10^{-5}	2079	7.19×10^{-6}	1.62×10^{-6}	23
9.40	7.42×10^{-6}	9.36×10^{-7}	77	2.10×10^{-5}	1.51×10^{-6}	220	2.51×10^{-5}	1.66×10^{-6}	265	1.14×10^{-4}	5.94×10^{-6}	1169	2.88×10^{-4}	5.79×10^{-6}	3056	3.03×10^{-6}	5.78×10^{-7}	32
9.80	7.16×10^{-6}	4.70×10^{-7}	267	1.34×10^{-5}	7.64×10^{-7}	403	8.50×10^{-6}	5.87×10^{-7}	263	5.42×10^{-5}	1.45×10^{-6}	1751	1.07×10^{-4}	1.99×10^{-6}	3594	1.13×10^{-6}	1.98×10^{-7}	37
10.2	4.69×10^{-6}	2.33×10^{-7}	522	6.40×10^{-6}	3.15×10^{-7}	532	3.69×10^{-6}	2.56×10^{-7}	300	2.26×10^{-5}	7.13×10^{-7}	1726	2.58×10^{-5}	6.34×10^{-7}	2314	6.10×10^{-7}	1.04×10^{-7}	47
10.6	2.47×10^{-6}	1.06×10^{-7}	763	2.27×10^{-6}	1.44×10^{-7}	367	9.81×10^{-7}	8.73×10^{-8}	172	5.74×10^{-6}	2.72×10^{-7}	856	4.02×10^{-6}	2.20×10^{-7}	641	9.03×10^{-8}	2.39×10^{-8}	17
11.0	1.15×10^{-6}	5.39×10^{-8}	807	5.43×10^{-7}	5.22×10^{-8}	148	3.17×10^{-7}	5.32×10^{-8}	71	9.10×10^{-7}	8.81×10^{-8}	201	3.40×10^{-7}	5.04×10^{-8}	74	4.21×10^{-8}	1.93×10^{-8}	10
11.4	3.38×10^{-7}	2.28×10^{-8}	310	5.08×10^{-8}	1.14×10^{-8}	23	2.95×10^{-8}	8.85×10^{-9}	14	1.62×10^{-7}	4.00×10^{-8}	36	3.04×10^{-8}	1.44×10^{-8}	8	1.30×10^{-8}	8.28×10^{-9}	3
11.8	6.88×10^{-8}	8.71×10^{-9}	68	4.77×10^{-9}	3.05×10^{-9}	3	9.64×10^{-9}	5.70×10^{-9}	3	6.93×10^{-9}	3.30×10^{-9}	4	0	4.74×10^{-9}	4.74×10^{-9}	1
12.2	4.61×10^{-9}	2.06×10^{-9}	5	9.44×10^{-10}	9.44×10^{-10}	1	0	3.59×10^{-9}	3.59×10^{-9}	1	0	0
12.6	8.92×10^{-10}	8.92×10^{-10}	1	0	0	0	0	0
13.4	8.92×10^{-10}	8.92×10^{-10}	1	0	0	0	0	0

Note. — Table 9 is published in its entirety in the electronic edition of the *Astrophysical Journal*. A portion is shown here for guidance regarding its form and content.

^a L_\odot

^b $\text{Mpc}^{-3} \text{Mag}^{-1}$

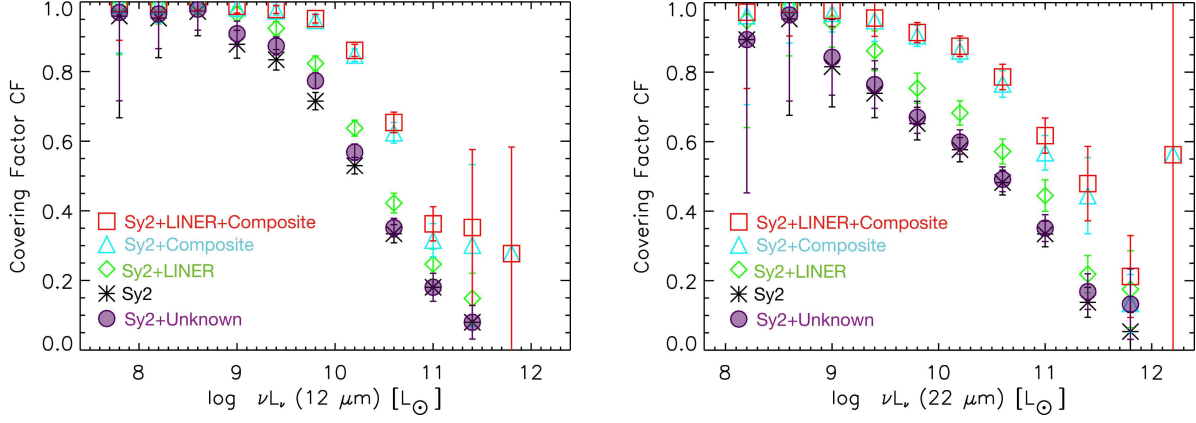


Fig. 31.— Variation in the CF with the 12- μm (left) and 22- μm (right) luminosities at $0.006 \leq z \leq 0.2$ without considering the AGN wedge.

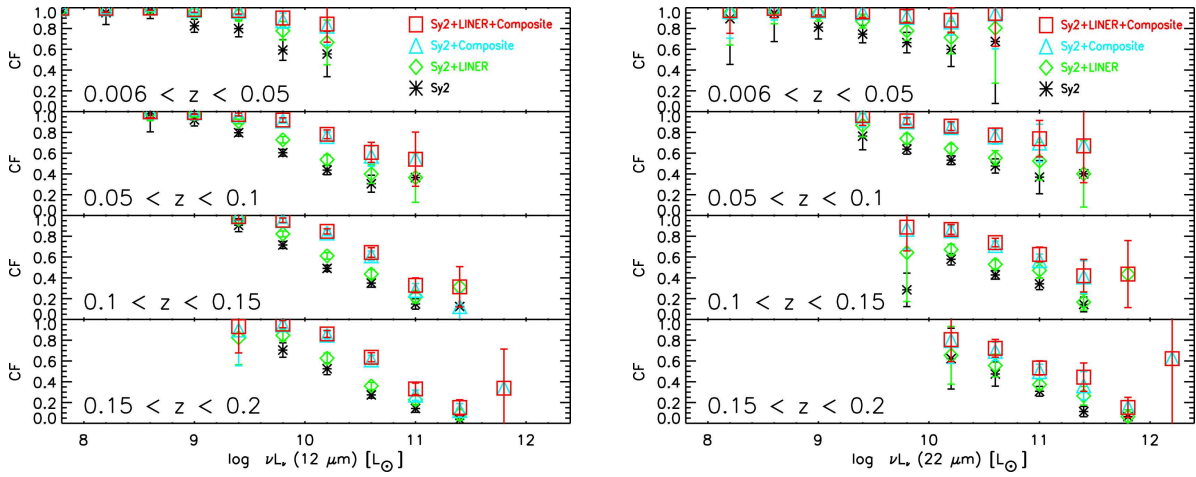


Fig. 32.— Variation in the CF with the 12- μm (left) and 22- μm (right) luminosities for all samples in different redshift bins without considering the AGN wedge.

Table 10. CFs as a function of the 12- μ m luminosity for each type 2 AGN definition without considering the AGN wedge.

log L	Sy2s		Sy2s + LINERs		Sy2s + Composites		Sy2s + LINERs + Composites	
	CF	σ_{CF}	CF	σ_{CF}	CF	σ_{CF}	CF	σ_{CF}
$0.006 \leq z < 0.05$								
7.80	0.96	0.29	0.99	0.14	0.99	0.14	0.99	0.11
8.20	0.95	0.11	0.99	0.05	0.99	0.05	0.99	0.04
8.60	0.97	0.07	0.99	0.03	1.00	0.03	1.00	0.02
9.00	0.83	0.06	0.95	0.04	0.97	0.03	0.98	0.03
9.40	0.80	0.08	0.93	0.05	0.96	0.04	0.97	0.03
9.80	0.59	0.10	0.78	0.09	0.88	0.07	0.90	0.07
10.2	0.55	0.22	0.67	0.21	0.82	0.18	0.84	0.17
$0.05 \leq z < 0.1$								
8.60	0.98	0.17	1.00	0.08	1.00	0.07	1.00	0.06
9.00	0.92	0.06	0.98	0.03	0.99	0.02	0.99	0.02
9.40	0.80	0.03	0.91	0.02	0.97	0.02	0.97	0.01
9.80	0.60	0.03	0.73	0.03	0.91	0.02	0.92	0.02
10.2	0.44	0.04	0.54	0.05	0.76	0.04	0.78	0.04
10.6	0.31	0.08	0.40	0.09	0.57	0.10	0.61	0.10
11.0	0.36	0.24	0.36	0.24	0.54	0.26	0.54	0.26
$0.1 \leq z < 0.15$								
9.40	0.91	0.06	0.96	0.04	0.99	0.04	0.99	0.03
9.80	0.72	0.03	0.82	0.03	0.95	0.02	0.95	0.02
10.2	0.49	0.03	0.61	0.03	0.83	0.03	0.85	0.03
10.6	0.35	0.04	0.44	0.04	0.61	0.05	0.64	0.05
11.0	0.15	0.05	0.22	0.06	0.28	0.07	0.33	0.07
11.4	0.12	0.13	0.31	0.19	0.12	0.13	0.31	0.19
$0.15 \leq z \leq 0.2$								
9.40	—	—	0.82	0.26	0.90	0.34	0.93	0.25
9.80	0.71	0.07	0.85	0.05	0.95	0.04	0.95	0.03
10.2	0.52	0.06	0.63	0.05	0.85	0.04	0.86	0.03
10.6	0.27	0.03	0.36	0.03	0.61	0.04	0.64	0.04
11.0	0.14	0.04	0.23	0.05	0.27	0.05	0.33	0.06
11.4	0.04	0.04	0.08	0.05	0.12	0.07	0.15	0.07
11.8	—	—	—	—	0.34	0.38	0.34	0.38
$0.006 \leq z \leq 0.15$								
7.80	0.96	0.29	0.99	0.14	0.99	0.14	0.99	0.11
8.20	0.95	0.11	0.99	0.05	0.99	0.05	0.99	0.04

Table 10—Continued

log L	Sy2s		Sy2s + LINERs		Sy2s + Composites		Sy2s + LINERs + Composites	
	CF	σ_{CF}	CF	σ_{CF}	CF	σ_{CF}	CF	σ_{CF}
8.60	0.97	0.07	0.99	0.03	1.00	0.03	1.00	0.02
9.00	0.88	0.04	0.97	0.02	0.98	0.03	0.99	0.02
9.40	0.83	0.03	0.92	0.02	0.97	0.01	0.98	0.01
9.80	0.68	0.02	0.80	0.02	0.94	0.01	0.94	0.01
10.2	0.49	0.03	0.60	0.03	0.82	0.02	0.84	0.02
10.6	0.34	0.04	0.43	0.04	0.60	0.04	0.63	0.04
11.0	0.19	0.06	0.24	0.07	0.32	0.07	0.36	0.07
11.4	0.12	0.13	0.32	0.19	0.43	0.40	0.51	0.37
$0.006 \leq z \leq 0.2$								
7.80	0.96	0.29	0.99	0.14	0.99	0.14	0.99	0.11
8.20	0.95	0.11	0.99	0.05	0.99	0.05	0.99	0.04
8.60	0.97	0.07	0.99	0.03	1.00	0.03	1.00	0.02
9.00	0.88	0.04	0.97	0.02	0.98	0.03	0.99	0.02
9.40	0.83	0.03	0.92	0.02	0.97	0.01	0.98	0.01
9.80	0.72	0.02	0.82	0.02	0.95	0.01	0.95	0.01
10.2	0.53	0.02	0.64	0.02	0.85	0.02	0.86	0.02
10.6	0.33	0.03	0.42	0.03	0.62	0.03	0.65	0.03
11.0	0.18	0.04	0.25	0.04	0.32	0.05	0.36	0.05
11.4	0.08	0.05	0.15	0.07	0.30	0.23	0.35	0.22
11.8	—	—	—	—	0.28	0.31	0.28	0.31

Table 11. CFs as a function of the 22- μ m luminosity for each type 2 AGN definition without considering the AGN wedge.

log L	Sy2s		Sy2s + LINERs		Sy2s + Composites		Sy2s + LINERs + Composites	
	CF	σ_{CF}	CF	σ_{CF}	CF	σ_{CF}	CF	σ_{CF}
$0.006 \leq z < 0.05$								
8.20	0.89	0.44	0.95	0.31	0.96	0.26	0.97	0.22
8.60	0.95	0.27	0.99	0.14	0.99	0.11	0.99	0.09
9.00	0.81	0.11	0.94	0.07	0.97	0.05	0.98	0.05
9.40	0.75	0.08	0.87	0.07	0.95	0.06	0.96	0.05
9.80	0.66	0.10	0.78	0.09	0.91	0.06	0.92	0.06
10.2	0.60	0.16	0.71	0.16	0.86	0.13	0.88	0.12
10.6	0.68	0.60	0.80	0.53	0.94	0.33	0.94	0.32
$0.05 \leq z < 0.1$								
9.40	0.76	0.13	0.87	0.11	0.96	0.11	0.96	0.10
9.80	0.64	0.05	0.74	0.05	0.90	0.03	0.91	0.03
10.2	0.53	0.04	0.64	0.04	0.85	0.04	0.86	0.04
10.6	0.48	0.07	0.56	0.07	0.76	0.07	0.78	0.07
11.0	0.37	0.16	0.52	0.18	0.70	0.18	0.74	0.18
11.4	0.40	0.32	0.40	0.32	0.67	0.35	0.67	0.35
$0.1 \leq z < 0.15$								
9.80	0.28	0.16	0.64	0.47	0.87	0.19	0.89	0.23
10.2	0.58	0.05	0.67	0.05	0.85	0.05	0.87	0.05
10.6	0.43	0.04	0.53	0.04	0.71	0.04	0.74	0.04
11.0	0.34	0.06	0.47	0.07	0.56	0.06	0.63	0.07
11.4	0.14	0.07	0.17	0.08	0.41	0.16	0.42	0.16
11.8	—	—	0.44	0.32	—	—	0.44	0.32
$0.15 \leq z \leq 0.2$								
10.2	0.62	0.29	0.65	0.28	0.80	0.22	0.81	0.21
10.6	0.47	0.12	0.56	0.11	0.69	0.09	0.72	0.09
11.0	0.31	0.05	0.37	0.05	0.50	0.07	0.53	0.07
11.4	0.11	0.05	0.26	0.09	0.36	0.14	0.44	0.14
11.8	0.06	0.07	0.06	0.07	0.15	0.10	0.15	0.10
12.2	—	—	—	—	0.62	0.77	0.62	0.77
$0.006 \leq z \leq 0.15$								
8.20	0.89	0.44	0.95	0.31	0.96	0.26	0.97	0.22
8.60	0.95	0.28	0.99	0.14	0.99	0.11	1.00	0.09
9.00	0.82	0.12	0.94	0.07	0.97	0.05	0.98	0.05
9.40	0.74	0.07	0.86	0.06	0.95	0.06	0.96	0.05

Figures 33 and 34 show the dependence of our measured CF on redshift, which corresponds to Figures 20 and 21 in Section 4.2, respectively. We also see that in this case the CF does not appear to depend on redshift.

D. Number Density Ratios for Each Galaxy Type

In Section 3.1, we constructed the 12- and 22- μm LFs for each galaxy type in each redshift bin, and these data are listed in Tables 8 and 9. We also calculated the number density ratios for each galaxy type by integrating the 22- μm LFs, i.e.,

$$\Phi = \int_L \phi(L) dL \sim \sum_i \phi_i(L) \Delta L. \quad (\text{D1})$$

Table 12 summarizes the number density ratios normalized by the number density of the type 1 AGNs in each redshift bin.

Note that the luminosity range defines the integral range, so that the integral range is different for each redshift bin. As shown in Table 12, the number density ratio is sensitive to the luminosity range and the redshift. To compare the number density ratio of the type 2 to type 1 AGNs with that of Toba et al. (2013), which were based on AKARI 18- μm LFs, we choose the nearest redshift bin ($0.006 \leq z \leq 0.05$) and an integral range of $\log(\nu L_\nu) > 10^{10} L_\odot$ for both AGN types. We obtained a number ratio of 1.53 ± 0.50 , which is consistent within error with the value of 1.73 ± 0.36 obtained by Toba et al. (2013).

REFERENCES

- Ahn, C. P., et al. 2012, *ApJS*, 203, 21
- Aihara, H., et al. 2011, *ApJS*, 193, 29
- Akylas, A., Georgantopoulos, I., Georgakakis, A., Kitsionas, S., & Hatziminaoglou, E. 2006, *A&A*, 459, 693
- Antonucci, R. 1993, *Annual Review of A&A*, 31, 473
- Assef, R. J., et al. 2013, *ApJ*, 772, 26
- Baldwin, J. A., Phillips, M. M., & Terlevich, R. 1981, *PASP*, 93, 5
- Beckmann, V., et al. 2009, *A&A*, 505, 417

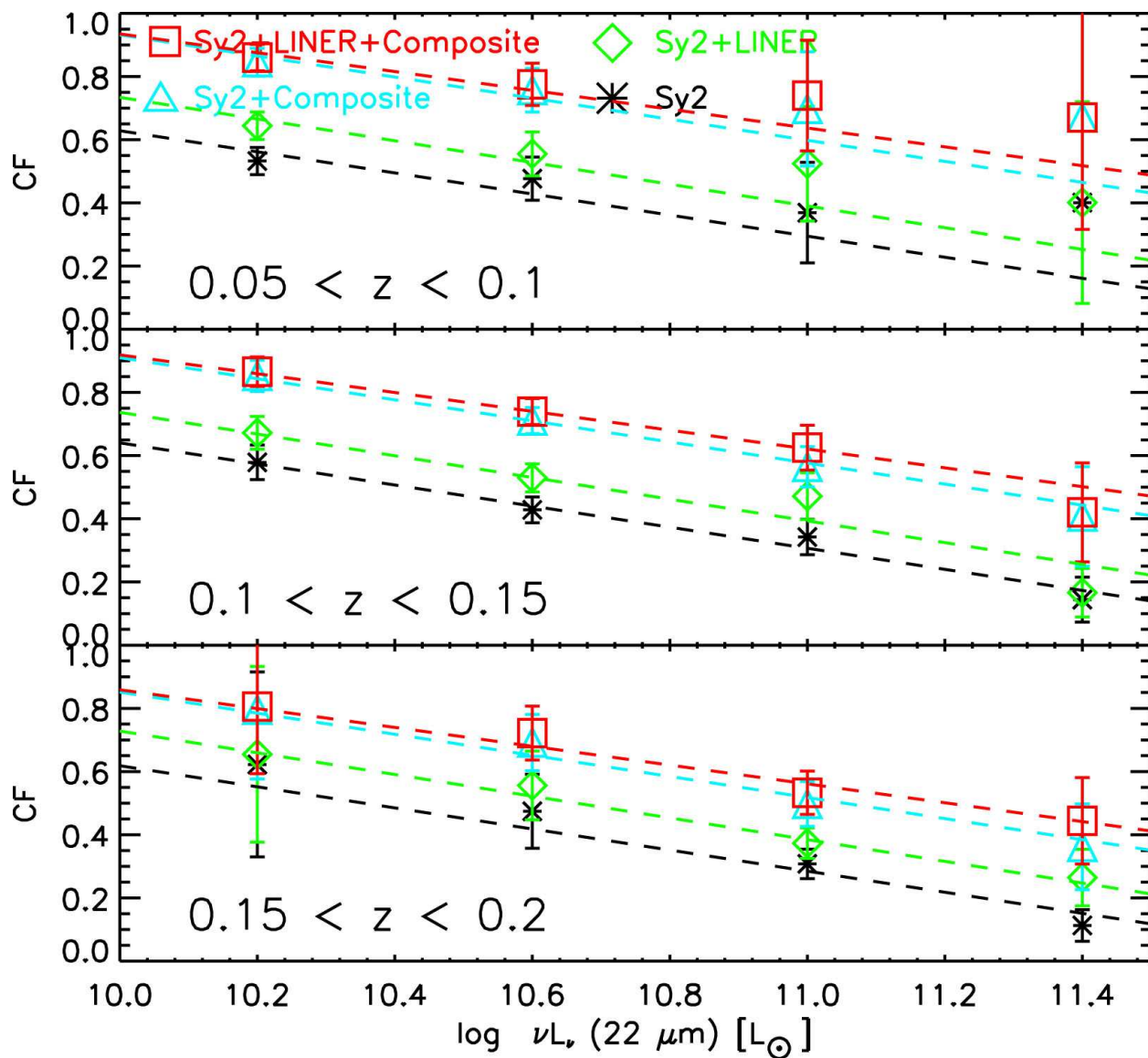


Fig. 33.— Variation in the CF with the 22- μm luminosity in different redshift bins without considering the AGN wedge. The dashed line shows the best-fit linear function with the slope fixed to the average value.

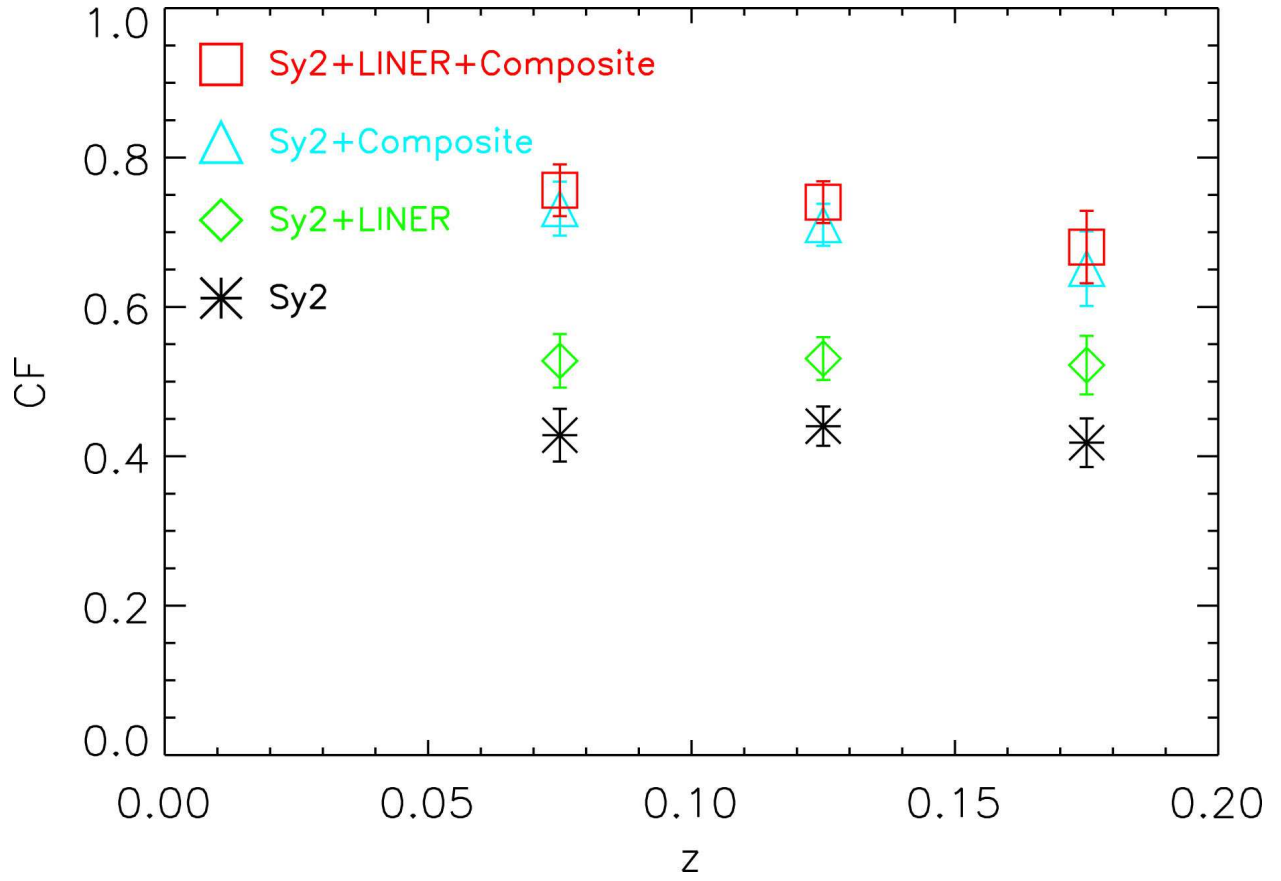


Fig. 34.— Dependence of the normalization of the CF at $\nu L_\nu(22 \mu\text{m}) = 10.6 L_\odot$ with redshift without considering the AGN wedge.

- Beichman, C. A., et al. 1988. in *Infrared astronomical satellite (IRAS) catalogs and atlases*
Volume 1: Explanatory supplement.
- Blanton, M. R., Lin, H., Lupton, R. H., Maley, F. M., Young, N., Zehavi, I., & Loveday, J.
2003, *AJ*, 125, 2276
- Blanton, M. R., & Roweis, S. 2007, *AJ*, 133, 734
- Burlon, D., Ajello, M., Greiner, J., Comastri, A., Merloni, A., & Gehrels, N. 2011, *ApJ*, 728,
58
- Caccianiga, A., Severgnini, P., Della Ceca, R., Maccacaro, T., Carrera, F. J., & Page, M. J.
2007, *A&A*, 470, 557
- Calderone, G., Sbarrato, T., & Ghisellini, G. 2012, *MNRAS*, 425, L41
- Donoso, E., et al. 2012, *ApJ*, 748, 80
- Driver, S. P., et al. 2011, *MNRAS*, 413, 971
- Driver, S. P., et al. 2009, *Astronomy and Geophysics*, 50, 12 Dwelly, T., & Page, M. J. 2006,
MNRAS, 372, 1755
- Eisenstein, D. J., et al. 2001, *AJ*, 122, 2267
- Fang, F., Shupe, D. L., Xu, C., & Hacking, P. B. 1998, *ApJ*, 500, 693
- Gandhi, P., et al. 2009, *A&A*, 502, 457
- Gehrels, N. 1986, *ApJ*, 303, 336
- Gu, M. 2013, *ApJ*, 773, 176
- Hasinger, G. 2008, *A&A*, 490, 905
- Hönig, S. F., & Beckert, T. 2007, *MNRAS*, 380, 1172
- Høg, E., et al. 2000, *A&A*, 355, L27
- Hopkins, A. M., et al. 2013, *MNRAS*, 430, 2047
- Horst, H., Gandhi, P., Smette, A., & Duschl, W. J. 2008, *A&A*, 479, 389

- Ichikawa, K., Ueda, Y., Terashima, Y., Oyabu, S., Gandhi, P., Matsuta, K., & Nakagawa, T. 2012, *ApJ*, 754, 45
- Ishihara, D., et al. 2010, *A&A*, 514, 1
- Jarrett, T. H., et al. 2011, *ApJ*, 735, 112
- Juneau, S., Dickinson, M., Alexander, D. M., & Salim, S. 2011, *ApJ*, 736, 104
- Kauffmann, G., et al. 2003, *MNRAS*, 346, 1055
- Kewley, L. J., Groves, B., Kauffmann, G., & Heckman, T. 2006, *MNRAS*, 372, 961
- Kewley, L. J., Heisler, C. A., Dopita, M. A., & Lumsden, S. 2001, *ApJS*, 132, 37
- La Franca, F., et al. 2005, *ApJ*, 635, 864
- Lawrence, A. 1991, *MNRAS*, 252, 586
- Lawrence, A., & Elvis, M. 2010, *ApJ*, 714, 561
- Lusso, E., et al. 2013, *ApJ*, 777, 86
- Ma, X.-C., & Wang, T.-G. 2013, *MNRAS*, 430, 3445
- Maiolino, R., Shemmer, O., Imanishi, M., Netzer, H., Oliva, E., Lutz, D., & Sturm, E. 2007, *A&A*, 468, 979
- Marshall, H. L. 1987, *AJ*, 94, 628
- Mateos, S., et al. 2012, *MNRAS*, 426, 3271
- Mateos, S., Alonso-Herrero, A., Carrera, F. J., Blain, A., Severgnini, P., Caccianiga, A., & Ruiz, A. 2013, *MNRAS*, 434, 941
- Matsuta, K., et al. 2012, *ApJ*, 753, 104
- Mor, R., & Trakhtenbrot, B. 2011, *ApJ*, 737, L36
- Murakami, H., et al. 2007, *PASJ*, 59, 369
- Neugebauer, G., et al. 1984, *ApJLetters*, 278, L1
- Ogle, P., Whyson, D., & Antonucci, R. 2006, *ApJ*, 647, 161
- Oyabu, S., et al. 2011, *A&A*, 529, 122

- Ricci, C., Paltani, S., Awaki, H., Petrucci, P.-O., Ueda, Y., & Brightman, M. 2013, *A&A*, 553, 29
- Petrosian, V. 1976, *ApJLetters*, 209, L1
- Richards, G. T., et al. 2002, *AJ*, 123, 2945
- Rodighiero, G., et al. 2010, *A&A*, 515, 8
- Roseboom, I. G., Lawrence, A., Elvis, M., Petty, S., Shen, Y., & Hao, H. 2013, *MNRAS*, 429, 1494
- Rush, B., Malkan, M. A., & Spinoglio, L. 1993, *ApJS*, 89, 1
- Schmidt, M. 1968, *ApJ*, 151, 393
- Simpson, C. 1998, *MNRAS*, 297, L39
- . 2005, *MNRAS*, 360, 565
- Spinoglio, L., Malkan, M. A., Rush, B., Carrasco, L., & Recillas-Cruz, E. 1995, *ApJ*, 453, 616
- Stern, D., et al. 2012, *The ApJ*, 753, 30
- Strauss, M. A., et al. 2002, *AJ*, 124, 1810
- Toba, Y., et al. 2013, *PASJ*, 65, 113
- Taylor, M. B., Arviset, C., Ponz, D., & Enrique, S. 2006, in *Astronomical Data Analysis Software and Systems XV*, ed. C. Gabriel, 666
- Urry, C. M., & Padovani, P. 1995, *PASP*, 107, 803
- Veilleux, S., & Osterbrock, D. E. 1987, *ApJS*, 63, 295
- Wright, E. L., et al. 2010, *AJ*, 140, 1868
- Wu, X.-B., Hao, G., Jia, Z., Zhang, Y., & Peng, N. 2012, *AJ*, 144, 49
- Yamauchi, C. 2011, *PASP*, 123, 1324

Table 11—Continued

log L	Sy2s		Sy2s + LINERs		Sy2s + Composites		Sy2s + LINERs + Composites	
	CF	σ_{CF}	CF	σ_{CF}	CF	σ_{CF}	CF	σ_{CF}
9.80	0.65	0.05	0.75	0.04	0.90	0.03	0.91	0.03
10.2	0.57	0.03	0.68	0.03	0.86	0.03	0.87	0.03
10.6	0.45	0.04	0.54	0.04	0.75	0.04	0.77	0.04
11.0	0.34	0.05	0.46	0.06	0.59	0.07	0.65	0.07
11.4	0.18	0.08	0.20	0.08	0.46	0.14	0.47	0.14
11.8	0.44	0.32	0.44	0.32
$0.006 \leq z \leq 0.2$								
8.20	0.89	0.44	0.95	0.31	0.96	0.26	0.97	0.22
8.60	0.95	0.28	0.99	0.14	0.99	0.11	1.00	0.09
9.00	0.82	0.12	0.94	0.07	0.97	0.05	0.98	0.05
9.40	0.74	0.07	0.86	0.06	0.95	0.06	0.96	0.05
9.80	0.65	0.05	0.75	0.04	0.90	0.03	0.91	0.03
10.2	0.58	0.03	0.68	0.03	0.86	0.03	0.87	0.03
10.6	0.48	0.04	0.57	0.04	0.77	0.04	0.79	0.04
11.0	0.33	0.04	0.44	0.05	0.57	0.05	0.62	0.05
11.4	0.14	0.04	0.22	0.05	0.44	0.11	0.48	0.11
11.8	0.05	0.05	0.18	0.11	0.13	0.08	0.21	0.12
12.2	—	—	—	—	0.56	0.69	0.56	0.69

Table 12. Number density ratios of each galaxy type in each redshift bin. The number density is estimated from the 22- μm LFs.

type	$0.006 \leq z \leq 0.05$	$0.05 \leq z \leq 0.1$	$0.1 \leq z \leq 0.15$	$0.15 \leq z \leq 0.2$	$0.2 \leq z \leq 0.25$	$0.25 \leq z \leq 0.3$	$0.006 \leq z \leq 0.3$
(integral range)	$(8.0 \leq \log \nu L_\nu \leq 10.8)$	$(9.2 \leq \log \nu L_\nu \leq 11.2)$	$(9.6 \leq \log \nu L_\nu \leq 11.6)$	$(10.0 \leq \log \nu L_\nu \leq 11.6)$	$(10.4 \leq \log \nu L_\nu \leq 11.6)$	$(10.8 \leq \log \nu L_\nu \leq 11.6)$	$(8.0 \leq \log \nu L_\nu \leq 12.0)$
type 1	1.00	1.00	1.00	1.00	1.00	1.00	1.00
type 2	4.80 ± 1.17	1.80 ± 0.14	0.96 ± 0.07	0.79 ± 0.13	0.09 ± 0.02	0.06 ± 0.04	4.08 ± 0.85
LINER	9.08 ± 2.00	1.37 ± 0.13	0.59 ± 0.10	0.27 ± 0.04	0.03 ± 0.01	0.43 ± 0.42	7.42 ± 1.37
Composte	20.76 ± 4.39	8.41 ± 0.61	3.15 ± 0.20	1.13 ± 0.11	0.35 ± 0.07	0.11 ± 0.05	17.38 ± 3.00
SF	93.87 ± 4.34	19.68 ± 0.53	4.99 ± 0.20	1.34 ± 0.13	0.16 ± 0.07	0.01 ± 0.08	79.19 ± 2.96